December 2017

Vortex detection and tracking in massively separated and turbulent flows

Yangzi Huang
Syracuse University

Abstract

The vortex produced at the leading edge of the wing, known as the leading edge vortex (LEV), plays an important role in enhancing or destroying aerodynamic force, especially lift, upon its formation or shedding during the flapping flight of birds and insects. In this thesis, we integrate multiple new and traditional vortex identification approaches to visualize and track the LEV dynamics during its shedding process. The study is carried out using a 2D simulation of a flat plate undergoing a 45^o pitch-up maneuver. The Eulerian Γ_1 function and Q criterion are used along with the Lagrangian coherent structures (LCS) analyses including the finite-time Lyapunov exponent (FTLE), the geodesic LCS, and the Lagrangian-Averaged Vorticity Deviation (LAVD). Each of these Lagrangian methods is applied at the centers and boundaries of the vortices to detect the vortex dynamics. The techniques enable the tracking of identifiable features in the flow organization using the FTLE-saddles and λ-saddles. The FTLE-saddle traces have shown potential to identify the timing and location of vortex shedding, more precisely than by only studying the vortex cores as identified by Eulerian techniques. The traces and the shedding times of the FTLE-saddles on the LEV boundary matches well with the plate lift fluctuation, and indicates a consistent timing of LEV formation, growth, shedding. The formation number and vortex shedding mechanisms are compared in the thesis with the shedding time and location by the FTLE-saddle, which validates the result of the FTLE-saddles and provide explanations of vortex shedding in different aspects (vortex strength and flow dynamics).

The techniques are applied to more cases involving vortex dominated flows to explore and expand their application in providing insight of flow physics. For a set of experimental two-component PIV data in the wake of a purely pitching trapezoidal panel, the Lagrangian analysis of FTLE-saddle tracking identifies and tracks the vortex breakdown location with relatively less user interaction and provide a more direct and consistent analysis. For a simulation of wall-bounded turbulence in a channel flow, tracking FTLE-saddles shows that the average structure convection speed exhibits a similar trend as a previously published result based on velocity and pressure correlations, giving validity to the method. When these Lagrangian techniques are applied in a study of the evolution of an isolated hairpin vortex, it shows the connection between primary and secondary hairpin heads of their circulation and position, and the contribution to the generation of the secondary hairpin by the flow characteristics at the channel wall. The current method of tracking vortices yields insight into the behavior of the vortices in all of the diverse flows presented, highlighting the breadth of its potential application.

Vortex detection and tracking in massively separated and turbulent flows

by

Yangzi Huang
B.S. Xi'an Jiaotong University, August 2008
M.S. Xi'an Jiaotong University, August 2011

Dissertation
Submitted in partial fulfillment of the
requirements for the degree of
Doctor of Philosophy
in
Mechanical and Aerospace Engineering
at
Syracuse University

December 2017

Acknowledgements

I kindly thank my advisor Professor Melissa A. Green, for her guidance, patience and support throughout my research at the Syracuse University. It is an honor to work with her, whose enthusiasm and optimism have greatly motivated me to stay focused on my research. I would like to thank all the past and present members of Green Fluid Dynamics Lab for their invaluable assistance. In particular, I would like to thank Dr. Matthew Rockwood for his specific advice and direction at various stages of my research. I am grateful also for the friendship and encouragement from Dr. Swathi Krishna, Eileen Haffner, Jenna Philipp, Justin King, and Dr. Richard Galvez.

I would like to express my deepest gratitude to my husband, Mattias and my parents, Yuming and Hongqi, for their unconditional love and support throughout my graduate studies. This endeavor would be impossible without them.

This work was supported by Air Force Office of Scientific Research, under grant number FA9550-14-1-0210. Their sponsorship is gratefully acknowledged.

Contents

List of Figures

List of Tables

Chapter 1

Introduction

1.1 Bio-inspired micro aerial vehicles design and leading edge vortex shedding

The need for micro aerial vehicles (MAVs, figure 1-1(a)), which are small, intelligent, and capable of dealing with challenging environments, has been increasing in military, commercial, scientific, recreational and other applications, such as aerial photography, delivery, surveillance, etc (Zbikowski, 2000; Żbikowski, 2002a; Pitt Ford and Babinsky, 2013). MAVs face unique challenges different from conventional aircraft, such as unsteady flow fields when encountering a gust, and transitions from steady to unsteady flow or from laminar to turbulent flow, due to their small size, low flight speed and working environment.

In MAV design, a new trend has arisen that takes inspiration from flying insects or birds (figure 1-1(b)), whose flapping flight produces much higher lift than the corresponding fixed wings at low Reynolds number, $Re = U_\infty c/\nu \leq 10^4$ (based on characteristic appendage length c and velocity U_∞), to achieve unprecedented flight capabilities (Dickinson and Gotz, 1993; Ellington et al., 1996; Wang, 2005; Eldredge et al., 2009; Mueller, 2001; Pines and Bohorquez, 2006; Shyy et al., 2010). The flapping wing mechanism at high-angles of attack, however, imposes challenges that are unseen in fixed wing vehicles, especially the formation of large scale vortical structures such as the leading edge vortex

(a) Bio-inspired MAV (image courtesy of Srigarom and Chan (2015))

(b) Animals with flapping flight (image courtesy of Institute of Physics)

Figure 1-1: MAV design mimicking natural flyer flapping-wings.

(LEV), significantly altering the behavior of the aerodynamic forces (Shyy et al., 2008). A better understanding of unsteady aerodynamics associated with massive separation at low *Re* can be utilized to improve maneuverability and performance of MAVs (Shyy et al., 2008; Pesavento and Wang, 2009).

1.1.1 Influence of leading edge vortex in massively separated flow

Unsteadiness in conventional air vehicles is considered a deficit since the unsteady motion can lead to flow separation, instabilities, and flow-structure interactions that are difficult to control. However, certain insects (Birch and Dickinson, 2001; Sane, 2003; Żbikowski, 2002b) and birds (Videler et al., 2004; Pesavento and Wang, 2009; Polet et al., 2015; Polet and Rival, 2015) take advantage of specific maneuvers and the extent of their flow control authority to manage the unsteady effects associated with flow separation in different applications.

Key to understanding the aerodynamics of natural flyers flight is the phenomenon of flow separation, in which the formation and shedding of coherent vortices can develop. The complex wing kinematics can provide efficient locomotion and control in complex flow environments or during precise maneuvers. Vorticity generation is also modified, which can change the nature and dynamics of shed vorticity. A dynamic stall (figure 1-2) occurs over aerodynamic surfaces when the effective angle of attack and the LEV formed by flow separation changes rapidly (McCroskey, 1982). The LEV interacts with the

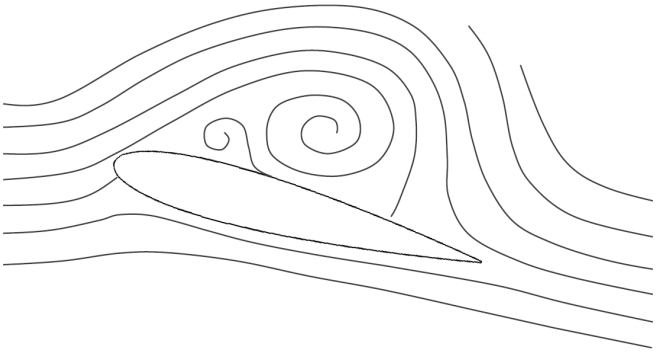

Figure 1-2: Streamlines representing typical stall behavior of an aerodynamic surfaces (image courtesy of Buchner (2016)).

wing surface and with vorticity shed from the trailing edge, which provides temporarily enhanced lift and decreased pitching moment, and then sheds downstream, resulting in lift loss and determining the ultimate form of the wake (Smith, 2005; Akkala et al., 2015; Buchner, 2016). The physical mechanisms driving the complex process of flow separation have remained in many ways unknown, requiring greater understanding of the production, evolution, and interaction of vortices and shear layers shed by the pitching airfoil (Żbikowski, 2002b; Eldredge et al., 2009; Ol et al., 2009; Buchner, 2016).

The attempt to model the flapping flight first emerged in the early work by Theodorsen and Mutchler (1935), which approached the problem of unsteady airfoil aerodynamics (the modeling of flutter in aircraft wings) from a quasi-steady perspective and led to practical modeling tools. Early work on the aerodynamic effects of more complex motions also include the assessment of an airfoil starting from rest by Wagner (1925), the response of an airfoil to a gust by Küssner (1936), and a theory related to generalized airfoil motions by Kármán (1938). Following on from these studies, it has become almost standard to model flapping flight as a simple combination of pitching, heaving, and surging motions, as well as some more complex three-dimensional (3D) motions such as wing-root rotation. Later on, Osborne (1951) and Pringle (1965) proposed the basic quasi-steady models, in which the instantaneous forces on the flapping wing were assumed to be equivalent to those for steady flight at the same instantaneous velocity and angle of attack.

The pioneering work on insect-wing flight mechanisms was started with the basic

quasi-steady models (Weis-Fogh, 1972, 1973; Lighthill, 1973; Maxworthy, 1979), then was rejuvenated by a series of seminal work by Ellington (1984a,b,c,d) in the 1980*s*. The latter strongly speculated the presence of unsteady flow mechanisms that led to further study in the area, i.e., the most complete description of insect-wing flapping motion at the time. Although it had been observed in earlier experiments (Martin and Carpenter, 1977; Maxworthy, 1979), it was not until then that the key role of the LEV received proper recognition in natural flight. The unsteady flow around flapping wings comprises two components, the attached flow due to freestream flow over the wing and that due to the unsteady motion, and separated flow in the form of wakes shed from both leading and trailing edges (Ellington, 1984c). Ellington (1984c) also described the dynamic stall of hovering insects, and believed it to be critical in force generation at low *Re*. High values of lift coefficient were associated with the formation of an LEV, which for specific parametric combinations was subsequently mixed with trailing-edge vortices (TEV) (McCroskey, 1981; Freymuth, 1990). Reynolds and Carr (1985) later provided insight on the basic mechanism governing LEV generation and stabilization, establishing the influence on lift enhancement by spanwise flow through the core of the LEV.

In the past two decades, a large number of experimental studies based on observations and measurements have been carried out to better understand the vortex dynamics in the near wake and the associated aerodynamic implications in flapping flight. For example, Ohmi et al. (1990, 1991) studied the vortex formation in the flow around a translating and harmonically pitching airfoil at *Re* between 1500 and 10000, with mean angle of attack of 15° or 30°, by a pathline method. At large angle of attack they found that the patterns in the vortex wake depend on whether the translational or rotational motion dominates the flow, and how the LEV interacts with TEV, while the *Re* effect was of secondary importance. In the case of the flow dominated by the rotational motion, the governing parameter is the product of the reduced frequency and the pitch amplitude, which is closely related to the Strouhal number (*St*) (Triantafyllou et al., 1991, 1993). Brodsky (1991) first measured the structure of the vortex wake for a peacock butterfly flying in a wind tunnel using high-speed filming, which showed that the near wake of the butterfly in 'feeding' flight was a system of discrete pairs of coupled vortex rings,

and the propulsive force is produced continuously through the evolutionary changes in the interaction between wings and the ambient environment. Grodnitsky and Morozov (1992, 1993) studied the near wake structures of several insects in tethered flight with a dust flow visualization technique. Their results indicated that flapping insects created a single vortex ring during each stroke, that an insect interacts with its own wake during the whole stroke cycle to gain additional energy, and that insects have adopted kinematic and morphological adaptations to increase the total efficiency of their flight apparatus.

Dickinson and Gotz (1993) carried out two-dimensional (2D) experiments on insect-like flapping-wing motion and investigated the effects on the lift of several kinematics parameters with the force measurement and flow visualization techniques. Jones conducted a series investigations of the propulsive properties of a heaving airfoil both theoretically and experimentally (Jones et al., 1996, 1997; Jones and Platzer, 1999; Jones et al., 2000; Jones and Babinsky, 2011). Ellington and his co-workers made the remarkable discovery of the LEV on a scaled-up model of the hawk-moth wings ($Re \simeq 100$) (Ellington et al., 1996; Willmott et al., 1997; Van Den Berg and Ellington, 1997a,b). They reported that insects utilize unsteady aerodynamic mechanisms to produce enough lift force to stay aloft, and in particular, prolonged attachment of an LEV due to the spanwise vortex stabilization was shown to be a key element in enhancing the lift force production. They postulated that spanwise flow through the vortex core, causing a conical spiral vortex coalescing with the tip vortex and convecting into the trailing wake, was responsible for the redirection of momentum toward the wing tip. This would then allow for the LEV circulation to remain sufficiently small to delay vortex shedding, similar to the quasi-steady stabilization experienced in the low AR delta-wing LEV arrangement (Martin and Carpenter, 1977; Van Den Berg and Ellington, 1997a,b). Not long after these studies, Liu et al. (1998) found that due to the presence of the LEV, the wings of a hovering hawk-moth were able to generate lift force up to 40% greater than that required to support its weight.

Anderson et al. (1998) studied the thrust-producing harmonically oscillating foils through force and power measurements, as well as visualization data, to classify the principal characteristics of the flow around and in the wake of the foil. Dickinson et al.

(1999) measured the near field flows around and aerodynamic forces acting on a robotic fly model wing in an idealized hovering motion by means of the particle imaging velocimetry (PIV) techniques. Thomas et al. (2004) and Bomphrey et al. (2005, 2006) investigated the LEV structure of several real insects in forward flight with high resolution using smoke-wire visualization and PIV techniques, which indicated that the LEV could be continuous across the thorax and contribute to the aerodynamic force generation in a form of vortex-body interactions. Poelma et al. (2006) carried out quantitative measurements of time-dependent 3D velocity fields around a flapping wing. Recently, Baik et al. (2011) investigated an experiment of a pitching and plunging flat plate at a prescribed effective angle of attack in the range of $0.16 \leq St \leq 0.35$. Using PIV, Akkala et al. (2015) investigated the kinematic and aerodynamic behaviors of sinusoidally plunging, flexible airfoils over a parameter space broadly representative of flapping flight, and described the evolution of flow structures with the effects of airfoil deformation, and developed a scaling parameter.

There have also been many numerical approaches that have been carried out for aerodynamic analysis of wings in severe unsteady maneuvers. Wang (2000a, 2003, 2005) have been tackling the problem of insect-flight aerodynamics from a computational fluid dynamics (CFD) point of view, which showed the association between the unsteady flow and accelerating flat plates using Navier-Stokes (NS) calculations. Similarly, using both inviscid models and CFD methods, Pullin and Wang (2004) analyzed the flow past an accelerating flat plate at fixed angles of attack. Jones (2003) considered the unsteady separated flow of an inviscid fluid around a moving flat plate by a boundary-integral method to represent and solve for the velocity field. Zdunich (2003) arrived at similar results for the unsteady separated flow around a thin airfoil, but without recourse to complex algebra. Ansari et al. (2006) developed a circulation-based, quasi-three-dimensional unsteady aerodynamic model of insect-like flapping wings in hover, and showed a good agreement with existing experimental data in terms of both flow field representation and force prediction. Aono et al. (2009) investigated and addressed the vortex dynamics of the unsteady 3D near wake of a hovering hawk-moth and its correlation with the aerodynamic force production by means of a biology-inspired dynamic flight simulator.

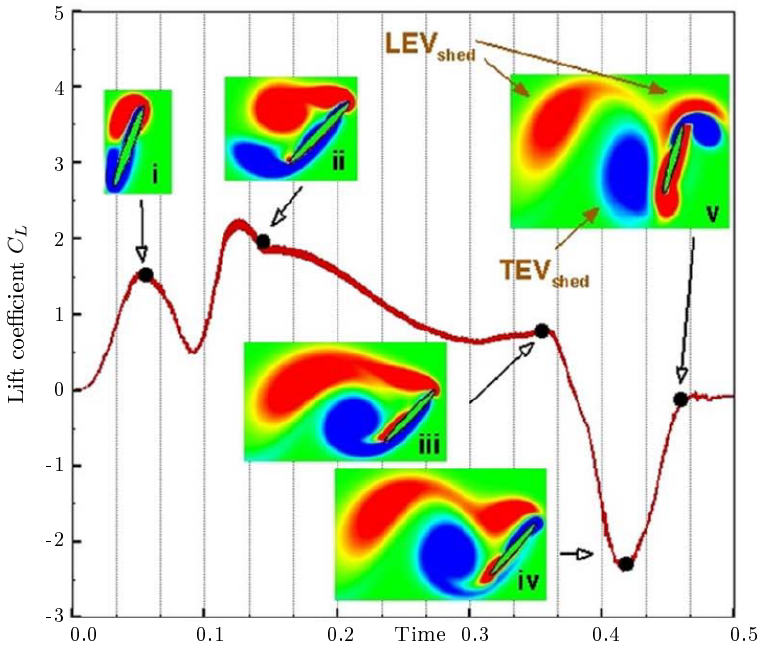

Figure 1-3: Lift coefficient per wing as a function of dimensionless time for a fling at $Re = 128$ (image courtesy of Arora et al. (2014)). The insets show the vorticity contours around the wing at the instants corresponding to the wing positions. At the beginning of fling $(i) - (ii)$, a strong LEV is formed, resulting in lift increase. Later, the LEV is about to shed in $(ii) - (iii)$, thus a gradual drop in lift is registered.

Using the lattice Boltzmann method (LBM) simulations for the 'clap and fling' motion, Arora et al. (2014) indicated the evolving LEV and its circulation that enhanced instantaneous lift on the wing, and the LEV shedding that corresponds with gradual lift drop, as shown in figure 1-3, especially at low Re. Jardin and David (2015) reviewed some main hypotheses of both LEV attachment and high lift generation on revolving wings by direct numerical simulation (DNS) of the NS equations, and evaluated the influence of the Coriolis effects on the lift generation.

The described studies have investigated numerous aspects of the vortex dynamics in near wake and have deepened the understanding of the aerodynamics of natural flapping flight. Missing from the literature are investigations of some of the finer points of the LEV shedding behavior and its influence on the aerodynamic forces over the wings. The complementary insight into the detailed fluid physics associated with the LEV will inform wing-design guidelines for MAVs.

1.1.2 Origins of leading edge vortex shedding

As postulated in section 1.1.1, the lift development of unsteady aerodynamic motion shows a close association with the LEV evolution and the corresponding near wake flow at low Re (McCroskey, 1982; Jones and Babinsky, 2010). The evolution of an LEV can be categorized into two main stages: formation and shedding. The former stage is initiated by shear-layer roll-up at the leading edge, and is characterized by the LEV attachment to the aerodynamic surface. During the formation, the LEV continuously increases in size and circulation, correlating to lift enhancement. This is followed by the LEV shedding and convecting downstream, and the lift then drops correspondingly (Dickinson et al., 1999; Wang, 2000b; Carr et al., 2013; Widmann and Tropea, 2017). In particular, the importance of the LEV shedding mechanisms to unsteady lift, deciding both the maximum lift that can be achieved and lift peak generation timing, is due largely to its maximum achievable circulation and shedding timing. It has also motivated the investigation of the parametric dependence of vortex strength on vortex evolution, and scaling laws to predict vortex strength (Buchholz et al., 2011; Wang and Eldredge, 2013; Wojcik and Buchholz, 2014).

A number of hypotheses regarding the origins of vortex shedding for inviscid/viscous and internal/external flows have been put forth, such as 'formation number' N (Gharib et al., 1998; Rosenfeld et al., 1998); flow instability (Boghosian and Cassel, 2016); topological flow changes inside a vortex (Dallmann et al., 1995; Theofilis et al., 2000; Marquillie and Ehrenstein, 2003); an eruption of secondary near-wall vorticity bisecting the main vortex (Obabko and Cassel, 2002); local temporal instability near the center of the vortex with upstream and downstream traveling disturbances (Marquillie and Ehrenstein, 2003; Wee et al., 2004). Among them, the most commonly used concept to explain vortex shedding in biological flight is the optimal vortex formation, which is associated with the formation number introduced originally by Gharib et al. (1998).

Gharib et al. (1998) used a piston-cylinder apparatus with flow visualization and PIV to demonstrate that there is a limit to the size and strength (circulation) that a vortex ring can attain, which is referred to as saturation. Upon saturation, the vortex

rings are shed via a process termed 'pinch-off' based on the Kelvin-Benjamin variational principle (Kelvin, 1880; Benjamin, 1976). Vortex ring pinch-off is characterized by the non-dimensional 'formation time', $\hat{T} = L/D$ (in their case, equivalent to the piston stroke-length-to-diameter ratio). Gharib et al. (1998) reported that for a variety of piston kinematics and geometry, a leading vortex ring saturates at $\hat{T} \approx 4$, while the vortex ring increases in size and circulation but remains unsaturated for $\hat{T} < 4$, and for $\hat{T} > 4$, additional entrainment of vorticity from the shear layer is rejected by the vortex ring and remains spatially in the adjacent trailing jet (shown in figure 1-4) (Pottebaum and Gharib, 2004). The formation number is defined as the formation time at which pinch-off happens, and exhibits as a universal time scale.

Gharib et al. (1998) observed $N = 4$ for vortex ring generated by an impulsively started jet from the piston-cylinder, while N falls in a range of $3.6 - 4.5$ for a broad range of generating flow conditions. Krueger and Gharib (2003) demonstrated that the time-averaged thrust for starting jets generated using a piston-cylinder mechanisms maximizes at instants $\hat{T} \approx N$, and the thrust reduces for time $\hat{T} > N$. The formation number concept then was extended to flow past oscillating cylinders by Jeon and Gharib (2004) and to temporarily varying orifices by Dabiri and Gharib (2005).

Milano and Gharib (2005) attempted to bridge the gap between piston-cylinder and impulsively-started, flat-plate work, using a genetic algorithm validated by Milano and Koumoutsakos (2002). They reported the optimized solutions of a flapping rectangular plate with aspect ratio $AR = 6$ produced an LEV of maximum circulation with associated formation numbers in the range of $3.6 - 4.6$, in agreement with previous studies. Similarly, Ringuette et al. (2007) studied vortex development in the wake of a rectangular flat plate $AR = 2$ and 6 undergoing a purely translating motion, to investigate the influence of the tips on vortex growth along the edges. His study showed the LEV saturated at each of the chord-wise planes investigated, indicating that the optimal vortex formation methodology is applicable to vortices in the wake of accelerating plates.

Dabiri (2009) extended the optimal vortex formation concept by defining the formation number based on the feeding shear-layer velocity and the characteristic length of the vortex generator, which provides a good scaling for the maximum LEV circulation gener-

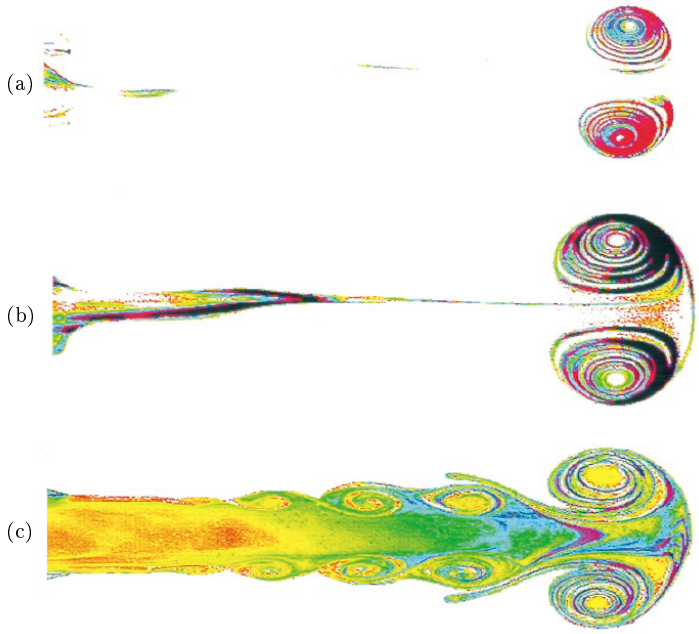

Figure 1-4: Visualization of vortex rings for (a) $\hat{T} = 2$; (b) $\hat{T} = 3.8$; (c) $\hat{T} = 14.5$ generated through impulsively started jet by the piston-cylinder (image courtesy of Gharib et al. (1998)).

ated by an airfoil executing unsteady motions. Since then, a formation number is found for a wide range of natural flyer flight. Rival et al. (2009) studied various bio-inspired airfoil kinematics, and demonstrated the relevance of vortex shedding to all maneuvers investigated with formation numbers between a range of 4.4 and 5. Jones and Babinsky (2011) showed that for $AR = 4$ rotating flat plates at 25° angle of attack and Re ranging from 1×10^4 to 6×10^4, formation number does capture the trends in LEV saturation and lift accounting for the Re variation. Onoue and Breuer (2016) demonstrated that the LEV formation time and circulation scale with the characteristic velocity of the feeding shear layer over a range of reduced frequencies $(0.038 - 0.11)$ and pitching amplitudes $(42° - 100°)$ at distinct Re on a rapidly pitching flat plate, and had a scaled LEV circulation and vortex formation time peak within a range of $N = 3.5 - 4$.

It is also quite common to see vortex shedding interpreted as a result of a 'Kelvin-Helmholtz-like' instability of the shear layer (Cherdron et al., 1978; Pauley et al., 1990; Tsui et al., 1995; Kaiktsis et al., 1996; Mittal et al., 2003; Boghosian, 2011). Previous research by Boghosian and Cassel (2013) has indicated that pressure gradient forces

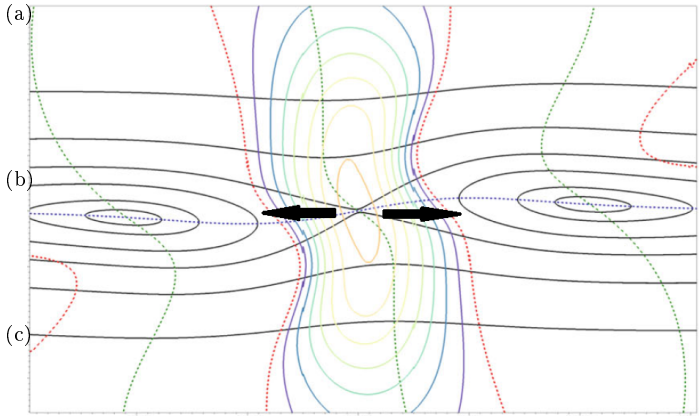

Figure 1-5: Demonstration of VSM in the flow field of an elliptically shaped vortex. Contour of net force divergence and streamlines (black lines) are plotted. Zero momentum location is shown by intersection of $u = 0$ and $v = 0$. which becomes the vortex shedding location due to the local maxim of net force divergence (image courtesy of Boghosian and Cassel (2016)).

having a specific magnitude signature (adverse, zero, and favorable in the streamwise direction) acting on regions in the flow having zero momentum, plays a critical role in making the physical link between the presence of an instability, and the subsequent vortex shedding. This explanation is called the pressure gradient mechanism (PGM) (Boghosian and Cassel, 2013). Essentially, the vortex is pulled apart by the adverse and favorable pressure gradients on the upstream and downstream sides of the shear layer at the shedding location. Boghosian and Cassel (2016) expanded PGM in vortex shedding by including viscous and body forces and eliminating directional dependence, which is termed the vortex shedding mechanism (VSM) and proved that it is mathematically valid for any 2D, incompressible flow, as demonstrated in figure 1-5. Similarly, Lawson and Dawson (2013) proposed a theory attributing the initiation of vortex ring pinch-off from a synthetic jet with a trailing pressure maximum (TPM) that forms at upstream of the vortex ring.

By examples from the existing literature, it has been shown that vortex shedding mechanisms can potentially serve as models for aerodynamic force prediction. Additionally, optimal vortex formation can provide a unifying principle to understand the diversity of solutions used to achieve propulsion in natural fliers. To obtain detailed knowledge of the vortex shedding mechanisms of LEV, it is necessary to investigate the shedding

timing and saturation strength of an LEV to understand the relationship between the wake structures and the aerodynamics (DeVoria and Ringuette, 2012).

1.2 The state of the art in vortex identification methods

Vortices, especially LEVs, and their interaction with aerodynamic bodies in separated flow are ubiquitous features in wakes of aerodynamic surfaces at high angles of attack associated with flapping wings. Previous indicators of LEV shedding are mainly based on the examination of airloads, which include the instants at which the pitching moment coefficient changes significantly, or the achievement of maximum or critical leading edge suction (Leishman and Beddoes, 1989; Wilby, 2001; Sheng et al., 2006). Qualitative and quantitative descriptions of the vortex dynamics based directly on the flow field by vortex identification methods are required, which can provide insight into the physical mechanisms of lift generation/loss and moment balance over the flapping-wings (Brunton and Rowley, 2009a; Mulleners and Raffel, 2012; Huang and Green, 2016).

Although the identification and tracking of vortices is not a new problem, a widely-accepted, objective definition of a vortex and its boundaries remains elusive (Jeong and Hussain, 1995; Chakraborty et al., 2005). The common goal of vortex identification methods is to locate, extract, and visualize vortical structures. The diffusion of vorticity by viscosity, coupled with the interaction of vorticity distribution with background strain fields, makes the vortex identification problem in real (complex, unsteady, 3D) fluids quite complicated. A series of reviews have been provided by Post et al. (2003); Salzbrunn et al. (2008); Pobitzer et al. (2010, 2011).

1.2.1 Eulerian approaches

Many commonly-used vortex criteria are Eulerian, which are calculated using spatial derivatives of the velocity field, such as closed or spiraling streamlines, iso-vorticity surfaces, pressure minima etc. The Eulerian criteria generally identify coherent structures

as concentrated regions of high vorticity, and usually contain the essential characteristics of the flow induced by a vortex filament (McWilliams, 1984; Hussain, 1986; Chakraborty et al., 2005). These Eulerian approaches define a function that can be evaluated point-by-point and then classify each point as being inside or outside a vortex according to a criterion based on the point values.

Most local vortex identification criteria are derived from the velocity gradient tensor (or *Jacobian*), $\bigtriangledown \boldsymbol{u}$, thereby making them Galilean invariant, i.e., invariant under any constant speed translation of the underlying coordinate system (Post et al., 2003; Günther et al., 2016). The most popularly used local criteria are: the Q-criterion (Hunt et al., 1988), λ_2-criterion (Jeong and Hussain, 1995), the Δ-criterion (Chong et al., 1990), and the swirling strength, λ_{ci}^2-criterion (Zhou et al., 1999).

The Q-criterion identifies vortices as flow regions with positive second invariant of $\bigtriangledown \boldsymbol{u}$, i.e. $Q > 0$ (Jeong and Hussain, 1995; Dubief and Delcayre, 2000). The λ_2-criterion is formulated based on the observation that a local pressure minimum in a plane alone fails to identify vortices under strong unsteady and viscous effects. Jeong and Hussain (1995) defined the vortex as a connected region with two positive eigenvalues of the pressure Hessian matrix. If the eigenvalues of the symmetric tensor are ordered as $\lambda_1 \geq \lambda_2 \geq \lambda_3$, this definition is equivalent to the requirement that $\lambda_2 < 0$ at every point inside the vortex core. Using critical point theory, Chong et al. (1990) define a vortex to be the region where $\bigtriangledown \boldsymbol{u}$ has complex eigenvalues with the Δ-criterion. The swirling strength λ_{ci}^2-criterion (Zhou et al., 1999) is based on the Δ-criterion and uses the imaginary part of the complex conjugate eigenvalue of $\bigtriangledown \boldsymbol{u}$ to identify vortices. Cucitore et al. (1999) uses the change in the relative distance between particles inside a vortex structure, D-criterion, in conjunction with the $\Delta > 0$ to identify a vortex. Graftieaux et al. (2001) introduced the Γ_2 function, calculating an averaged rotation intensity to locate the vortex center in 2D flow fields, which has gained popularity due to its simplicity. Chakraborty et al. (2005) proposed using the ratio of real and imaginary parts of the complex eigenvalues of $\bigtriangledown \boldsymbol{u}$ to refine the definition of a vortex core. Okubo (1970) and Weiss (1991) independently developed a criterion related to the Q-criterion. As Jeong and Hussain (1995); Dubief and Delcayre (2000) and Haller (2005) have pointed out,

these Eulerian criteria identify similar structures in most flows except in some special cases, i.e. time-dependent rotations.

In the past, the above Eulerian approaches have been widely used in unsteady aerodynamic problems. Zhou et al. (1999) used λ_{ci}^2-criterion to study the evolution of a single hairpin vortex structure in the mean turbulent field of low Re. Berson et al. (2009) combined Γ_2 and streamlines to identify and track the location of vortex center with a non-zero convection velocity, which is validated using PIV performed in an oscillating flow as a model of a thermo-acoustic refrigerator. Yilmaz and Rockwell (2012) applied PIV, phase-referenced 3D streamline patterns, volume images of iso-Q-criterion and vorticity projections in orthogonal directions, to study the onset and development of the 3D flow structure around a wing undergoing a pitch-up maneuver and the relation between the flow features and the unsteady aerodynamic forces on the wing. Instantaneous flow features extraction can be combined with tracking of the singularities over time.

Because Eulerian scalar quantities depend only on the instantaneous velocity field and its gradient, they are relatively quick to compute. However, they share some disadvantages (as reviewed by Jeong and Hussain (1995); Cucitore et al. (1999); Kolář (2007)). When visualizing the data, especially in 3D, an important disadvantage is that the structure size and boundary shape can vary with the user's selection of threshold or iso-surface level.

1.2.2 Lagrangian approaches

In Lagrangian approaches, a vortex is generally viewed as an evolving domain with a high degree of material invariance (Chakraborty et al., 2005; Haller, 2005). Virtually, all Lagrangian approaches are based on the flow map, a vector quantity that maps fluid trajectories from their initial locations to their final locations in space after an integration time. They include information on the history/future of the flow, and have a clear physical interpretation (Gurtin, 1982). The Lagrangian approaches uncover repelling, attracting, and shearing material surfaces from experimental and numerical flow data, which promise a simplified understanding of the overall flow geometry, and exact quantification of material transport, thus providing a powerful prediction of vortical features

of the flow (Haller, 2015). A number of Lagrangian approaches have been proposed over the past two decades (Peacock and Dabiri, 2010; Peacock et al., 2015; Shadden, 2011; Haller, 2015; Allshouse and Peacock, 2015).

The Lagrangian coherent structures (LCS) analysis was initiated by Haller (2001), and includes a series of Lagrangian methods that calculate quantities based on the relative behavior of fluid particle trajectories. The most popular LCS analysis is based on finite-time Lyapunov exponents (FTLE) and related techniques (Haller and Yuan, 2000; Haller, 2002; Shadden et al., 2005; Lipinski and Mohseni, 2010; Allshouse and Peacock, 2015; Huntley et al., 2015; Balasuriya, 2015; He et al., 2016), the maximizing ridges of which have been defined geometrically as hyperbolic LCSs in some cases and represent partial vortex boundaries (Shadden et al., 2005; Lipinski and Mohseni, 2010; Haller, 2011; Mulleners and Raffel, 2012).

Unsteady aerodynamic problems have been widely explored with FTLE in the past two decades. FTLE was applied to vortex extraction from time-periodic laboratory experiments by Voth et al. (2002) and then from turbulent flow experiments by Mathur et al. (2007). Shadden et al. (2005) applied FTLE to the 'double gyre' example and various other example 2D flow fields. Shadden et al. (2006) studied the entrainment and detrainment of an empirical vortex ring as well as in the vicinity of a live jellyfish. Green et al. (2007) extended the application of FTLE combined with λ_{ci}^2-criterion and Q-criterion to a 3D turbulent channel flow. The entrainment regions of a sheet swimming in an inviscid fluid have been examined by the FTLE (Peng and Dabiri, 2008). Separation from an airfoil at a low angle of attack and $Re = 10^4$ has been studied by Lipinski et al. (2008) and Cardwell and Mohseni (2008), who used the FTLE and associated particle tracking to explore the vortex formation and reattachment topology. The FTLE obtained from a computational model of jellyfish swimming has been studied by Lipinski and Mohseni (2009) and in 2D flow with a low Re by Wilson et al. (2009). Later, Brunton and Rowley (2009b) used FTLE to visualize the wake of a flat-plate cross section of a wing either fixed or undergoing oscillatory pitching and plunging kinematics in a free stream with $Re = 10^2$. Green et al. (2010) used FTLE to investigate the evolution of vortical structures in the wakes of rigid pitching panels with a trapezoidal platform geometry

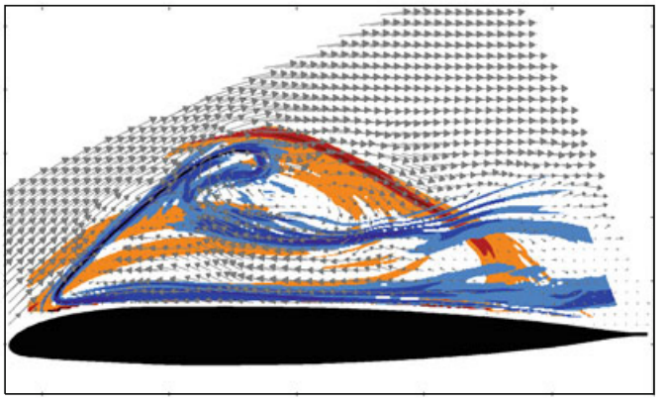

Figure 1-6: Presence of LEV at an instant during a dynamical stall cycle indicated by FTLE ridges (red-pFTLE, blue-nFTLE) (image courtesy of Mulleners and Raffel (2012)).

chosen to model idealized fish caudal fins. Mulleners and Raffel (2012) described the influence of the unsteadiness of a pitching wing with respect to the dynamic stall process utilizing a combination of FTLE (shown in figure 1-6) and Γ_2. O'Farrell and Dabiri (2014) used FTLE on both numerical and experimental data to study the vortex formation and shedding in starting jets.

As research in LCS analysis advances, there is inevitably evolution in the scope of the field. Recently, Haller (2011, 2015) initiated a stretching-based mathematical approach to identify Lagrangian vortical structures from the complex geophysical flow data by the geodesic theory. The geodesic theory of LCSs is a collection of global variational principles for material lines/surfaces, including hyperbolic, parabolic, and elliptic LCSs that form the time-evolving dynamical structures (Farazmand and Haller, 2012a; Haller and Beron-Vera, 2013, 2014; Haller, 2015).

The skeleton of the most influential hyperbolic LCSs act as the generalized stable and unstable manifolds over a finite-time interval (Farazmand and Haller, 2012b, 2013). Parabolic LCSs detect the shearless transport barriers that are minimally hyperbolic, hence serve as generalized jet cores (Farazmand et al., 2014). Elliptic LCSs extend the notion of Kolmogorov-Arnold-Moser (KAM) tori (a doughnut-shaped surface) and serve as generalized coherent vortex boundaries in unsteady flows (Haller and Beron-Vera, 2012; Beron-Vera et al., 2013). Most recently, Farazmand and Haller (2016) introduce the notion of rotationally coherent vortices as impermeable tubular material regions with

a high concentration of vorticity over a finite time interval. In this fashion, Haller et al. (2016) use the Lagrangian Averaged Vorticity Deviation (LAVD), to identify rotationally coherent vortices, whose elements exhibit identical mean material rotation.

These recent LCS analysis approaches were established to provide objective (material invariant) vortex extraction methods. Objectivity requires that the vortex identification methods provide invariant results under Euclidean coordinate changes of the form (Truesdell and Noll, 2004),

$$y = Q(t)x + p(t), \tag{1.1}$$

with $Q(t)$ denoting a time-dependent proper orthogonal tensor and $p(t)$ denoting a time-dependent translation (Haller, 2015). Therefore, the Lagrangian vortex is defined objectively in this way, representing the material evolution independent of the observer (Gurtin, 1982).

Other than the contribution of Haller and his group, there are several other heuristic and mathematical Lagrangian approaches that have been developed over the years, including Finite-Size Lyapunov exponent (FSLE) (Joseph and Legras, 2002; d'Ovidio et al., 2004; Bettencourt et al., 2013), Perron-Frobenius transfer operator methods that help determine regions that 'hold together' (Froyland and Padberg, 2009; Dellnitz and Junge, 2002; Froyland et al., 2010), topological analyses based on braids (Allshouse and Thiffeault, 2012; Budišić and Thiffeault, 2015), ergodic partitions and entropy Budišić and Mezić (2012); Froyland and Padberg-Gehle (2012), the Koopman operator (Mezić, 2013), sets whose boundaries retain their curvature (Ma and Bollt, 2014), clustering (Huntley et al., 2015; Froyland and Padberg-Gehle, 2015), and a Lagrangian generalization of the Okubo-Weiss criterion via mesochronic analysis (Mezić et al., 2010).

Cucitore et al. (1999) extracted LCS by observing the neighboring particles around a particle, i.e., they let the reference frame move with the tested particle. Salzbrunn et al. (2008) introduced the notion of 'pathline predicates (Boolean function)', which proposed a pathline placement allowing a user to track individual particles showing a specified behavior, yielding a proper illustration of the flow. Lagrangian smoothing as proposed

by Fuchs et al. (2008) and Shi et al. (2009) can be applied to any local vortex detector that was originally designed for steady flow by smoothing the extraction results along pathlines over time. Weinkauf and Theisel (2010) developed the description of streaklines as tangent curves of a derived vector field, and show how it can be computed from the spatial and temporal gradients of the flow map. A particle density estimation is proposed by Wiebel et al. (2011), which injects a number of particles and observes their attraction behavior over time. Specifically, their mesochronic classification considers regions where the deformation gradient has real eigenvalues as mesohyperbolic, and regions where the deformation gradient has complex eigenvalues as mesoelliptic. Mancho et al. (2013) proposed that abrupt variations in the arc-length function of a trajectory indicate the positions of boundaries of qualitatively different dynamics, which is quick to compute but not objective. Some comprehensive reviews of the diversity of Lagrangian approaches and recommendations for applying their requirements are provided by Jiang et al. (2005); Peacock et al. (2015) and Hadjighasem et al. (2017).

As a new vortex identification scheme, Lagrangian approaches have gained more popularity due to their objective nature, i.e., frame invariant under any smooth translation and rotation of the coordinate system (Günther et al., 2016). LCS analyses provide the insight into the structure and dynamics of the shear layer that analysis of the Eulerian approaches overlook (Shadden et al., 2005; Garth et al., 2007).

1.3 Objectives

There is a wealth of previous work addressing the problem of vortex dynamics in massively-separated flow of flapping-flight with a variety of approaches. However, there is a corresponding lack of fundamental research based on the direct vortex detection and tracking with current vortex identification methods, and a lack of convergence of the various vortex shedding mechanisms that explain the occurrence of physically-significant phenomena.

In the work of this thesis, Eulerian vortex identification approaches, along with Lagrangian coherent structure analysis, such as hyperbolic LCS, Lagrangian saddle, and LAVD, are used to study the LEV separation in a plate simulation. The optimal vortex

formation concept and VSM are examined in the research to reveal more mechanisms of vortex shedding.

While current computational systems can efficiently process the velocity information needed to track trajectories for these Lagrangian calculations, improvements in experimental techniques have led to increasingly large amounts of data, requiring development of automated procedures for vortex tracking (Chong et al., 1990). All the computations are implemented automatically by the code developed as a part of this work. An additional objective of this thesis work is to minimize user interaction for successful identification and tracking of physically significant vortex structures.

This thesis seeks to contribute to the following ongoing discussion in the field of unsteady aerodynamics by doing the following:

- Initiate a discussion of the definition of vortex shedding and influences on vortex shedding, including perspectives of vortex dynamics and flow dynamics for research on the physical mechanisms of vortex shedding, and connections between vortex dynamics and aerodynamic forces on the immersed body.

- Implement several new Lagrangian vortex identification methods for study of vortex visualization and tracking in massively separated and turbulent flow and establish their efficacy and appropriateness for different data sets.

- Provide suggestions on proper usage of multiple vortex criteria and combine applications of multiple vortex criteria for complete descriptions of vortex dynamics in unsteady 2D and 3D flow fields.

Chapter 2

Analysis Techniques

The main focus of vortex dynamics analysis in the current study is to determine the evolution of the LEV and study the origin of its shedding since it is believed to have a critical influence on lift in unsteady aerodynamics (Chakraborty et al., 2005). It involves two steps: the detection of the vortex and the analysis of its location and strength. In this chapter, the numerical analysis scheme used to detect the LEV during its formation and shedding process are presented, as well as some vortex shedding mechanism diagnostics.

2.1 Visualization Techniques

In the study, a combination of multiple vortex detection schemes are applied to visualize the vortex by its area, center and boundary, which are used for tracking as well.

2.1.1 Γ_1, Γ_2 functions

Many Eulerian criteria are not capable of pinpointing the individual vortex axes or determining the geometry of the various vortex cores (Mulleners and Raffel, 2012). The Γ_1, Γ_2 functions provide a simple and quick way to indicate the vortex center. Graftieaux et al. (2001) initially defined the scalar function Γ_1 by using the topology of streamlines to find the center of the vortex core in 2D flows. The velocity field is sampled at discrete spatial locations, and the Γ_1 quantity is defined as,

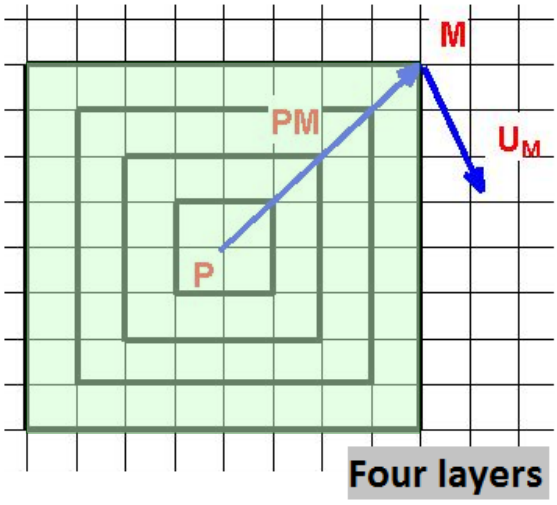

Figure 2-1: Demonstration of Γ_1 function calculation.

$$\Gamma_1(P) = \frac{1}{N}\sum_{i=1}^{N}\frac{(\boldsymbol{PM}\times\boldsymbol{U}_M)\cdot\boldsymbol{z}}{||\boldsymbol{PM}||\cdot||\boldsymbol{U}_M||}dA = \frac{1}{N}\sum_{i=1}^{N}\sin(\theta_M)dA, \tag{2.1}$$

where A is a 2D rectangular domain of fixed size and geometry, centered on P (shown as light green block in figure 2-1) and M lies in A. Here, N is the number of points M inside A, and z is the unit vector normal to the measurement plane. θ_M is the angle between the velocity vector at M (U_M) and the radius vector at M (PM). $||\cdot||$ represents the Euclidean norm of the vector (sometimes known as the Frobenius norm). The parameter N plays the role of a spatial filter, but only weakly affects the location of the maximum Γ_1 function (Graftieaux et al., 2001), which is chosen as 4×4 in this thesis.

The vortex center location is determined by the local maxima of Γ_1, typically ranging from 0.9 to 1 near the vortex center. The sense of vortex rotation is given by the sign of the Γ_1 function. An example of vortex detection by the Γ_1 function is given in figure 2-2, where a simple 2D periodic Bickley jet model involving several rotating vortices (Onu et al., 2015) is visualized by streamlines and Γ_1 function contours. The vortex centers are captured by local maxima of Γ_1 function, coinciding with the rotating center of the closed streamlines.

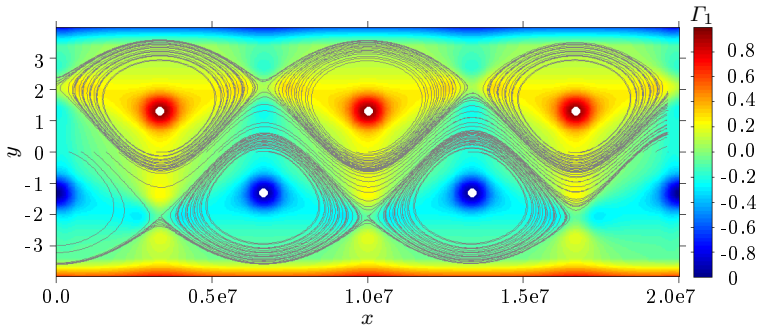

Figure 2-2: Visualization of Bickley jet flow field by Γ_1 contour and streamline (gray lines). The vortex centers are shown by white spots.

The Γ_1 quantity itself is not Galilean invariant, meaning that it is affected by reference frame translation. The local function Γ_2 was derived from the previous Γ_1 algorithm to account for this (Graftieaux et al., 2001). It takes into account a local convection velocity $\tilde{U}_P$ around P and thus is Galilean invariant. Γ_2 function is defined as,

$$\Gamma_2(P) = \frac{1}{N} \sum_{i=1}^{N} \frac{(\boldsymbol{PM} \times (\boldsymbol{U}_M - \tilde{\boldsymbol{U}}_P)) \cdot \boldsymbol{z}}{||\boldsymbol{PM}|| \cdot ||\boldsymbol{U}_M - \tilde{\boldsymbol{U}}_P||} dA, \tag{2.2}$$

where $\tilde{\boldsymbol{U}}_P = \frac{1}{N} \sum_{i=1}^{N} \boldsymbol{U}_M \; dA$.

Graftieaux et al. (2001) defined a vortex core in 2D flow as area with $\Gamma_2 > 0.6$, and showed that the locus of the vortex core boundary was insensitive to perturbations in the threshold around this value.

2.1.2 Eulerian Q-criterion

Another Eulerian scalar, the Q-criterion is employed to discern vortices based on the distinction it makes between shear and swirling flow (Hunt et al., 1988; Poelma et al., 2006; Lu and Shen, 2008; Yilmaz and Rockwell, 2012; Carr et al., 2013). The velocity gradient tensor $\nabla \boldsymbol{u}$ is decomposed into the symmetric rate of strain tensor $\boldsymbol{S}$ and antisymmetric rate of rotation tensor $\boldsymbol{\Omega}$, as,

$$\nabla \boldsymbol{u} = \boldsymbol{S} + \boldsymbol{\Omega}, \tag{2.3}$$

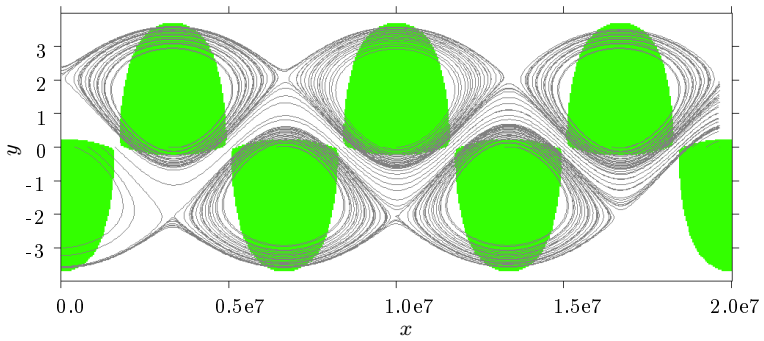

Figure 2-3: Visualization of Bickley jet flow field by green positive Q-criterion regions and streamlines (gray lines).

where $\boldsymbol{S} = \frac{1}{2}[\nabla \boldsymbol{u} + (\nabla \boldsymbol{u})^\top]$ and $\boldsymbol{\Omega} = \frac{1}{2}[\nabla \boldsymbol{u} - (\nabla \boldsymbol{u})^\top]$. $[\cdot]^\top$ indicates the matrix transpose. The Q criterion is then defined as,

$$Q = \frac{1}{2}[||\boldsymbol{\Omega}||^2 - ||\boldsymbol{S}||^2]. \tag{2.4}$$

In simple flows, especially simulations in two-dimensions, contours of $Q > 0$ can often be used to define vortices, which is interpreted as where local rotation dominates over local strain. A demonstration of Q-criterion is shown in figure 2-3 of the Bickley jet model compared to streamlines. The regions with positive Q-criterion are usually defined as vortex areas in simple flows, especially 2D simulations, such as in figure 2-3, where the vortex area of Bickley jet model is located by green positive Q-criterion regions.

In complex flows, notably 3D or turbulent experimental flows, contours of a certain percentage of Q_{max} are often used, for example $0.1Q_{max}$, in practical implementation. When noise is present in the system caused by uncertainty in the velocity measurements, the spatial gradients used to calculate the Q-criterion magnify the errors caused by the noise significantly, thus causing inherently noisy Q-criterion for experimental flows (Rockwood, 2017). For 3D or turbulent datasets, the vortex surface identified by a Q-criterion threshold appears significantly smoother, resulting in an easy interpretation, as well as allowing to distinguish individual vortices from a shear layer which is often difficult.

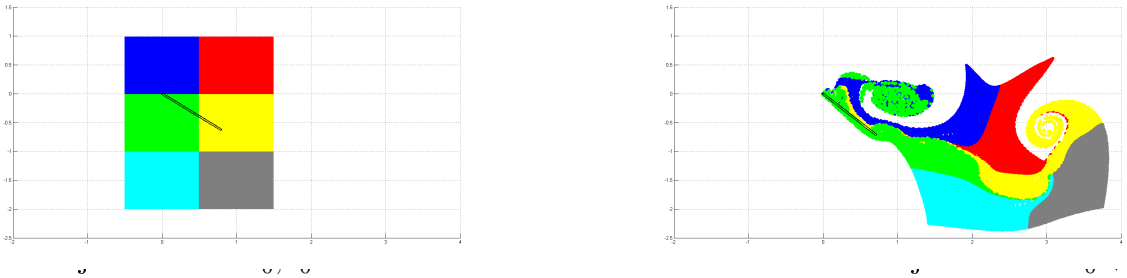

(a) Fluid trajectories at $\boldsymbol{x}_0, t_0$. (b) Location of fluid trajectories at $t_0 + \tau$.

Figure 2-4: Visualization of flow map in positive time.

2.1.3 Finite-time Lyapunov exponent

Building from the work of Haller (2002) and Shadden et al. (2005) provided a precise definition of the Finite-time Lyapunov exponent (FTLE), a scalar field that measures the maximum rate of Lagrangian separation around a certain location over a prescribed time interval.

Virtually all Lagrangian approaches are based on the flow map $\boldsymbol{\phi}(\boldsymbol{x}_0, t_0, \tau)$, a vector quantity defined on $\boldsymbol{x}_0$ at t_0, that maps fluid trajectories initiated at $\boldsymbol{x}_0, t_0$ to their final location in space after an integration time τ (shown in figure 2-4), thereby mimicking experimental flow visualization by tracers (Haller, 2015). In the visualization of the flow map, the trajectories initiated at $\boldsymbol{x}_0, t_0$ are colored by their location in figure 2-4(a), and the color distribution in their final location in figure 2-4(b) shows the separation of the trajectories from their neighboring trajectories due to their belonging to different partitions of flow dynamics, thus the flow map provides the separation information of the fluid trajectories of $\boldsymbol{x}_0$ at t_0 over the integration time τ. Several Lagrangian approaches also rely on the deformation gradient, $\partial\boldsymbol{\phi}(\boldsymbol{x}_0, t_0, \tau)/\partial\boldsymbol{x}_0$, comprised of the spatial derivatives of the flow map with respect to the initial location $\boldsymbol{x}_0$.

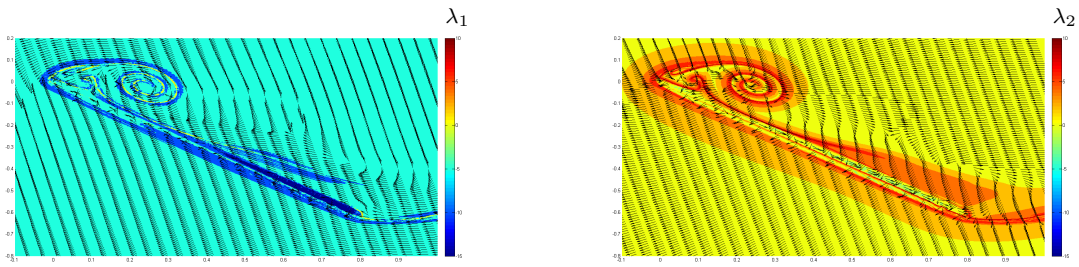

(a) λ_1 and $\boldsymbol{\xi}_1$ (b) λ_2 and $\boldsymbol{\xi}_2$

Figure 2-5: Visualization of eigenvalues and eigenvectors of 2D Cauchy-Green strain tensor.

To calculate FTLE at location $\boldsymbol{x}_0$ at time t_0, calculation of the flow map $\boldsymbol{\phi}(\boldsymbol{x}_0, t_0, \tau)$ and its deformation gradient $\partial\boldsymbol{\phi}(\boldsymbol{x}_0, t_0, \tau)/\partial\boldsymbol{x}_0$ are the first step. The Lagrangian stretching associated with the deformation gradient is captured by the Cauchy-Green strain tensor, which is defined as (Truesdell and Noll, 2004),

$$\boldsymbol{C}(\boldsymbol{x}_0, t_0) = \left[\frac{\partial\boldsymbol{\phi}(\boldsymbol{x}_0, t_0, \tau)}{\partial\boldsymbol{x}_0}\right]^\top \frac{\partial\boldsymbol{\phi}(\boldsymbol{x}_0, t_0, \tau)}{\partial\boldsymbol{x}_0}. \tag{2.5}$$

For a 2D velocity field, the Cauchy-Green strain tensor is symmetric and positive definite, we can get the positive eigenvalues (λ_i) and normalize the eigenvectors (ξ_i) (shown in figure 2-5) as follows:

$$\boldsymbol{C}(\boldsymbol{x}_0, t_0)\boldsymbol{\xi}_i = \lambda_i\boldsymbol{\xi}_i, i = 1, 2; 0 < \lambda_1 \leq \lambda_2; |\boldsymbol{\xi}_i| = 1; \boldsymbol{\xi}_2 \perp \boldsymbol{\xi}_1. \tag{2.6}$$

The maximum eigenvalue of the Cauchy-Green strain tensor is referred to as the coefficient of expansion σ_τ:

$$\sigma_\tau(\boldsymbol{x}_0, t_0, \tau) = \lambda_2(\boldsymbol{C}(\boldsymbol{x}_0, t_0)). \tag{2.7}$$

From there, the FTLE field is defined from the coefficient of expansion as:

$$FTLE(\boldsymbol{x}_0, t_0, \tau) = \frac{1}{2\tau}\log\sigma_\tau(\boldsymbol{x}_0, t_0, \tau). \tag{2.8}$$

Maximizing ridges in the FTLE field, which can either be explicitly extracted or (more commonly) visualized by viewing a contour plot (Lipinski and Mohseni, 2010), indicate high levels of Lagrangian stretching among nearby particle trajectories. For well-defined FTLE ridges computed using a sufficiently long integration time, the flux across the ridges is usually negligible (Shariff et al., 1989; Rom-Kedar et al., 1990; Guckenheimer and Holmes, 2013), and therefore delineate regions that exhibit qualitatively different dynamical behavior. For this reason, these ridges can represent vortex boundaries in a flow (Shadden et al., 2005; Haller, 2001, 2002).

While repelling ridges of FTLE can be calculated using forward-time integration, attracting ridges at time t_0 can be found by calculating FTLE using particle trajectories initialized at t_0 and integrated in negative-time. This calculation also yields a scalar FTLE field, but because it measures Lagrangian separation in negative time, its ridges represent those regions in the flow where particle trajectories are being attracted in physical (forward) time. By including ridges from both FTLE calculations, the analysis produces both the repelling FTLE ridges at t_0 along which particle trajectories locally are most prone to deviate from one another (positive-time, pFTLE), and attracting FTLE ridges at t_0 along which particle trajectories locally have contracted to each other (negative-time, nFTLE). pFTLE are analogous to the stable manifolds, and in contrast, nFTLE are associated with the unstable manifolds, both of which apply the notion of hyperbolic invariant manifolds to finite-time dynamics.

The pFTLE and nFTLE ridges at time t_0 intersect at the outer boundaries of vortices but do not overlap when there is low level of shear. Inclusion of both FTLE types provides a more complete boundary that delineates which particles are entrained into the vortex from those that continue to convect with the outer flow. Since the Q-criterion only visualizes the vortex cores, the ability to visualize the boundaries objectively provides additional insight into the vortex dynamics, especially when studying the interactions among coherent structures. The Bickley jet model is used to show the vortex detection by pFTLE and nFTLE ridges in figure 2-6. The boundaries of individual vortices of which are captured by the both the pFTLE and nFTLE ridges but not in previous Eulerian approaches. A representation of the vortex boundaries using FTLE ridges is obtained at

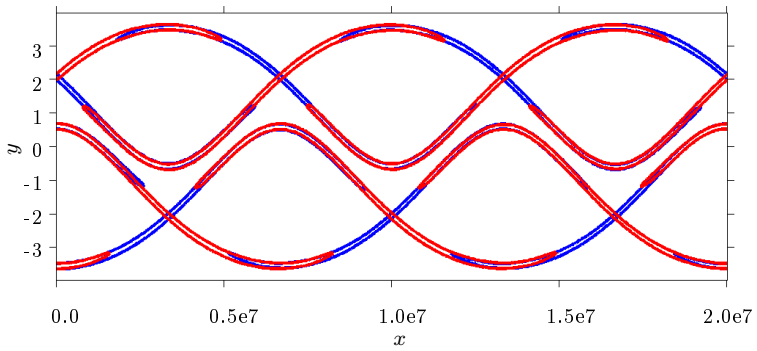

Figure 2-6: Visualization of Bickley jet flow field by positive- (blue) and negative-time (red) FTLE ridges.

later times in the flow evolution by reinitializing the flow map calculations (updating t_0), which is considered the 'standard' method by Lipinski and Mohseni (2010).

Compared to Eulerian criteria, using FTLE in vortex detection could avoid the sensitivity to short-term anomalies in the velocity field because it has been shown to be robust and relatively insensitive to imperfect velocity data (Haller, 2002). The mean location of the FTLE ridge got a minimal effect by the random velocity field noise as long as it remains a time-weighted sense (it has either small magnitude or short duration) (Olcay et al., 2010). It is important to note that changing the threshold value or integration time for FTLE ridge extraction does not change the location or shape of the coherent structures identified, only the thickness of the ridges (Shadden et al., 2005; Rockwood et al., 2016).

There is also scope for improvement in the practical application of FTLE. For example, it is important to check convergence of the FTLE values with system parameters, such as the temporal and dimensional resolution of experimental velocity data. While it is not uncommon to use a trajectory integration time step during flow map calculation that is smaller than the time between subsequent velocity data sets, the temporal resolution of the data must be sufficient so that interpolation techniques adequately recreate intermediate velocity fields when it is necessary (Rockwood et al., 2016). For inherently 3D flows, a single plane of data from stereoscopic PIV, even if it contains all three velocity components, may not be sufficient to generate an accurate Cauchy-Green strain

tensor and FTLE field. Particularly, vortices parallel to the data plane, such that the vortex-induced velocity will be normal to the plane, will not be captured (Rockwood, 2017). In those cases prior knowledge for orientations of both the vortex of interest and the data plane is critical for the success to capture the majority structures of the data plane by FTLE.

Finally, an outstanding issue is that it can be unclear what type of local separatrices the FTLE ridges represent (i.e., normally hyperbolic repulsion, Lagrangian shear, or tangential stretching) (Mezić et al., 2010; Allshouse and Peacock, 2015; Haller, 2015; Hadjighasem et al., 2017). In order to exact FTLE ridges that are indeed hyperbolic, the normal rate of Lagrangian strain $S_\perp$ can be examined along the identified ridges Haller (2002). The normal rate of Lagrangian strain is defined by equation 2.9,

$$S_\perp(\boldsymbol{x}_0, t_0) =< \boldsymbol{n}(\boldsymbol{x}_0, t_0), \boldsymbol{S}\boldsymbol{n}(\boldsymbol{x}_0, t_0) > . \tag{2.9}$$

Here, $\boldsymbol{S}$ represents the local rate of strain tensor, $\boldsymbol{n}(\boldsymbol{x}_0, t_0)$ is defined as a unit vector normal to the target FTLE ridges, and $< \cdot >$ denotes inner product operation.

A positive value of normal rate of Lagrangian strain $S_\perp$ indicate a hyperbolically repelling FTLE ridge, while a negative value reveals hyperbolically attracting FTLE ridges (Mathur et al., 2007). The method is applied to different flow phenomena, such as hyperbolic material line detection in 2D turbulent flow (Mathur et al., 2007), the evolution of hairpin vortices in turbulent boundary layers (Green et al., 2007), and the forecast for the major short-term changes in oceanic contamination patterns of oil spills Olascoaga and Haller (2012).

2.1.4 Geodesic LCS

The geodesic theory of LCSs is a collection of global variational principles for material transport barrier, which includes elliptic LCS, hyperbolic LCS and parabolic LCS (Haller and Beron-Vera, 2012). By an analogous study of LCSs with black holes by Haller and Beron-Vera (2013) and Haller (2015), the above LCSs coincide with null-geodesics of appropriately defined Lorentzian metrics. In this thesis, we only discuss the application

of hyperbolic LCS, herein the term LCS will refer to a hyperbolic LCS only.

By the geodesic definition of LCSs, Haller and Beron-Vera (2012) and Farazmand and Haller (2012a) argue that repelling LCSs in 2D flows are least-stretching strainlines in a forward time interval. Similarly, attracting LCS are defined as least-stretching strainlines in backward time over the same time interval. By solving the Lorentzian metrics, the repelling LCSs turn out to be the material lines that are everywhere tangent to the field of unit eigenvectors $\boldsymbol{\xi}_1(\boldsymbol{x}_0)$ associated with the smaller eigenvalue field $\lambda_1(\boldsymbol{x}_0)$ of the Cauchy-Green strain tensor $\boldsymbol{C}(\boldsymbol{x}_0, t_0)$ from equation 2.6 (Farazmand and Haller, 2012b, 2013). In practice, repelling LCSs are computed, in a way similar to the computation of streamlines from the velocity field (Miron and Vétel, 2015).

To calculate the repelling LCS at time t_0 in a 2D flow, it starts from the calculation of the flow map $\boldsymbol{\phi}(\boldsymbol{x}_0, t_0, \tau)$ (blue arrow in figure 2-7) over the time interval of interest $[t_0, t_1]$ (black arrow in figure 2-7, where $t_1 = t_0 + \tau$). Then we obtain the repelling Cauchy-Green strain tensor $\boldsymbol{C}_{rep}(\boldsymbol{x}_0, t_0)$ with the particle trajectories repelling information over the time interval $[t_0,\ t_1]$ by equation 2.5, and its eigenvalues $\lambda_i(\boldsymbol{x}_0, t_0)$ and eigenvectors $\boldsymbol{\xi}_i(\boldsymbol{x}_0, t_0)$. The repelling LCSs at t_0 are calculated as trajectories, i.e., loci of points $\boldsymbol{r}$ from a set of grid points satisfying the following ordinary differential equation (ODE) of the eigenvectors $\xi_1(\boldsymbol{r}, t_0)$,

$$\boldsymbol{r}' = \boldsymbol{\xi}_1(\boldsymbol{r}, t_0). \tag{2.10}$$

In practice, the above procedure starts with the selection of initial coordinates that satisfy two criteria: the first criterion states that the normal repulsion rate (the larger eigenvalue $\lambda_2(\boldsymbol{r}, t_0)$ of the repelling Cauchy-Green strain tensor $\boldsymbol{C}_{rep}(\boldsymbol{x}_0, t_0)$) computed along the repelling LCS is larger than the tangential stretching rate (the smaller eigenvalue $\lambda_1(\boldsymbol{r}, t_0)$) i.e. $\lambda_2(\boldsymbol{r}, t_0) > \lambda_1(\boldsymbol{r}, t_0)$ (Haller, 2011; Onu et al., 2015); the second ensures the repelling LCS has a local maximum repulsion rate $\lambda_2(\boldsymbol{r}, t_0)$ among all other material lines. The procedure is carried on until either the boundary of the domain is reached or pre-set maximum LCS length is reached.

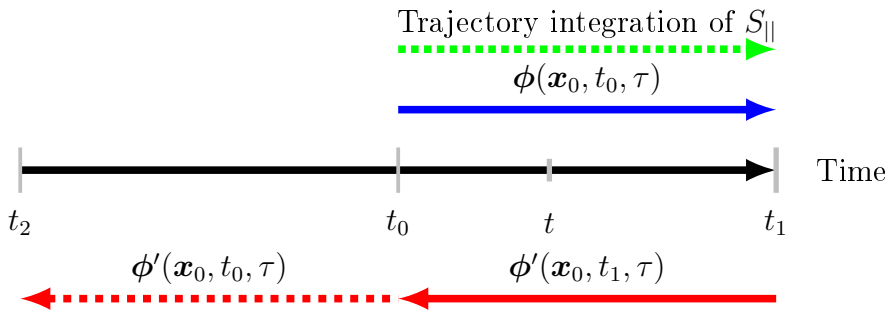

Figure 2-7: Schematic of flow maps.

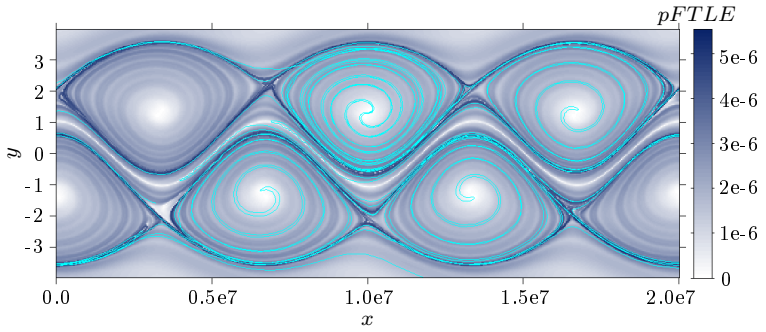

Figure 2-8: Visualization of Bickley jet flow field by repelling LCS (cyan lines) and pFTLE contour.

The repelling LCS in the Bickley jet model is demonstrated in figure 2-8, in which the pFTLE contour is shown for comparison as well. In this case, the repelling LCSs match with the bright pFTLE ridges well.

The calculation of attracting LCSs at time t_1 starts with the flow map $\boldsymbol{\phi}'(\boldsymbol{x}_0, t_1, \tau)$ (red arrow in figure 2-7) over the same dynamical system over $[t_0,\ t_1]$ but in negative time. Thus by equation 2.5, we gain the attracting Cauchy-Green strain tensor $\boldsymbol{C}_{att}(\boldsymbol{x}_0, t_1)$ with the particle trajectories attracting information over the time interval $[t_0,\ t_1]$, and its eigenvalues $\lambda_i(\boldsymbol{x}_0, t_1)$ and eigenvectors $\boldsymbol{\xi}_i(\boldsymbol{x}_0, t_1)$. The attracting LCSs are locus of points $\boldsymbol{r}$ solved by ODE equation 2.10 with eigenvectors $\boldsymbol{\xi}_1(\boldsymbol{r}, t_1)$ from the attracting Cauchy-Green strain tensor $\boldsymbol{C}_{att}(\boldsymbol{x}_0, t_1)$ with the same procedure as described above. As proved by Farazmand and Haller (2013), the forward repelling LCS coincides with the backward attracting LCS, and the backward repelling LCS coincides with the forward

attracting LCS when calculated in the same time interval of interest.

By the procedure described above and full available data over the time interval of interest $[t_0, t_1]$, we can get the repelling LCS of t_0 and attracting LCS of t_1. To get the complete and dynamically consistent LCS at any time t of the interval $(t_0 \leq t \leq t_1)$), the repelling LCS of t_0 needs to be advected forward by the flow map $\boldsymbol{\phi}(\boldsymbol{x}_0, t_0, \tau)$ (blue arrow in figure 2-7) from t_0 to t to get repelling LCS of t (Farazmand and Haller, 2012a, 2013). Similarly, the attracting LCS of t_1 needs to be advected backward by the flow map $\boldsymbol{\phi}'(\boldsymbol{x}_0, t_1, \tau)$ (red arrow in figure 2-7) from t_1 to t to get attracting LCS of t. The geodesic LCS method is an automated and objective vortex detection approach, as well as a mathematically rigorous and sophisticated scheme by support of exact variational principles. There remain some practical challenges for its application, such as the fact that it involves heavy computation and is sensitive to a large number of numerical input parameters; it is too restrictive for some weak coherent structures as it only detects the most coherent LCSs (Hadjighasem et al., 2017).

2.1.5 Lagrangian saddle

In vortex dominated flow, a Lagrangian saddle (or hyperbolic stagnation point) is a time-varying location at which particles consisted of attracting LCS approach asymptotically while particles consisted of repelling LCS repel from asymptotically (Balasuriya, 2012; Balasuriya and Padberg-Gehle, 2014; Balasuriya et al., 2016). Lagrangian saddles have been shown to be dynamically important features as components of vortex boundaries (Green et al., 2011; Mulleners and Raffel, 2012), and can be used for vortex tracking (Huang and Green, 2015; Rockwood et al., 2016) that yields insight into the behavior of the vortices in various vortex dominated flow.

In practice, there is no universally agreed-upon definition for Lagrangian saddle. The research by Voth et al. (2002) identifies a Lagrangian saddle as the intersection between an nFTLE ridge, corresponding to the unstable manifold, and a pFTLE ridge, corresponding to the stable manifold. In this thesis, the Lagrangian saddles identified in this way will be referred to as FTLE-saddles.

A more recent method (Olascoaga and Haller, 2012), termed LCS-core analysis, con-

cluded that a point $\boldsymbol{r}$ that lies on an attracting LCS of time t_1 (a locus of finite number of points calculated in a time interval (t_0, t_1)) is a Lagrangian saddle over the time interval of interest $[t_0,\ t_1]$ if its normal rate of Lagrangian strain $S_\perp(\boldsymbol{r}, t) =< \boldsymbol{n}(\boldsymbol{r}, t), \boldsymbol{S}\boldsymbol{n}(\boldsymbol{r}, t) >$ stays negative for all the time t $(t_0 \leq t \leq t_1))$ when advected backward by the flow map $\boldsymbol{\phi}'(\boldsymbol{x}_0, t_1, \tau)$ (red arrow in figure 2-7) from t_1 to t. Here, $\boldsymbol{n}(\boldsymbol{r}, t)$ is defined as a unit vector normal to the target attracting LCS at an arbitrary time t during the backward advection.

Similarly, Miron and Vétel (2015) proposed a method extracting a Lagrangian saddle from an attracting LCS by an exponent λ related to the tangential rate of Lagrangian strain $S_{||}$ based on the previous work of Haller and Iacono (2003), Haller (2004) and Lekien and Haller (2008). These Lagrangian saddles are computed and referred to as λ-saddle in this thesis. The Lagrangian λ-saddle over the time interval of interest $[t_0,\ t_1]$ is defined as the hyperbolic point $\boldsymbol{r}$ that maximizes the $\lambda(\boldsymbol{r}, t_0, t_1)$ exponent along the attracting LCS of time t_0 (Miron et al., 2015). The attracting LCS of time t_0 is calculated in a time interval $[t_2, t_0]$, where $t_2 = t_0 - \tau$, by flow map $\boldsymbol{\phi}'(\boldsymbol{x}_0, t_0, \tau)$ (red dashed arrow in figure 2-7). The $\lambda(\boldsymbol{r}, t_0, t_1)$ exponent, defined as in equation 2.11, is computed for all points $\boldsymbol{r}$ of the attracting LCS of t_0, and is a trajectory integral of the tangential rate of Lagrangian strain $S_{||}$ (green dotted arrow in figure 2-7) of each point $\boldsymbol{r}$ for all the time t $(t_0 \leq t \leq t_1))$ when the points are advected forward by the flow map $\boldsymbol{\phi}(\boldsymbol{x}_0, t_0, \tau)$ (blue arrow in figure 2-7) from t_0 to t_1 (Miron and Vétel, 2015).

$$\lambda(\boldsymbol{r}, t_0, t_1) = \int_{t_0}^{t_1} S_{||}(\boldsymbol{r}, s) ds, \tag{2.11}$$

where the tangential rate of Lagrangian strain $S_{||}$ is defined as,

$$S_{||}(\boldsymbol{r}, t) =< \boldsymbol{e}(\boldsymbol{r}, t), \boldsymbol{S}\boldsymbol{e}(\boldsymbol{r}, t) > . \tag{2.12}$$

Here, $\boldsymbol{e}(\boldsymbol{r}, t)$ is defined as a unit vector along and tangent to the target attracting LCS at an arbitrary time t during the advection. As proved by Haller and Iacono (2003), for incompressible flow $S_{||}(\boldsymbol{r}, t) = -S_\perp(\boldsymbol{r}, t)$.

Note that, the attracting LCS of time t_0 consists of finite number of points extracted from a set of grid points satisfying equation 2.10 and the calculation criteria. The tangential unit vector $\boldsymbol{e}(\boldsymbol{r}, t)$ of each point $\boldsymbol{r}$ during the forward advection by flow map $\boldsymbol{\phi}(\boldsymbol{x}_0, t_0, \tau)$ can be solved by setting $e = (\cos\theta, \sin\theta)$ for $\boldsymbol{r}$ at t_0 and equation 2.13:

$$\dot{\theta} = v_x \cos^2\theta - u_y \sin^2\theta + (v_y - u_x)\cos\theta\sin\theta. \tag{2.13}$$

Alternatively, Dellnitz and Junge (2002); Balasuriya (2011); Balasuriya and Padberg-Gehle (2014); Balasuriya et al. (2016) proposed some analytical and numerical methods to extract Lagrangian saddles, termed as hyperbolic neighborhoods, which is beyond the scope of this thesis.

2.1.6 Lagrangian-Averaged Vorticity Deviation

A majority of researchers (Haller, 2005; Chakraborty et al., 2005) view vortex cores as regions where both swirling motion and small particle separation govern the flow. To capture both main features of a vortex, Haller et al. (2015) proposed an objective vortex criteria called Lagrangian-Averaged Vorticity Deviation (LAVD).

LAVD is defined as the trajectory integral of the normed vorticity deviation from its spatial mean around a certain location in space $\boldsymbol{x}_0$ from time t_0 to t, as

$$LAVD^t_{t_0}(\boldsymbol{x}_0) = \int_{t_0}^{t} |\boldsymbol{\omega}(\boldsymbol{x}(\boldsymbol{s}; \boldsymbol{x_o}), \boldsymbol{s}) - \bar{\boldsymbol{\omega}}(\boldsymbol{s})| ds. \tag{2.14}$$

where $\bar{\boldsymbol{\omega}}$ is the instantaneous spatial mean of vorticity, and $\boldsymbol{s}$ is the coordinate along a Lagrangian trajectory initialized at $\boldsymbol{x}$.

A rotationally coherent Lagrangian vortex is defined as a nested set of outward decreasing tubular level sets of LAVD. The Lagrangian vortex boundary is defined as the outermost closed convex level surface of LAVD, satisfying convexity deficiency (ensuring a round structure) and arc-length thresholds (eliminating numerical or observational noise), while the vortex center is defined as singular level sets (local maxima) of LAVD enclosed by an LAVD boundary. The vortex detection by LAVD in the Bickley jet model is

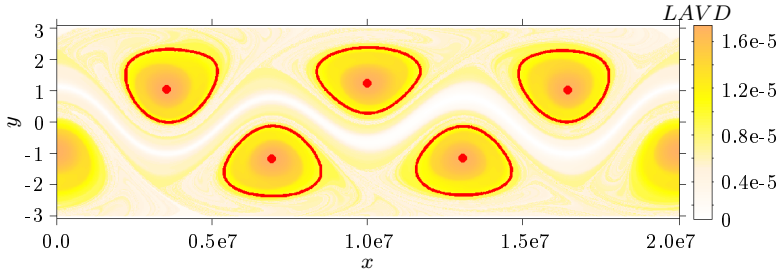

Figure 2-9: Visualization of Bickley jet flow field by LAVD contour. Vortex boundaries and centers are shown as red circles and spots.

visualized in figure 2-9, and LAVD boundaries and centers identify the vortex boundaries and centers in the flow.

LAVD is obtained from the exact, dynamically consistent Dynamic Polar Decomposition (DPD) (Haller, 2016) of fluid element finite deformation, thus it provides a fully frame invariant, and not subject to individual judgment, thresholding vortex criterion, avoiding trial and error implementation in complex 3D flow or material convection flow. Furthermore, LAVD can provide a complete vortex boundary definition and has benefits for vortex strength study. However, it requires some user input (the maximal convexity deficiency and the minimal spatial scale), and requires a large enough computational domain for practical application (Hadjighasem et al., 2017).

2.1.7 Circulation

Vortex strength is measured by circulation as it characterizes the vorticity flux into a prescribed vortex area. Thus the circulation of an LEV is related to the lift development over the aerodynamic surface (Ringuette et al., 2007; Carr et al., 2013), and the increase of the circulation indicates a vorticity flux into the vortex area. The circulation Γ of a vortex is defined as in equation 2.15:

$$\Gamma = \oint \boldsymbol{u} \cdot dl. \tag{2.15}$$

In this thesis, the vorticity is sampled at discrete spatial locations. By the Stokes

Theorem, the instantaneous circulation can then be obtained by integrating its vorticity within the vortex area:

$$\Gamma = \sum_{i=1}^{N} \boldsymbol{\omega} \cdot dS. \tag{2.16}$$

Here, the total vortex area S is the finite enclosing vortex area defined for circulation calculation. N is the number of discrete area elements inside S.

In vortex circulation study, special care needs to be taken in vortex area definition. Although studies on vortex dynamics have been carried out for decades, a widely-accepted, objective definition of a vortex and its boundaries and areas remains an open question. A consistently defined vortex area, especially in study of circulation development, is critical to the result. The area definition is more complicated when the vortex is fed by a shear layer, as the boundary between the vortex and the shear layer is unclear. Several application-specific manners of vortex area definition, based on different vortex definition approaches, are applied in the following chapters for different data sets. The resulting circulation developments are compared for a further discussion of different vortex criteria performance in vortex circulation study.

2.2 Vortex shedding mechanisms

2.2.1 Optimal vortex formation

The optimal vortex formation theory (Dabiri, 2009) suggests that the optimality of propulsion can be achieved by maximizing the vortex size and strength. The key concept in the optimal vortex formation is the dimensionless vortex formation time $\hat{T}$, defined by the instantaneous vortex circulation Γ as well as the vortex-feeding shear layer velocity U (U is originally the jet velocity from the piston-cylinder apparatus in the vortex ring generation (Gharib et al., 1998)), and the characteristic length scale D (cylinder exit of the piston-cylinder apparatus in vortex ring generation (Gharib et al., 1998)), respectively (Mohseni et al., 2001; Dabiri, 2009):

$$\hat{T} = \frac{C\Gamma}{DU}, \tag{2.17}$$

where C is a constant factor depending on the physical configuration of a given vortex generator, and is given by the inverse of the dimensionless vorticity flux $d\hat{\Gamma}/d\hat{T}$ from the vortex generator configuration. In the piston-cylinder apparatus for vortex ring generation, the dimensionless vorticity flux $d\hat{\Gamma}/d\hat{T} \simeq 1/2$ (Didden, 1979), then the parameter C is equal to 2 in the case. Dabiri (2009) proposed the constant factor C to make sure the change of formation number $N = 4$ (defined as the formation time at which pinch-off happens from piston-syliner apparatus) is independent of the vorticity flux from the vortex generator. Thus only the influence of parameter Γ, D and U on the formation number will be shown by comparing the resulting formation number to the universal formation number $N = 4$ for a comparison across the various apparatus of vortex shedding.

Some physical intuition on the vortex formation process limitations is indicated by equation 2.17, such as larger vortex circulation tends to advance formation number, while either a stronger shear layer or a longer shear layer from the vortex generator tends to delay the formation number. With the framework of optimal vortex formation, the optimal design strategies that involve combinations of various aforementioned parameters can be applied for engineering design assessment.

A series of research (Mohseni et al., 2001; Dabiri and Gharib, 2005; Milano and Gharib, 2005; Krueger et al., 2006; Dabiri, 2009) applied the optimal vortex formation concept to flapping flight, and modified the definition of formation time $\hat{T}$ accounting for the varying velocity distribution and vortex generator configuration.

In the study of flapping flight of this thesis, vortex circulation Γ in equation 2.17 is approximated by equation 2.18,

$$\Gamma \approx \frac{U_\infty}{\cos(\alpha)} \frac{U}{\delta} t\delta, \tag{2.18}$$

Here the flux of vorticity-containing mass into the vortex is represented by the advection of vorticity flux from the uniform feeding shear layer with velocity $U_\infty/\cos(\alpha)$ over the plate with thickness δ (Dabiri, 2009; Sattari et al., 2012; Rival et al., 2014). The vorticity generated at the leading edge can be approximated by the vortex-feeding shear layer velocity U divided by the characteristic shear layer thickness δ.

Equation 2.17 is then simplified to calculate the optimal formation time as follow:

$$\hat{T} \approx \frac{CU_\infty t}{c\cos(\alpha)}, \tag{2.19}$$

where the characteristic length scale D implies the geometry-related limit of vortex growth, e.g., nozzle opening, cylinder diameter, or airfoil chord, which in the current work is chosen as the plate length c (Sattari et al., 2012; Rival et al., 2014). In addition, t is the dimensionless time, and α is the instantaneous plate angle of attack. In the case of chapter 3, the plate angle of attack α remains 45° during the period of interest, and when setting $C = 1$ the dimensionless vorticity flux $d\hat{\Gamma}/d\hat{T} = \sqrt{2}/2$, thus $C = \sqrt{2}$ (as the reverse of dimensionless vorticity flux) is chosen in this study.

2.2.2 Vortex shedding mechanism

According to the Vortex shedding mechanism (VSM) proposed by Boghosian and Cassel (2016), the necessary and sufficient conditions of vortex separation for any 2D, incompressible flow are (1) the existence of a location with zero momentum and (2) the same location having the presence of a net force with a positive divergence. More specifically, VSM states that the existing vortex will undergo a separation at a location where if and only if:

(1) There is a zero-momentum point as defined with following stream function (Ψ) condition,

$$\frac{\partial \Psi}{\partial x} = \frac{\partial \Psi}{\partial y} = 0. \tag{2.20}$$

(2)The divergence of the net force is positive, which can be expressed as follows:

$$\nabla \cdot \boldsymbol{f_{net}} = -\nabla^2 p + \nabla \cdot \boldsymbol{f_b}. \tag{2.21}$$

for incompressible flow.

In this thesis, this condition becomes the presence of a positive pressure streamwise gradient because no body force is present. As demonstrated by its definitions, vortex separation detected by VSM is supposed to be independent of Re, study case geometry,

and net force source.

Chapter 3

Vortex formation and shedding in two-dimensional massively separated flows

In this chapter, vortex visualization, tracking, and strength calculation using both Eulerian and Lagrangian methods were applied to a numerical 2D example data set to reveal the occurrence of physically-significant phenomena in massively-separated flows.

3.1 Test case

To obtain a better understanding of vortex shedding in flapping flight, it is useful to break such a complex problem into simpler sub-problems. Compared to the whole system, a sub-problem approach focuses on more sophisticated models progressively. There are several goals of this approach: it pays attention to individual phenomena, such as the influence of single vortex dynamics on leading edge vortex shedding events in these scenarios, before including more complicated phenomena like vortex interactions; it also serves as a benchmark for comparisons between various experiments, computations and theories from independent researchers, within a manageable parameter space and simplified systematic framework (Buchner, 2016); finally, it serves as a validation exercise for the development of numerical algorithms and experimental apparatuses (Eldredge,

2007).

In the spirit of a sub-problem approach, this chapter focuses on one such canonical case, a simulation of the flow at $Re = 1000$ surrounding a flat plate in the process of a 45° pitch-up maneuver generated by Eldredge (2007). The Re of this case lies in the range of typical flight experienced by insects, thus is relevant to the design and miniaturization of MAVs (Ol et al., 2009). This data set has been distributed among the Massively Separated Flows Discussion Group of the American Institute of Aeronautics and Astronautics (AIAA) Fluid Dynamics Technical Committee (FDTC), in an effort to share insight into the canonical case as the simplification of the problems of unsteady airfoils or unsteady flow over airfoils problem.

An instantaneous snapshot of the flow field of the data is shown in figure 3-1 by streamlines and vorticity contour. Figure 3-2 shows the plate angle of attack α (the angle between the plate and the freestream) change in dimensionless formation time. During this motion, there is formation and shedding of a large scale leading edge vortex (LEV) and trailing edge vortex (TEV), the dynamics of which are shown to correlate with the fluctuation of lift on the plate (Wang and Eldredge, 2013).

3.2 Analysis implementation

Mechanisms of LEV shedding in the canonical case are examined by approaches introduced in chapter 2. Most of the popular vortex identification schemes can only provide partial information (Sadlo and Peikert, 2009), i.e. vortex center, or boundary, or core area, thus different combinations of multiple vortex criteria are necessary for a complete comprehension of vortex dynamics during LEV shedding.

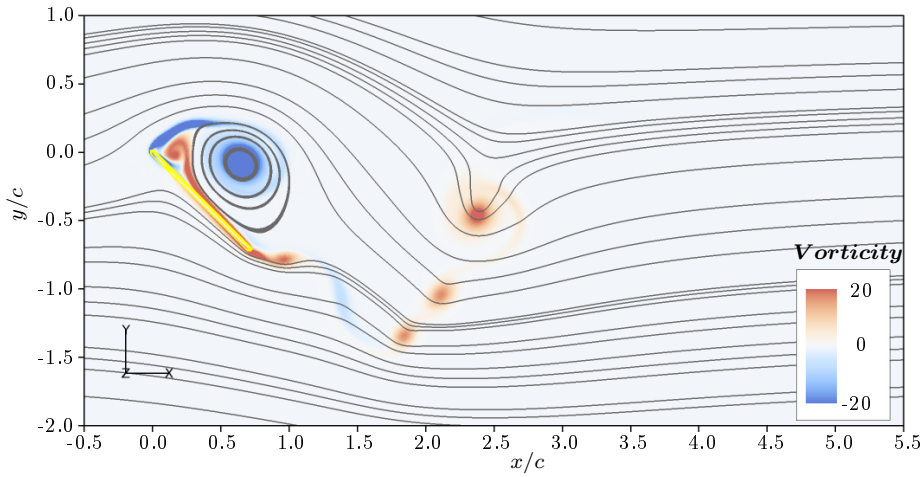

Figure 3-1: Instantaneous snapshots of the primary LEV shedding process visualized by vorticity contour and instantaneous streamlines at $\hat{T} = 6.0$. Flat plate is shown as a yellow line.

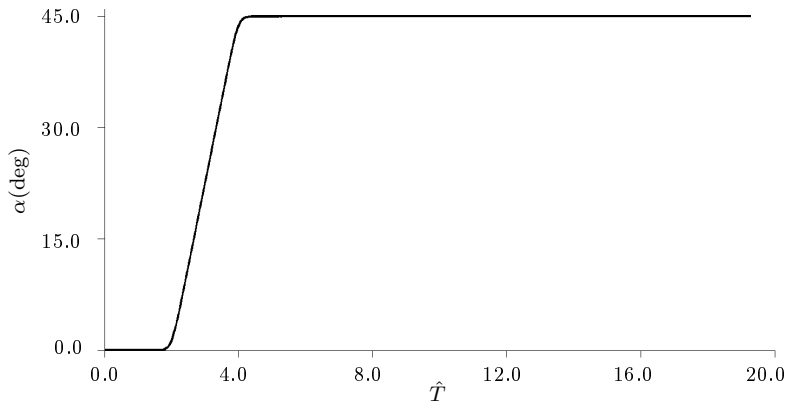

Figure 3-2: Angle of attack (α) of the plate with respect to formation time $\hat{T}$.

3.2.1 Vortex center and boundary identification

Demonstration of vortex core area, center and boundary detections are shown in figure 3-3. In that figure, the LEV center is first found using the Γ_1 function, which is shown as the orange spot in the center of the vortex core area visualized by positive Q-criterion.

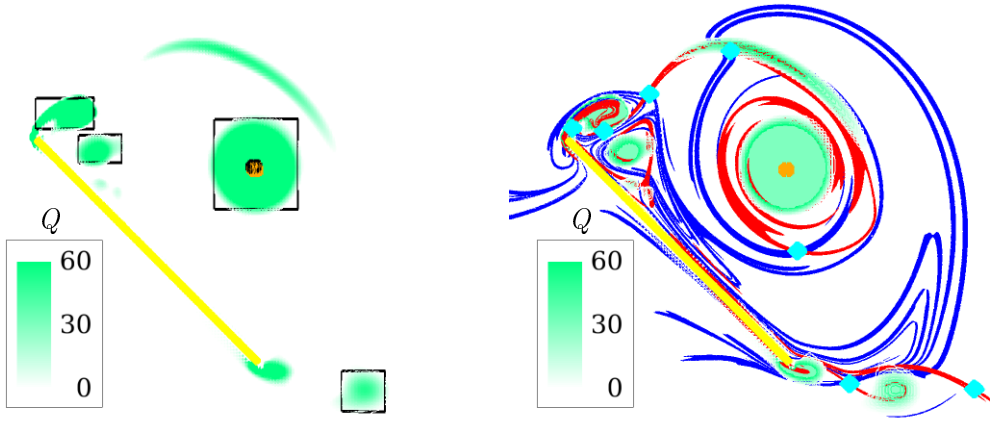

(a) Vortex center identification (b) Vortex boundary identification.

Figure 3-3: Examples of vortex identification methods. Positive Q-criterion contour (green) defines vortex core area. Negative- and positive-time FTLE ridges are shown as red and blue ridges respectively, with contour level of values more than 85% maximum. Γ_1 function, Q-criterion centers, and FTLE-saddles are orange, black and cyan spots, separately.

Another method to locate vortex center uses the Q-criterion by first identifying a rectangular area around the Γ_1 center that roughly bounds the region of $Q > 0$ (separating vortex core from shear layer). Starting from the Γ_1 center, the rectangular sides are tangent to the farthest point of $Q = 0$ at up, down, right and left directions. The vortex center by the Q-criterion is defined as the 'center of mass' of the Q-criterion in that rectangular region (defined as in equation 3.1), shown as the black boxes and black spot in figure 3-3(a).

$$\boldsymbol{C} = \frac{\sum_{i=1}^{n} Q_i \boldsymbol{c}_i}{\sum_{i=1}^{n} Q_i}, \tag{3.1}$$

In equation 3.1, n is the number of points with $Q > 0$ inside the rectangular region; Q_i is the value of Q at each point, and $\boldsymbol{c}_i$ is spatial coordinate of each point. In the present case, we found these two centers generally, but not exactly, locate the vortex center at the same location.

For vortex boundary identification, we also compared several methods involving dif-

ferent Lagrangian vortex criteria. In figure 3-3(b), the LEV boundaries are identified by positive- (blue) and negative-time (red) FTLE ridges wrapping around vortex area. The nFTLE ridges are calculated using a $\tau = 2.0$ integration time, and $\tau = 4.0$ for pFTLE ridges. The cyan dots mark FTLE-saddles, and are used for vortex tracking during the flow evolution as they locate on the vortex boundaries (Huang and Green, 2015). Among all the FTLE-saddles, only FTLE-saddles observed surrounding and convecting consistently with the LEV are tracked and analyzed in this thesis.

Figure 3-4 presents the behavior of material particles, initially located in the vicinity of an FTLE-saddle and its connecting pFTLE and nFTLE ridges at $\hat{T} = 5.4$, at four instantaneous moments during their advection by flowmap. This is demonstrated and compared with the nFTLE, pFTLE ridges and FTLE-saddles shown in the background, which are calculated at the four instants $\hat{T} = 5.4$, 5.6, 5.8 and 6.1 respectively, by the 'standard' method introduced in section 2.1.3. Each quadrant of particles divided by the initial FTLE ridges is assigned one solid color. Any particles found on the initial pFTLE ridge with finite thickness are colored blue while those on the initial nFTLE ridges are colored red, and particles found at the area where two ridges overlapping are colored black.

There is a clear motion of particles away from the pFTLE ridge, and along the nFTLE ridge, remaining tangent to the ridges, which agrees with the expected behavior of particles in the vicinity of a Lagrangian saddle. The Lagrangian saddle behavior is further observed in the thickening and compressing of the blue ridge initially containing particles on the pFTLE ridge at $\hat{T} = 5.4$ as the nearby particles are repelled away, and a narrowing and stretching of the red ridge initially containing particles on the nFTLE ridge at $\hat{T} = 5.4$ as the particles are attracted closer. All the new FTLE-saddles identified by the 'standard' method at each instantaneous moment $\hat{T} = 5.4$, 5.6, 5.8 and 6.1, appear to overlap with the particles initially located at the FTLE-saddle at $\hat{T} = 5.4$ and convected by the flow map. This implies that the FTLE-saddles extracted by the 'standard' method are indeed Lagrangian saddles, since the same dynamics are found for each FTLE calculation.

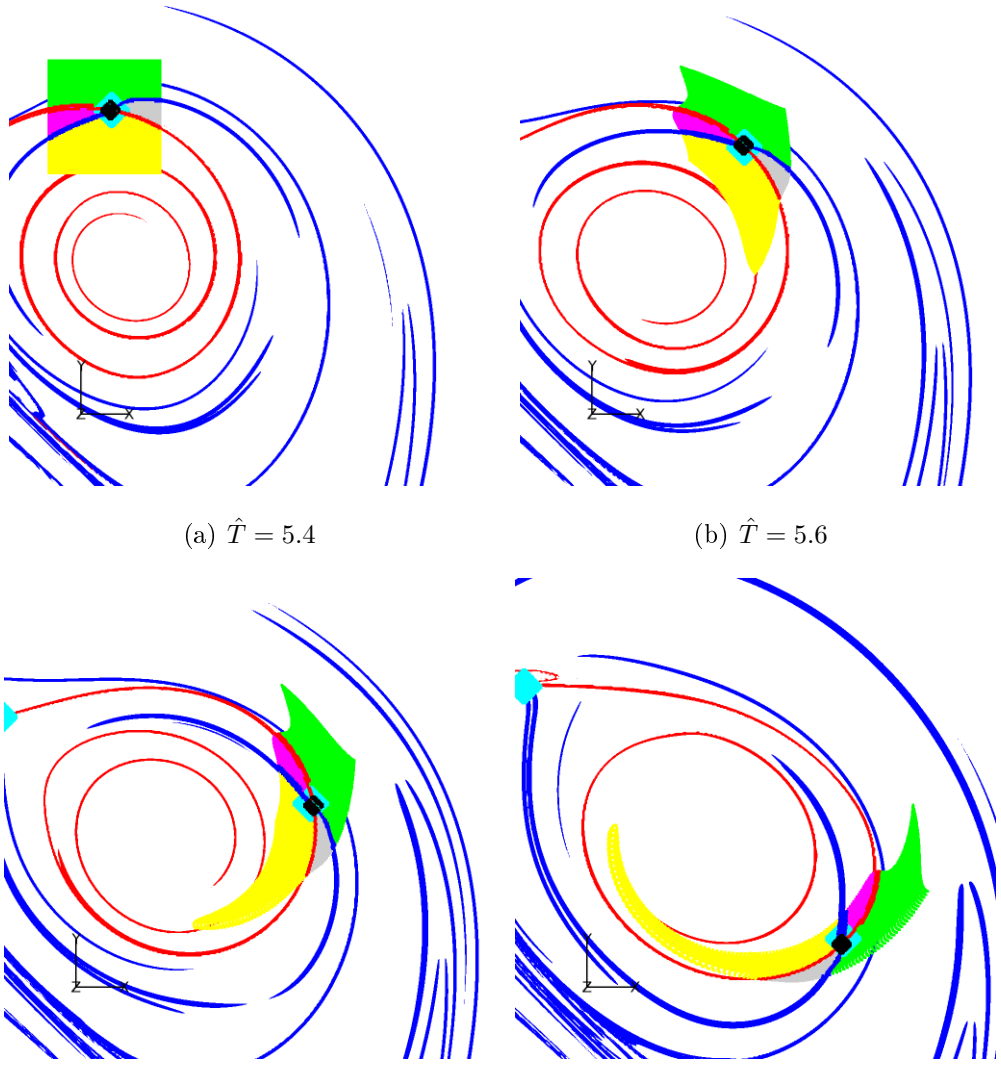

(a) $\hat{T} = 5.4$ (b) $\hat{T} = 5.6$

(c) $\hat{T} = 5.8$ (d) $\hat{T} = 6.1$

Figure 3-4: Lagrangian particle evolution around an FTLE-saddle identified at $\hat{T} = 5.4$. Particles are colored by their initial locations as described in the text. Negative- and positive-time FTLE ridges calculated by the 'standard' method at every instantaneous moment are shown as red and blue ridges respectively, with contour level of values more than 90% maximum. FTLE-saddles calculated by the 'standard' method at every instantaneous moment are shown as cyan spots.

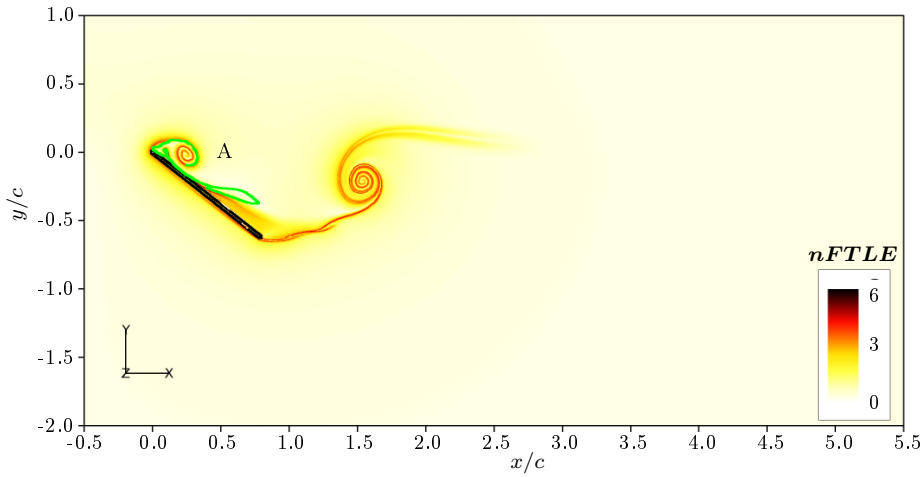

(a) $\hat{T} = 3.7$

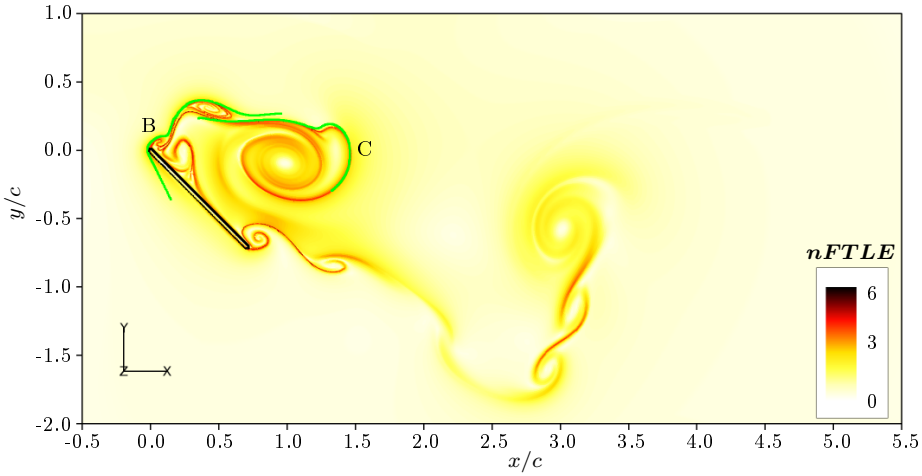

(b) $\hat{T} = 7.7$

Figure 3-5: Visualization of LEV shedding process by nFTLE contour and attracting LCS at $\hat{T} = 3.7$ and $\hat{T} = 7.7$. Flat plate is shown as black line.

Figure 3-5 shows the vortex boundary using attracting LCS (introduced by geodesic LCS in section 2.1.4) at $\hat{T} = 3.7$ and $\hat{T} = 7.7$. One or two attracting LCS are captured at each instant, which are marked 'A' in figure 3-5(a) and 'B' and 'C' in figure 3-5(b), separately. Compared with the nFTLE contours, attracting LCS A, B and C all coincide with the nFTLE ridges wrapping around the LEV and feeding shear layer in the LEV vicinity.

Attracting LCS A is calculated backward by the flow map $\boldsymbol{\phi}'(\boldsymbol{x}_0, t_0, \tau)$ (red dashed arrow in figure 2-7) from $\hat{T} = 3.7$ right after the LEV is formed, with an integration

time of $\tau = 2$, similar to the nFTLE calculation. Alternatively, attracting LCS B and C are calculated backward using the flow map $\boldsymbol{\phi}'(\boldsymbol{x}_0, t_1, \tau)$ (red arrow in figure 2-7) with integration time $\tau = 4$ and shown in the end of the period of interest $\hat{T} = 3.7 - 7.7$, during which the LEV sheds. In the following calculation for the λ-saddle along these LCSs, attracting LCS B and C are convected by flow map $\boldsymbol{\phi}'(\boldsymbol{x}_0, t_1, \tau)$ (red arrow in figure 2-7) backward to the beginning of the period of interest to show attracting LCS B and C at $\hat{T} = 3.7$, as done by Farazmand and Haller (2012a) and Olascoaga and Haller (2012).

The λ values along all three attracting LCS are computed from $\hat{T} = 3.7$ to $\hat{T} = 7.7$ by trajectory integration (green dotted arrow in figure 2-7) and have 3D contours as shown in figure 3-6. The λ values are visualized as a 3D surface for which the x-axis is the curvilinear coordinate s along the attracting LCS A, B, and C, the y-axis is the integration time τ, and the z-axis and the contour color indicates the magnitude of the λ value.

As integration time τ increases, the $\lambda(x_0, t_0, t)$ values gradually reveal the existence of several hyperbolic points (marked by green markers in figure 3-6) maximizing the Lagrangian strain rate, allowing the extraction of the λ-saddles along each attracting LCS respectively, as shown in figure 3-7. In figure 3-6(a), there are several hyperbolic points (λ peaks) at $s < 0.6$, which are not identified as λ-saddles of the LEV. This is because the attracting LCS A, which separates the plate shear layer from both the LEV and the free stream extends beyond the the LEV boundary (as shown in figure 3-5(a)), and thus contains particles (locating at $0 < s < 0.6$) that do not entrain into or convect along the LEV.

All the λ-saddles extracted at the end of the integration time are tracked backward using the flow map $\boldsymbol{\phi}'(\boldsymbol{x}_0, t_1, \tau)$ (red arrow in figure 2-7) to their locations in each time instant. In practice, the number of λ-saddles extracted along each attracting LCS is determined by all the hyperbolic points that remain a local maxima of λ over the longest τ. The calculation characteristics of all the Lagrangian criteria applied in the case are summarized in table 3.1 for comparison.

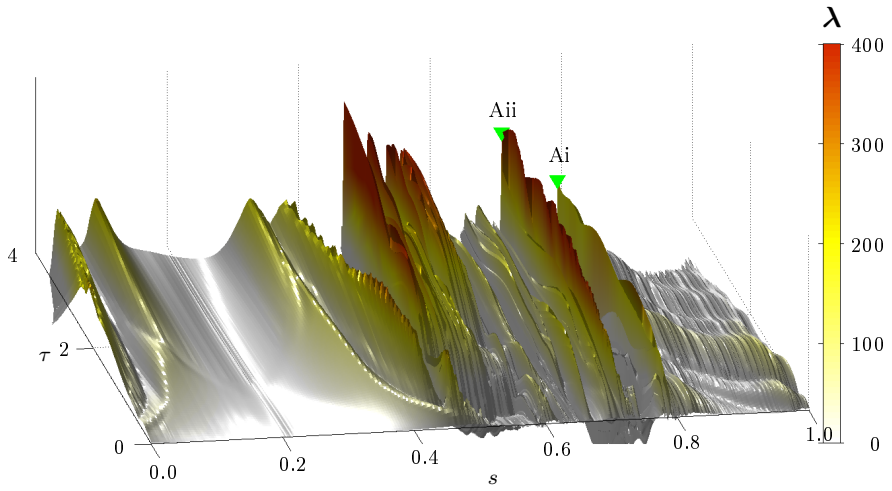

(a) Attracting LCS A

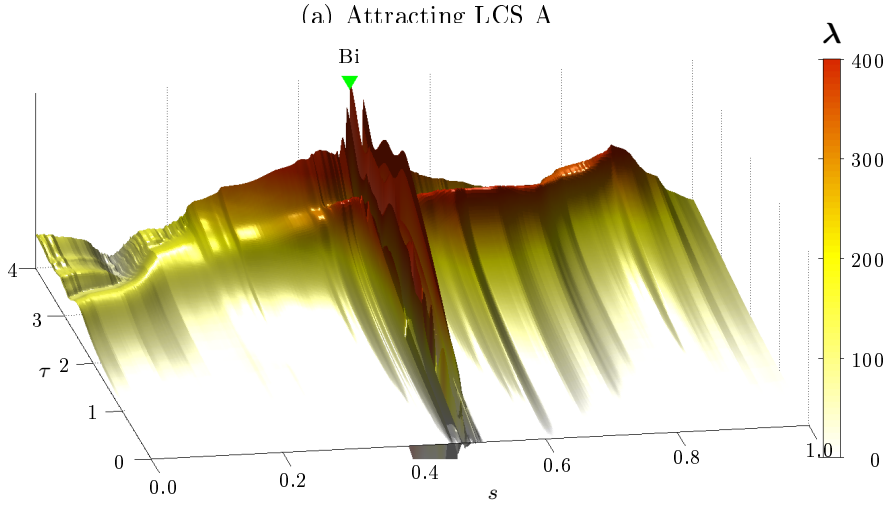

(b) Attracting LCS B

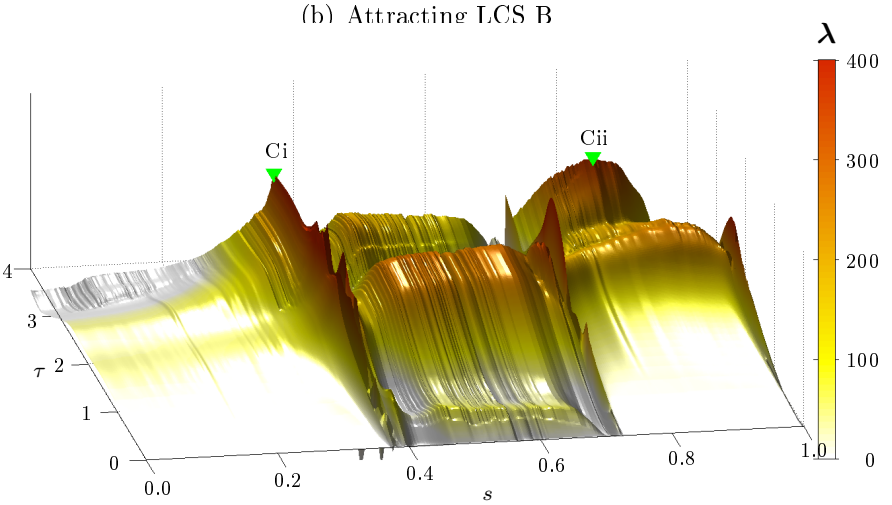

(c) Attracting LCS C

Figure 3-6: The corresponding λ values computed over attracting LCS A, B and C in figure 3-5 is 3D contour shown as a function of the curvilinear coordinate s (computed along the attracting LCS, and the integration time τ. The local maximum of λ at the end integration time τ is marked by green markers.

Lagrangian criteria	Integration direction	Integration interval ($\hat{T}$)
Negative-time FTLE	Backward	$t_0 + 2.0$
Positive-time FTLE	Forward	$t_0 - 4.0$
FTLE-saddle		t_0
Attracting LCS A	Backward	$3.7 - 1.7$
λ-saddle on attracting LCS A	Forward	$3.7 - 7.7$
Attracting LCS B&C	Backward	$7.7 - 3.7$
λ-saddle on attracting LCS B&C	Forward	$3.7 - 7.7$
LAVD	Backward	$17.0 - 13.0$
LAVD fluid particle	Backward	$17.0 - 3.7$

Table 3.1: Integration characteristics of various Lagrangian criteria

3.2.2 Vortex area for circulation calculation

As discussed in section 2.1.7, the definition of the vortex boundary and area remains ambiguous to date, especially during the vortex formation, but plays a critical role in the vortex circulation study. To determine the circulation of the LEV during its shedding process, vortex area for circulation calculation is defined by three approaches for comparison. Two approaches that involve instantaneous vortex identifications are introduced in this subsection. Traditionally, the instantaneous vortex circulation is obtained by integrating its vorticity within a rectangular or circular window generally surrounding the target vortex for easy implementation (Maxworthy, 1979; Anderson et al., 1998; Rival et al., 2010; Buchholz et al., 2011; Gutierrez et al., 2016), similar to the magenta square shown at three instants $\hat{T} = 4.0$, $\hat{T} = 8.0$ and $\hat{T} = 12.0$ in figure 3-8. The center of the window was determined by and follows the vortex center using the Γ_1 function (the orange spot shown in figure 3-8 in every instant).

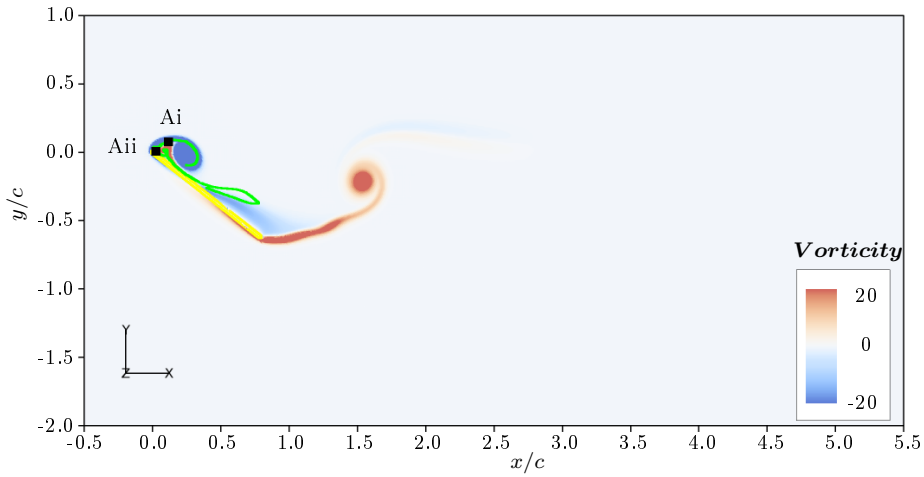

(a) $\hat{T} = 3.7$

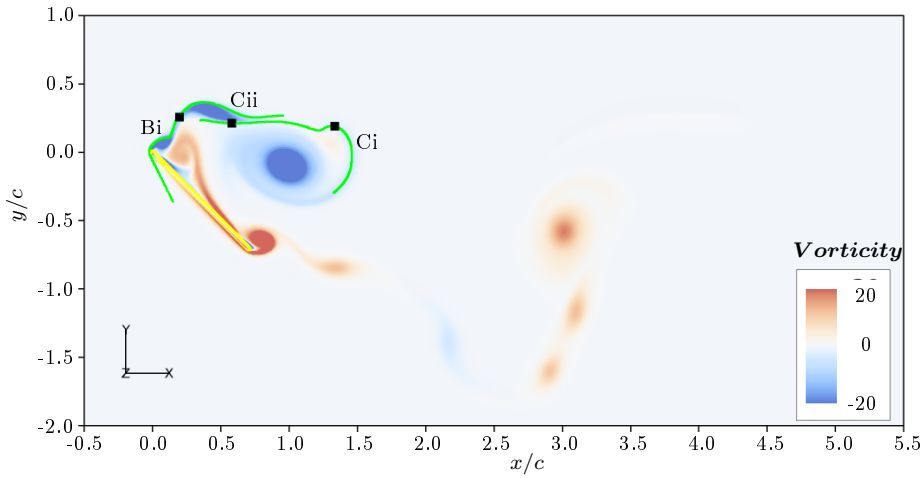

(b) $\hat{T} = 7.7$

Figure 3-7: Visualization of LEV shedding process by vorticity contour, attracting LCS (green lines) and λ-saddles (black spots) along them. λ-saddles A_i and A_{ii} are extracted from attracting LCS A at $\hat{T} = 3.7$, and λ-saddles B_i and C_i, C_{ii} are extracted from attracting LCS B and C at $\hat{T} = 7.7$ respectively. Flat plate is shown as yellow line.

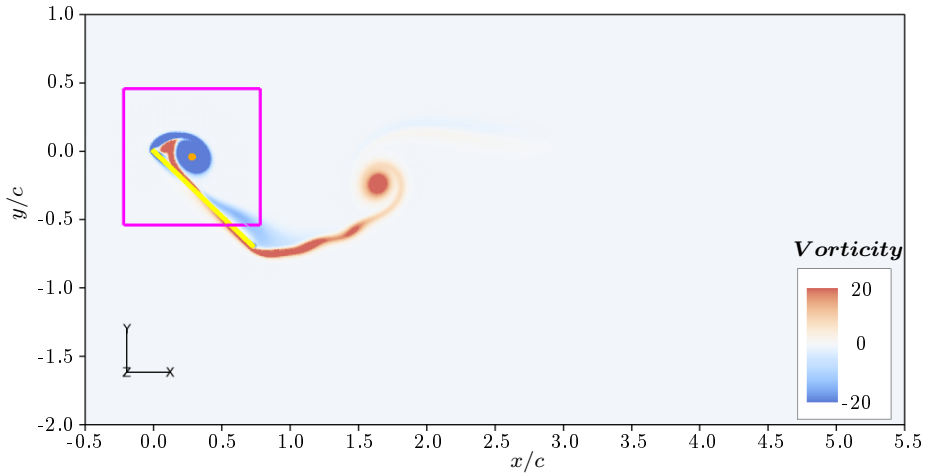

(a) $\hat{T} = 4.0$

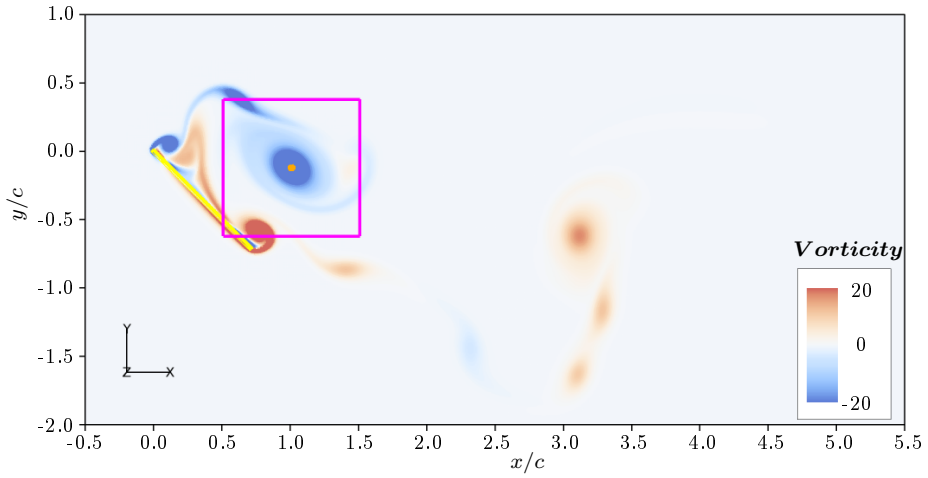

(b) $\hat{T} = 8.0$

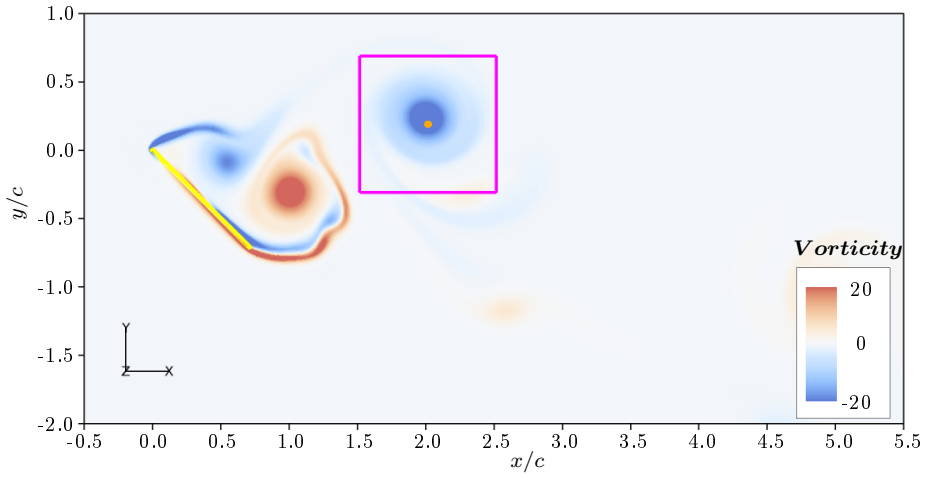

(c) $\hat{T} = 12.0$

Figure 3-8: Demonstration of window size/location for the LEV (magenta square) circulation calculation at three instants $\hat{T} = 4.0$, $\hat{T} = 8.0$ and $\hat{T} = 12.0$. The flow field is shown by vorticity contour, and the LEV center is shown by orange spot. The flat plate is shown as the yellow line.

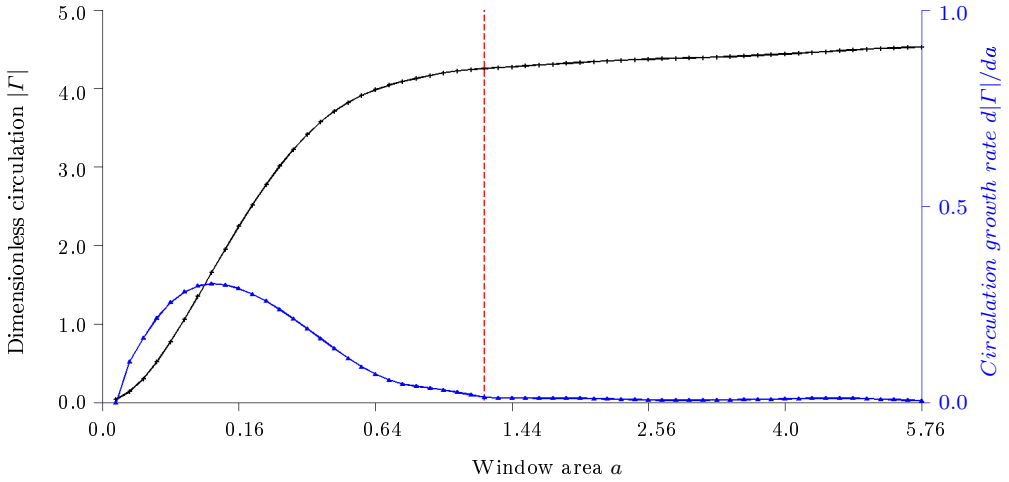

Figure 3-9: Circulation sensitivity analysis. The black line with black markers is the dimensionless circulation against the window area a. The blue line with blue markers is the circulation growth rate against the window area a. The red dash line marks the optimal window area for the LEV.

Early in the formation ($\hat{T} \leq 7.1$) of the the LEV, the positive Q-criterion iso-contour ($Q = 0$) does not distinguish the shear layer from the vortex core. The preferred window area, in cases where a forming vortex is fed by a connected shear layer, varies in the literature due to the influence of the shear layer and nearby vortices on the resulting circulation. Later, the LEV can be identified separately from the shear layer after it sheds at $\hat{T} \leq 7.1$, thus we pick the optimal window area at a later stage $\hat{T} = 12.0$ and apply it for the LEV circulation calculation at every instant.

A sensitivity analysis is conducted at $\hat{T} = 12.0$ to find the optimal dimensionless window area as indicated in figure 3-9. The dimensionless circulation and its growth rate against the dimensionless window area is shown as a function of the bounding window area around the LEV Γ_1 function center at $\hat{T} = 12.0$. For a window area of less than 1.25 (marked by red dash line), the circulation increases rather steeply. While for window area larger than 1.25, the dimensionless circulation $|\Gamma|$ reaches a plateau with a value 4.4, and the growth of dimensionless circulation with the increasing dimensionless window area reaches to a plateau with a value 0.01. Therefore, a bounding window of area 1.25 is chosen as the optimal window for the LEV circulation calculation through the LEV

formation and shedding process. Only the negative vorticity within the optimal bounding window is included in the spatial integration of equation 2.16. During the formation stage, the variation of LEV circulation calculated within the fixed-area window represent the transportation of vorticity flux by shear layer into the LEV.

For the study of formation number in the current case, the total circulation over the whole plate also needs to be calculated. The total circulation is obtained by the spatial integration of all the negative vorticity in the whole flow domain.

Another approach was developed uniquely in this thesis to obtain a more specific prescription of the individual LEV structure. In this approach, the LEV is identified by the selected regions within a $Q = 0$ level set centered on each Γ_1 function-identified LEV center (as shown in figure 3-10). The forming LEV is made of the main core region and shed feeding shear layer region, for example the two light green positive Q blocks in the instantvisualized in the figure 3-10. The regions within the $Q = 0$ level set above the main LEV core (region surrounding orange LEV center) are shed from the feeding shear layer and will be entrained later into the LEV core. It is included in the vortex area, because it locates inside the LEV boundaries of both pFTLE and nFTLE ridges, which means it will entrain into LEV in the future. The vortex area identified by this approach is re-initialized for each velocity field snapshot. This method will introduce error by mistakingly including extra regions of vorticity or shear layer in the vicinity of the targeted vortex, and will make it difficult for automatic calculation due to the changing LEV area each time step.

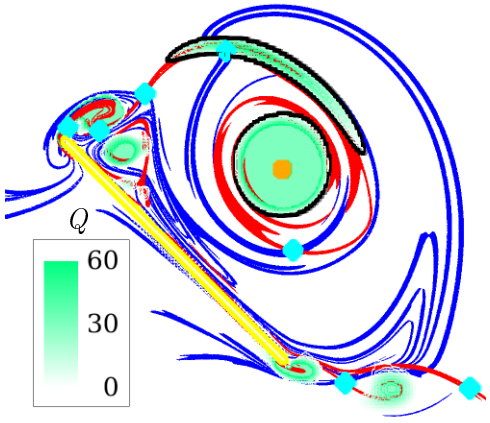

Figure 3-10: Vortex area identified by multiple criteria. Negative- and positive-time FTLE ridges are contoured as red and blue ridges respectively, with contour level of values more than 85% maximum. Positive Q-criterion (black) with contour level $Q = 0$. Flat plate is shown as yellow line. Green curves bound the vortex area of primary LEV to be used in circulation calculation.

3.2.3 Identification method by LAVD

LAVD is implemented to identify the materially-coherent LEV during a time frame after it has shed. The area is determined after it is shed due to the tubular requirement for an LAVD vortex. The filamentary shape of vortex undergoing formation would make it fail the convexity deficiency threshold, and dissatisfy the definition of tubular shape LAVD vortex. The forming LEV usually is not materially-coherent, because the entrainment and detrainment of the mass transformed from the shear layer. By comparing the detection of LEV by both LAVD and Q-criterion, certain feeding shear layer regions, picked up by Q-criterion as part of the LEV, are eventually excluded from the materially-coherent LEV identified by LAVD.

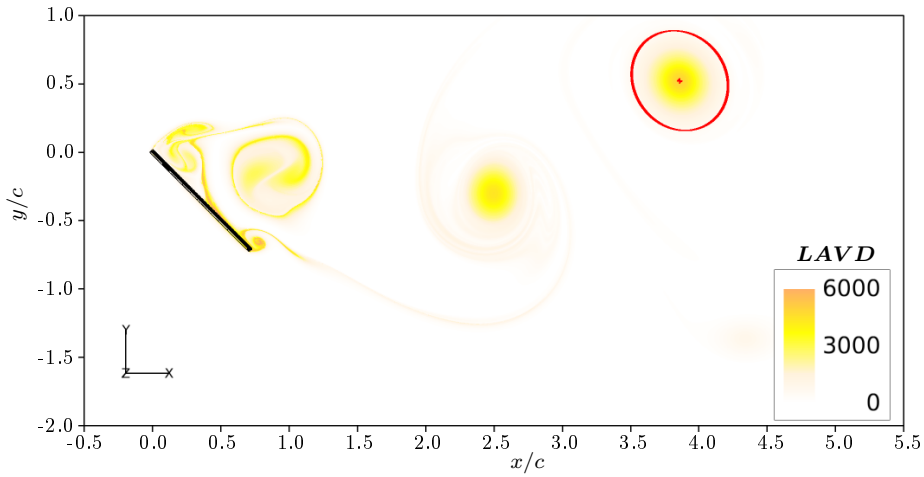

(a) $\hat{T} = 17.0$ LEV

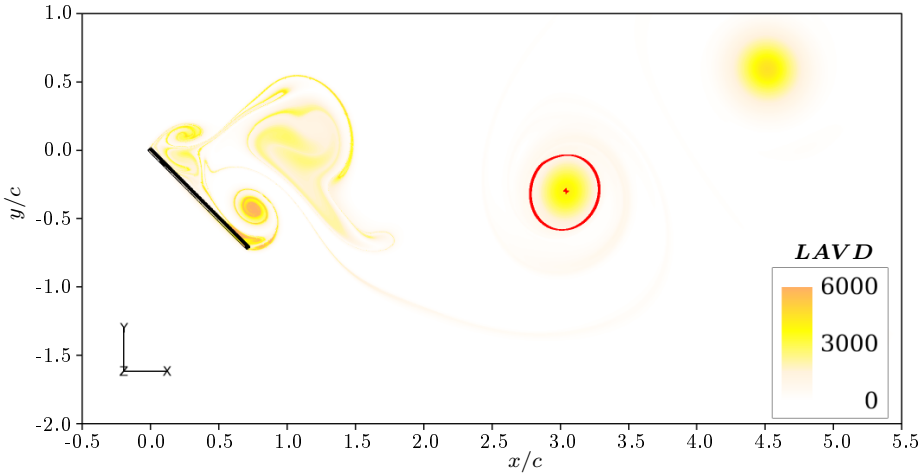

(b) $\hat{T} = 18.8$ TEV

Figure 3-11: Identification of the LEV and the TEV after shedding by contour plot of LAVD at $\hat{T} = 17.0$ and $\hat{T} = 18.8$, respectively. LAVD vortex center and boundary are shown as red spot and circle respectively. Flat plate is shown as black line.

In the case of the LEV on a pitching flat plate, the LAVD of the primary LEV is calculated at $\hat{T} = 17.0$ after it is fully shed. A TEV formed and shed in the vicinity of the primary LEV is also studied by LAVD at a time $\hat{T} = 18.8$ to reveal the interaction between the LEV and the TEV by the motion of the fluid particles from the shear layer. The LAVD contour plot, LAVD center and boundary of both LEV and TEV are shown in figure 3-11. The LAVD calculation for the LEV is done backward during formation time span $\hat{T} = 17.0 - 13.0$, and similarly a backward calculation during $\hat{T} = 18.8 - 14.8$

is used to determined the TEV area.

The third approach we exploit to provide a new way of studying the vortex area for its circulation calculation is with the objective LAVD. Figure 3-12 shows that all the fluid within the LAVD boundary constitutes a Lagrangian coherent vortex during calculation time span $\hat{T} = 17.0 - 13.0$, but it can also be tracked backward by a flowmap calculation to time before $\hat{T} = 13.0$. In this way, its origins (shear layer over pitching panel and from upstream) before being entrained into the coherent LEV are shown, such as at the instant of $\hat{T} = 6.4$ in figure 3-12(c). Despite not being considered a 'coherent vortex' for $\hat{T} < 13.0$, the fluid defined this way stays materially invariant at these earlier times. It enables us to study the relationship between shear layer and the LEV and the feeding process between them, as well as the strength an LEV requires to shed. A better understanding of how fluid mixes during vortex shedding presents the opportunity to identify when the fluid making up the vortex will be subject to a flow control scheme designed to influence the vortex dynamics (Cardwell and Mohseni, 2008).

The circulation within the LAVD boundary for each velocity field is calculated on same set of fluid particles in their new location, which will remain a constant area due to incompressibility, to monitor the LEV formation and shedding. The LEV vortex center defined by LAVD at $\hat{T} = 17.0$ is convected backward by flow map for each instant as well.

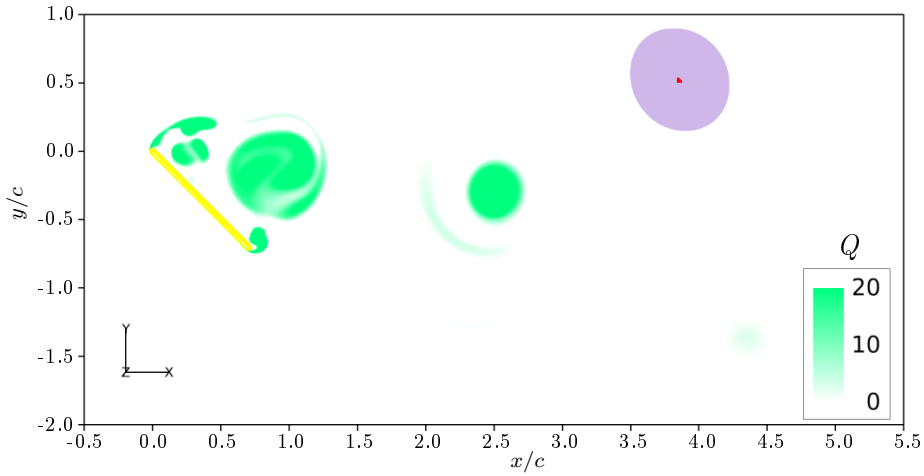

(a) $\hat{T} = 17.0$

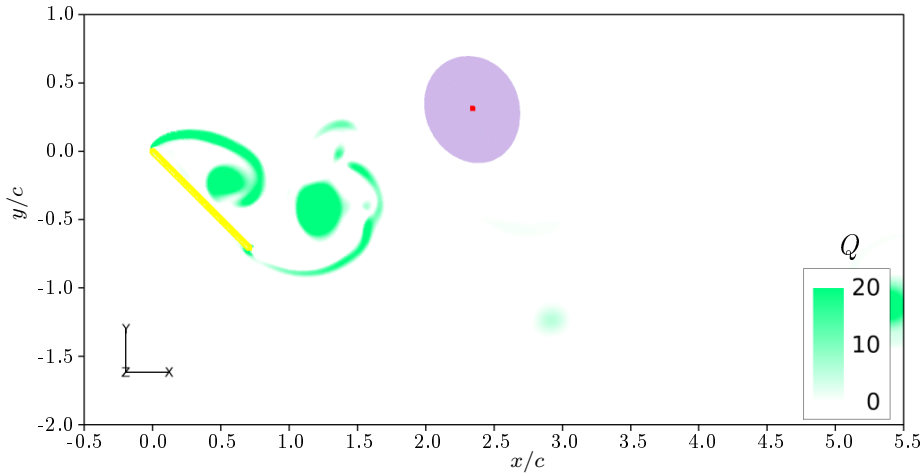

(b) $\hat{T} = 13.0$

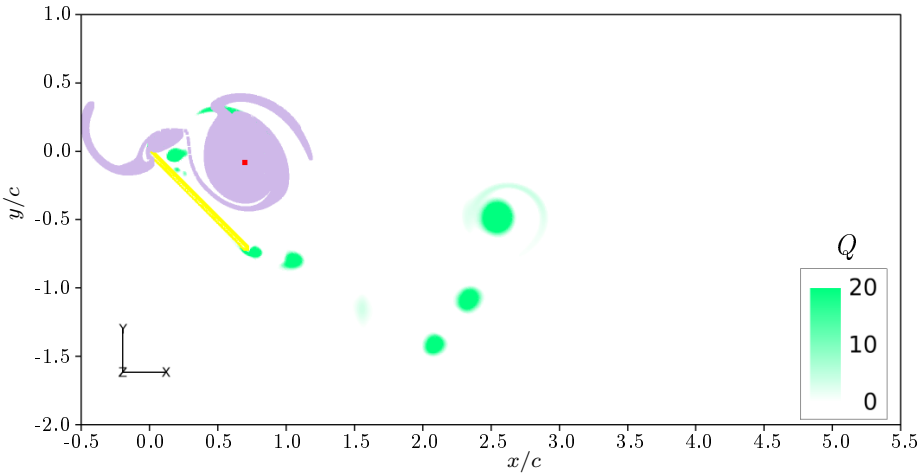

(c) $\hat{T} = 6.4$

Figure 3-12: Distribution of Lagrangian fluid belonging to primary LEV at different instants. Purple regions are fluid within Lagrangian coherent structure of primary LEV identified by LAVD. Flow field is shown by positive Q contour, and the LEV center by LAVD is shown as red spot. Flat plate is shown as yellow line.

3.3 Results

3.3.1 FTLE- and λ-saddles

Figure 3-13 shows the formation time history of the primary LEV separation process at nine instants of the flow evolution. In the figures, multiple vortex identification techniques are employed. Red and blue ridges are the negative- and positive-time FTLE ridges, respectively. Green contour regions indicate the vortex core by positive Q-criterion. The orange and black spots mark the Γ_1-criterion and Q-criterion vortex centers of the primary LEV and a TEV formed in its vicinity. The cyan spots with the black edge visualize the FTLE-saddles of the LEV and TEV via the methods described in section 3.2.1. In figure 3-13(a) when $\hat{T} = 3.7$, the LEV has started rolling up from the shear layer into the circulating area, and multiple vortices have shed from the trailing edge. Both the Γ_1 function and Q-criterion locate the vortex centers in approximately the same location for each LEV vortex core. As described, the FTLE-saddles locate at the intersections of the pFTLE and nFTLE ridges. Four of the FTLE-saddles between the LEV and shear layer or TEV, containing the most information of the relevant dynamics, are marked 'I', 'II', 'III' and 'IV' corresponding to the time of their appearance.

After formation until $\hat{T} = 4.5$ (3-13(b)), the LEV centers by both methods continue to move downstream, from approximately $x/c = 0.25$ to $x/c = 0.45$, but the LEV FTLE-saddle I stays in approximately the same position ($[x/c, y/c] = [0.11, 0.07]$). This location is not exactly at the leading edge of the plate, but remains toward the top of a pair of counter-rotating secondary and tertiary vortices that form at the leading edge after the formation of the primary LEV. That FTLE-saddle I is stationary and connected to the vortex system during this time indicates continued LEV attachment. After $\hat{T} = 4.5$, FTLE-saddle I accelerates downstream, and the centers of the LEV continue to move downstream at a steady rate.

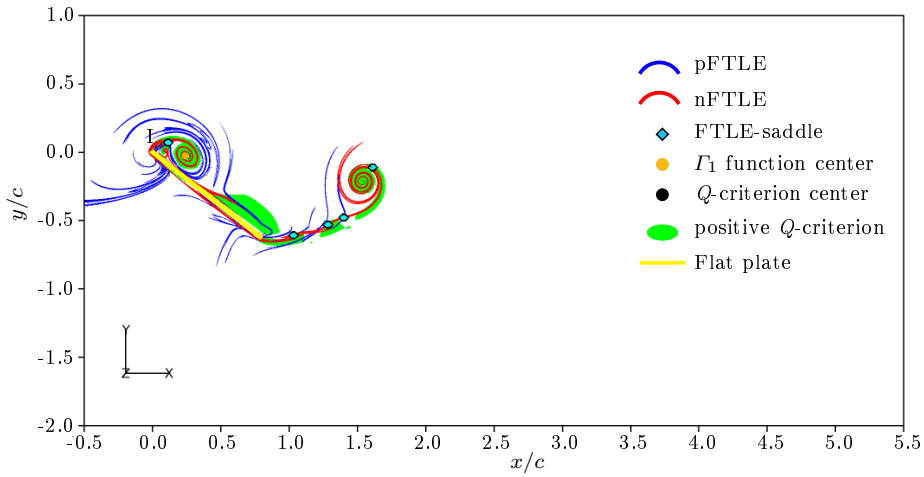

(a) $\hat{T} = 3.7$

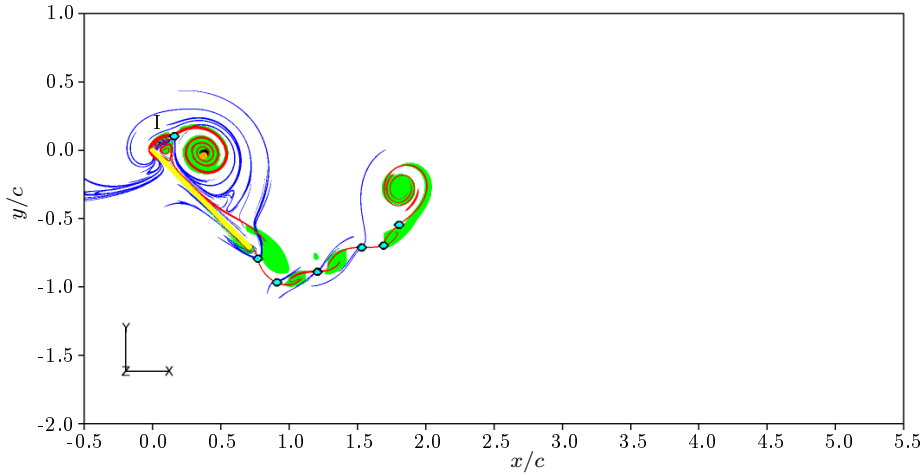

(b) $\hat{T} = 4.5$

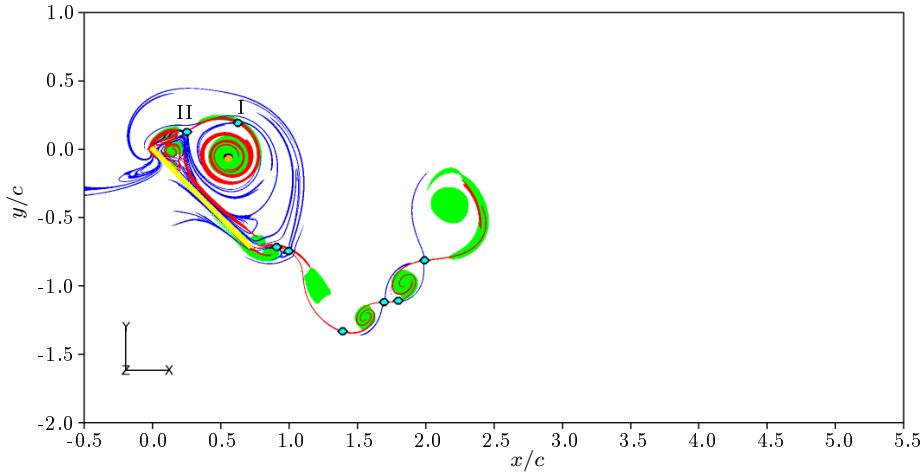

(c) $\hat{T} = 5.5$

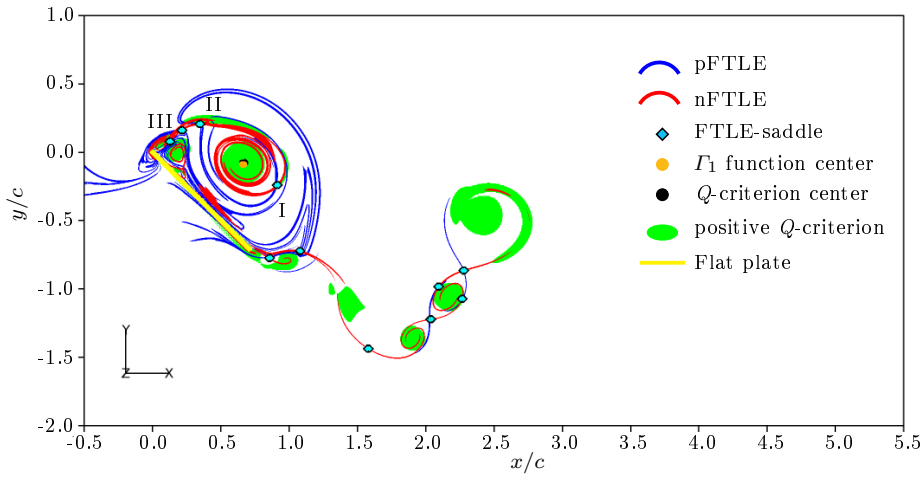

(d) $\hat{T} = 6.1$

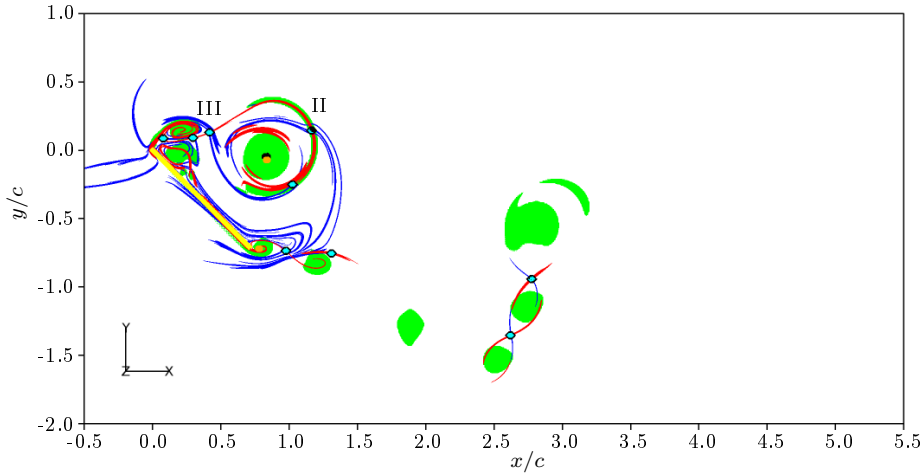

(e) $\hat{T} = 7.1$

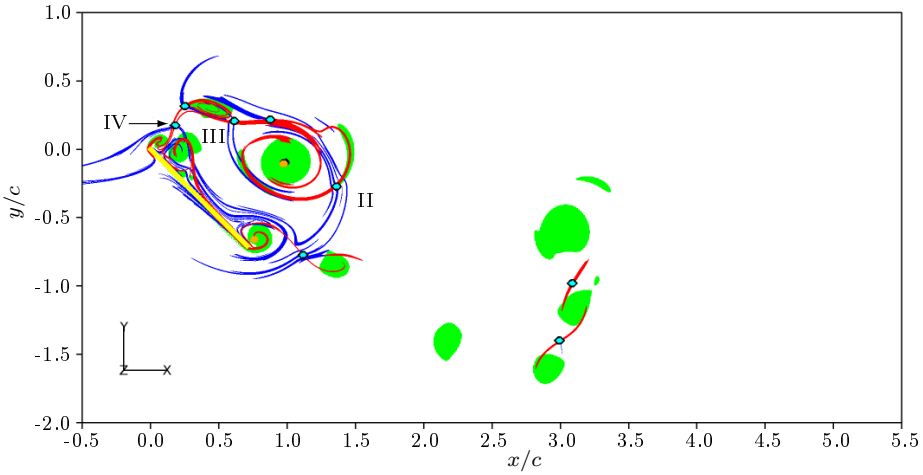

(f) $\hat{T} = 7.7$

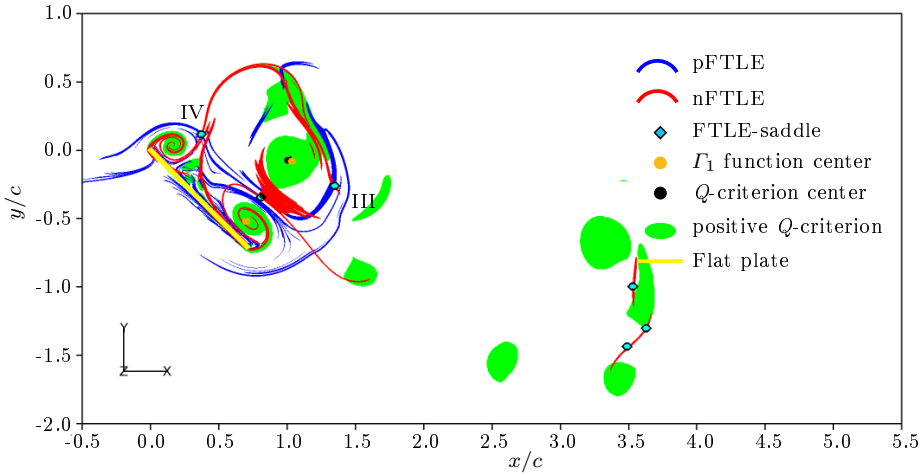

(g) $\hat{T} = 8.5$

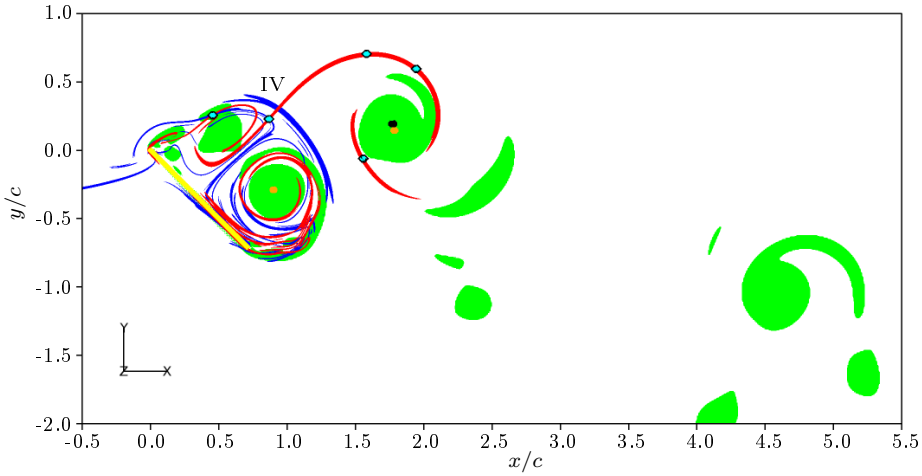

(h) $\hat{T} = 11.3$

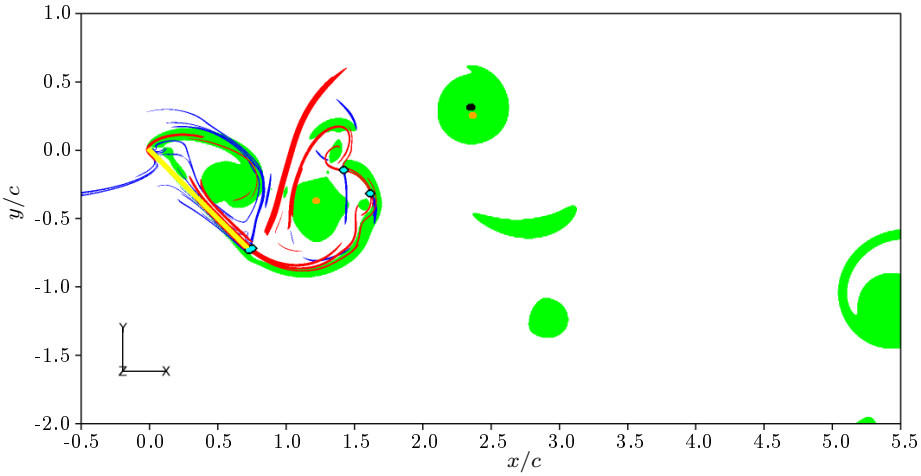

(i) $\hat{T} = 13.0$

Figure 3-13: Instantaneous flow field is shown by positive Q-criterion. nFTLE and pFTLE are contoured as red and blue ridges respectively, with contour level of values more than 85% maximum. Γ_1 function, Q-criterion centers and FTLE-saddles are presented by orange, black spots and cyan spots with black edge, respectively. Flat plate is shown as yellow line.

The TEV center is detected by Γ_1 function at $\hat{T} = 6.9$ (the instant before figure 3-13(e)) when its circulation motion is intense enough. It convects upstream along the pitching plate between the LEV and the plate between $\hat{T} = 7.1$ (figure 3-13(e)) and $\hat{T} = 10.0$. The FTLE-saddle IV appears at $\hat{T} = 7.6$ between the LEV, TEV and the secondary LEV, and convects downstream with a similar speed of the LEV center until $\hat{T} = 11.3$. At $\hat{T} = 11.3$, FTLE-saddle IV drops toward the pitching plate between the TEV and the secondary LEV, and the center of the TEV starts convecting downstream with an accelerating speed.

Figure 3-14 shows the location of each of these tracking targets in time, measured as distance from the leading edge and scaled by the plate chord. From this figure, we see that LEV Q-criterion center and Γ_1 function center give very similar traces of the vortex center path, with a convecting speed $u_{convec} \approxeq 0.7U_\infty$, matching the convection speed range between 0.6 and 0.8 of shed vortices from the airfoils as reported by Panda and Zaman (1994).

The traces of the FTLE-saddles, on the other hand, appear to move with a different profile. As can be observed in a movie of the tracking targets' motion, this is due to the rotation of the structure boundary after it sheds and begins to evolve downstream (figure 3-13(b) – figure 3-13(i)). Each point on the LEV boundary (including the FTLE-saddles) will trace out a large arc unlike the vortex core path. A portion of the difference comes from the fact that as a structure grows, the core points shift downstream even as the LEV remains attached to the plate (figure 3-13(a) – figure 3-13(b)).

The motion difference between different targets is evident in figure 3-14 in the trace of FTLE-saddle I, which is part of the boundary of the primary LEV that forms and sheds first. FTLE-saddle I moves away from its initial stationary location with a rapid acceleration at $\hat{T} = 4.5$ (figure 3-13(b)). This is apparent in the changing slopes of the cyan diamonds in figure 3-14, which is highlighted with two intersecting red solid lines and by dash lines 'a'. After it sheds, FTLE-saddle I follows an arc due to its motion around the LEV as shown between $\hat{T} = 4.5$ in figure 3-13(b) and $\hat{T} = 6.1$ in figure 3-13(d). We propose that this rapid acceleration of Lagrangian saddles from their formation zone gives a good indication of the starting point of vortex shedding. Similar to the cyan trace

of FTLE-saddle I, the other two traces of FTLE-saddle II (green) and FTLE-saddle III (blue) indicate additional dynamics of the LEV shedding process.

As postulated in section 1.1.2, the LEV separation can be described as a process in which the leading edge shear layer stops feeding circulation to the LEV, and the LEV does not shed from the shear layer until it reaches its maximum circulation. In the present case, however, this process is intermittent. The shear layer emanating from the leading edge breaks into masses of vorticity due to the Kelvin Helmholtz-type instability (DeVoria and Ringuette, 2012).

By observing the shear layer in figure 3-13(b) as the thin green region of $Q > 0$ extending from the leading edge of the plate to the LEV, we see that the Q-criterion magnitude in the shear layer near FTLE-saddle I drops considerably at $\hat{T} = 4.5$ as FTLE-saddle I sheds. In figure 3-13(c), the value of Q-criterion in the region of interruption has become negative, indicating that that region is no longer considered part of a vortex according to the Q-criterion.

However, an additional green filamentary region of shear layer is wrapped around and then entrained into the LEV after that, before breaking again at $\hat{T} = 6.1$, as seen in figure 3-13(d). The timing of this second interruption corresponds to the acceleration of FTLE-saddle II at $\hat{T} = 6.1$, as highlighted by dash lines 'b' in figure 3-14. Finally, an additional region of vorticity is shed and entrained into the LEV at approximately $\hat{T} = 7.1$ (as shown in figure 3-13(e)), which corresponds to FTLE-saddle III shedding at that time (as highlighted by dash lines 'c' in figure 3-14). This is the last saddle to move from the leading edge region and wrap around the LEV, and after its departure a drastically different Lagrangian coherent structures emerge, as shown between figure 3-13(f) and figure 3-13(i).

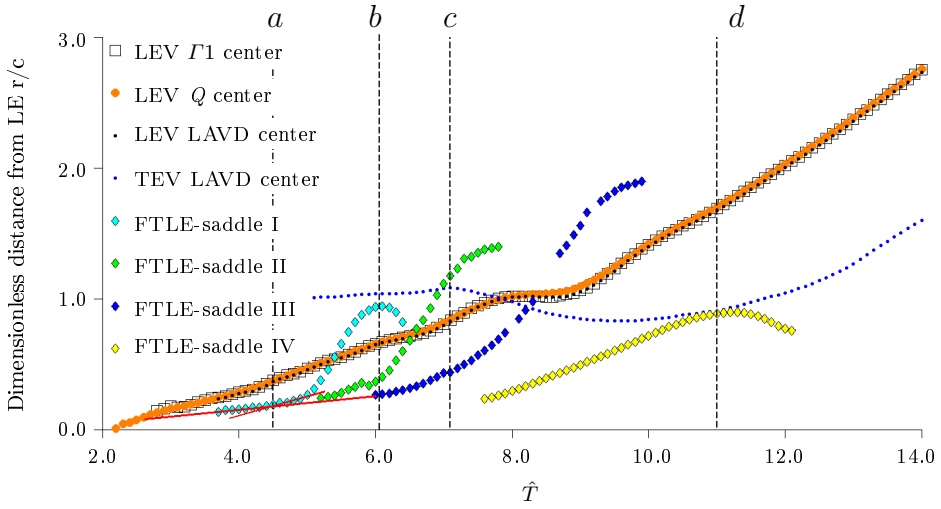

Figure 3-14: Distance of tracking markers, measured from the panel leading edge, in formation time. Red lines indicates the trace segments slopes of FTLE-saddle I. Black dash lines indicate FTLE-saddle shedding times.

The trace of the TEV center indicates its motion upstream starting at $\hat{T} = 7.1$, when the last detected FTLE-saddle of the LEV, FTLE-saddle III, sheds. This phenomenon matches the observation in the research of Rival et al. (2014), which points out that the LEV shedding leads to the opening of a channel for reversed flow, the development of TEV, at the trailing edge. In the research by the Eulerian topological analysis (Rival et al., 2014), the LEV shedding process is described as the merging of the rear stagnation point (half Eulerian saddle) of the LEV and half Eulerian saddle of the trailing edge into one full Eulerian saddle, and the lift-off of this full Eulerian saddle. In this thesis, the observed LEV shedding process shows a similar influence on the topology at the trailing edge, while taking advantage of the frame invariant Lagrangian approaches.

The FTLE-saddle IV (yellow) trace exhibits a constant distance from the LEV center between $\hat{T} = 7.7$ and $\hat{T} = 11.3$, while a growth in distance is observed between the TEV and the secondary LEV (as shown in figure 3-13(f) – figure 3-13(h)). The FTLE-saddle IV sheds at $\hat{T} = 11.3$ as highlighted by dash lines 'd' in figure 3-14), dropping towards the plate between the TEV and the secondary LEV (figure 3-13(h)). At the same time, a slope change of the TEV center trace by both LAVD and Γ_1 function indicates the beginning of its convection downstream.

Figures 3-15 and 3-16 compare the performance of the λ-saddles of three attracting LCSs and five FTLE-saddles (introduced in section 3.2.1) in detecting the LEV shedding process at five instants. As seen in figure 3-15(a), λ-saddle Ai is found in the vicinity of FTLE-saddle I at the attracting LCS A extracting time $\hat{T} = 3.7$. We consider FTLE-saddle I and λ-saddle Ai to be the two different numerical saddles identifying the same physical saddle in the flow at the moment. Ideally, we expect both the FTLE-saddles and the λ-saddles to behave similarly.

However, in a movie that compares the motion of both the FTLE-saddle and the λ-saddle, the λ-saddle Ai only remains close to the FTLE-saddle I for a finite interval after the latter is detected (as shown in figure 3-15(a)). After the previous stage, it shows that the λ-saddle Ai tends to convect away from the FTLE-saddle along the attracting LCS A earlier and gets entrained inside the LEV, as observed in figure 3-15(b) and figure 3-15(c). The λ-saddle Aii is observed in figure 3-15(c) in the vicinity of FTLE-saddle III right after the latter is detected at the time $\hat{T} = 6.0$. Similarly, a finite interval after $\hat{T} = 6.1$, the λ-saddle Aii convects away from the FTLE-saddle along the attracting LCS A and gets entrained inside the LEV earlier (shown between figure 3-15(c) and 3-15(e)).

In figure 3-16(e), λ-saddles Bi and Cii appear in the vicinity of FTLE-saddles III and IV at the time $\hat{T} = 7.7$ when the attracting LCS B and C are extracted. Contrasted with λ-saddle Ai, λ-saddles Bi and Cii appear to convect towards the vicinity of FTLE-saddles III and IV from the upstream along the attracting LCS B and C. Later, λ-saddles Bi and Cii convect close to the FTLE-saddles along the attracting LCS B and C. Between the figure 3-16(c) and 3-16(e), the λ-saddle Ci convects at close to, but upstream of FTLE-saddle II along the attracting LCS C, with a constant distance between them.

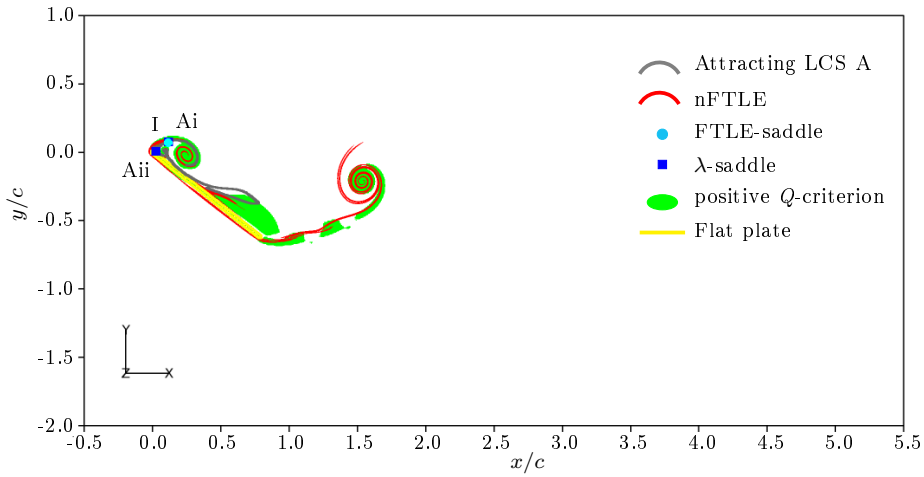

(a) $\hat{T} = 3.7$

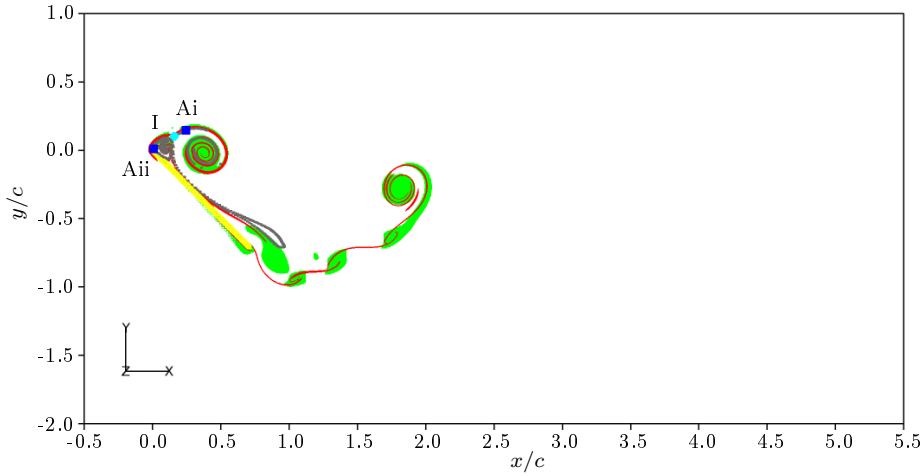

(b) $\hat{T} = 4.5$

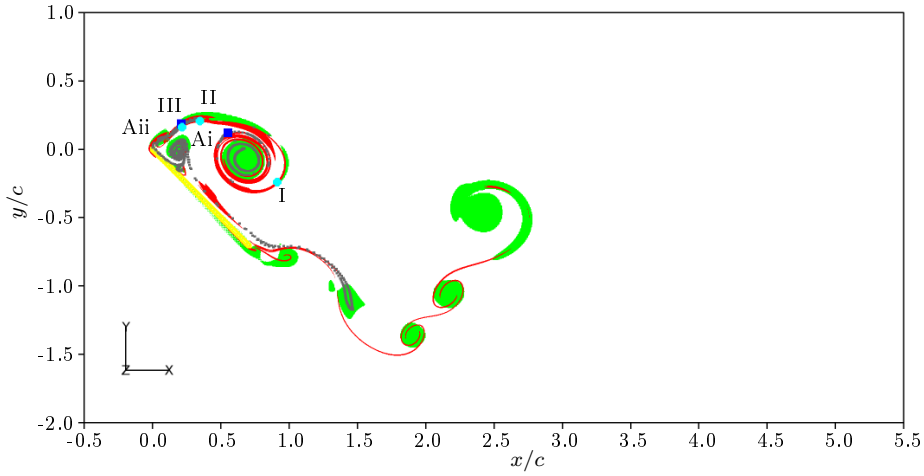

(c) $\hat{T} = 6.1$

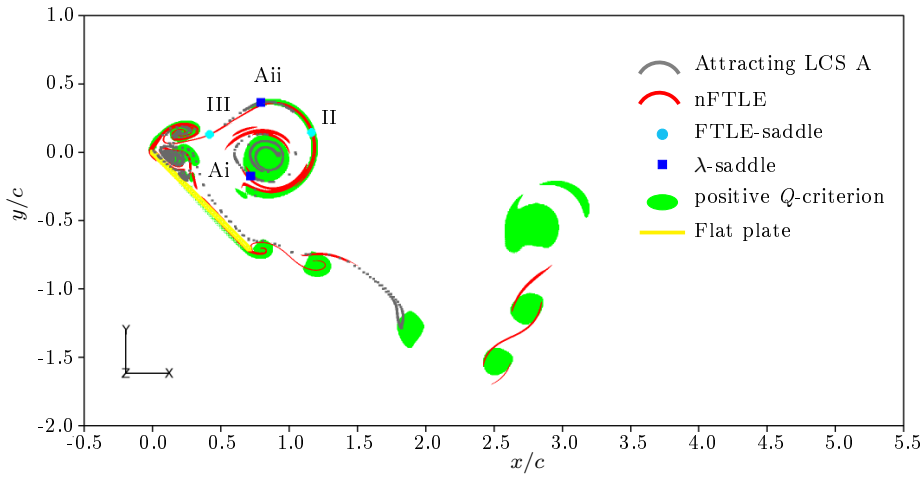

(d) $\hat{T} = 7.1$

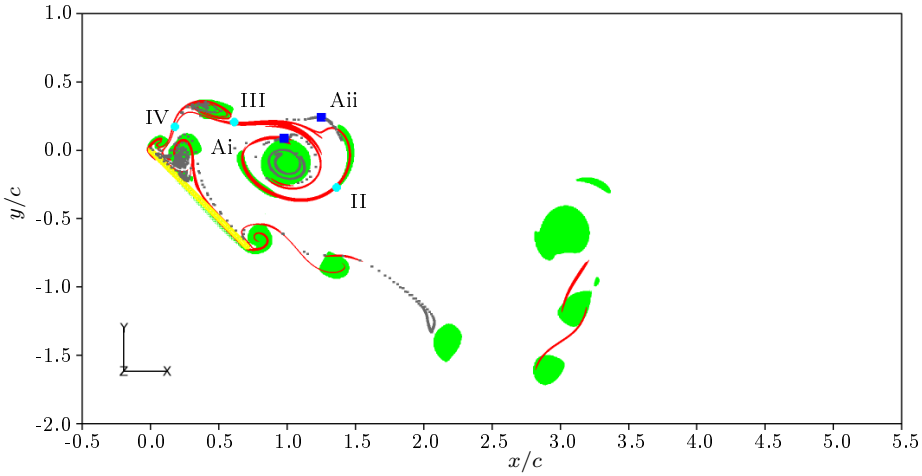

(e) $\hat{T} = 7.7$

Figure 3-15: Comparison of FTLE-saddles and λ-saddles on attracting LCS A (gray curves) during the LEV shedding process. Vortex core areas are visualized by green positive Q-criterion, and nFTLE are contoured as red ridges indicating the vortex area, with contour level of values more than 85% maximum. The λ-saddles on A and FTLE saddles are shown as blue and cyan spots. Flat plate is shown as a yellow line.

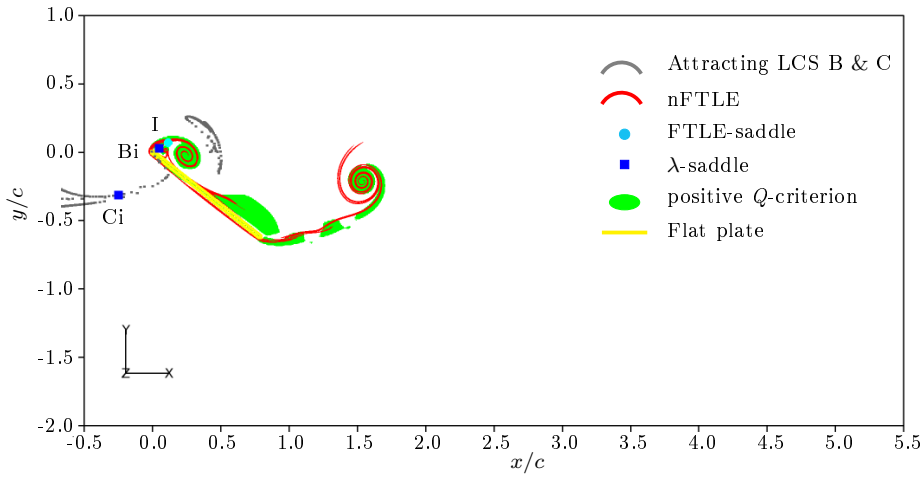

(a) $\hat{T} = 3.7$

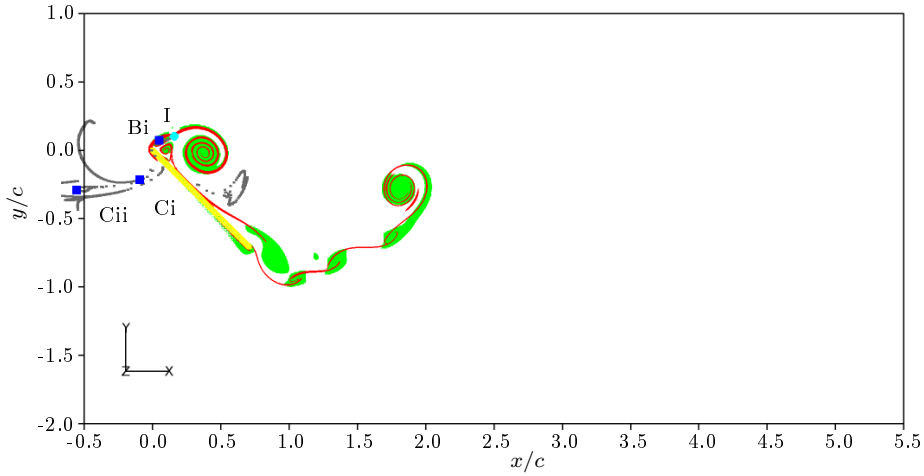

(b) $\hat{T} = 4.5$

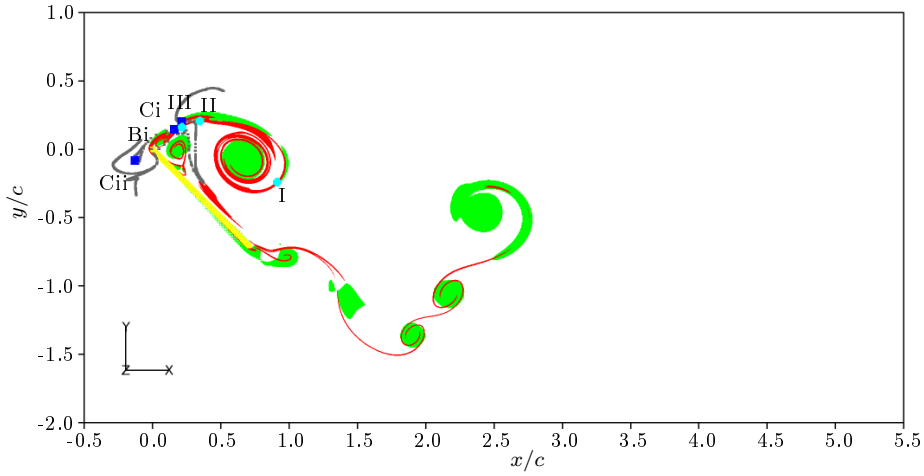

(c) $\hat{T} = 6.1$

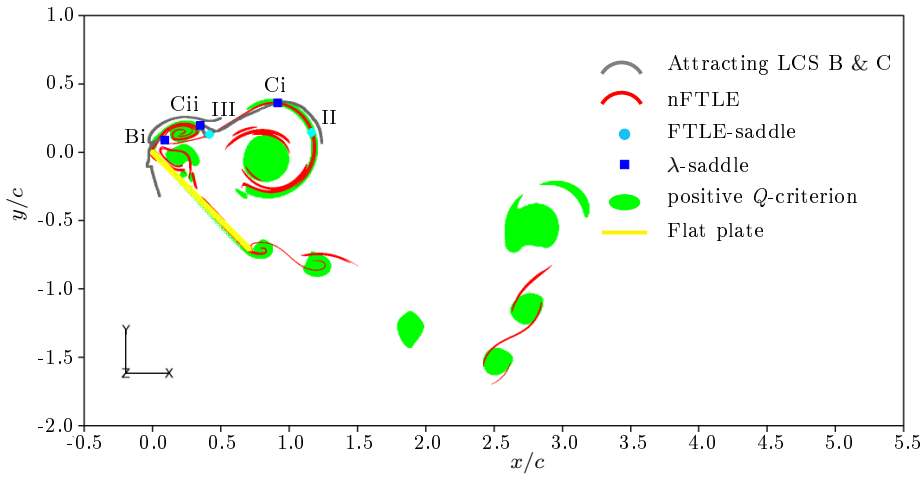

(d) $\hat{T} = 7.1$

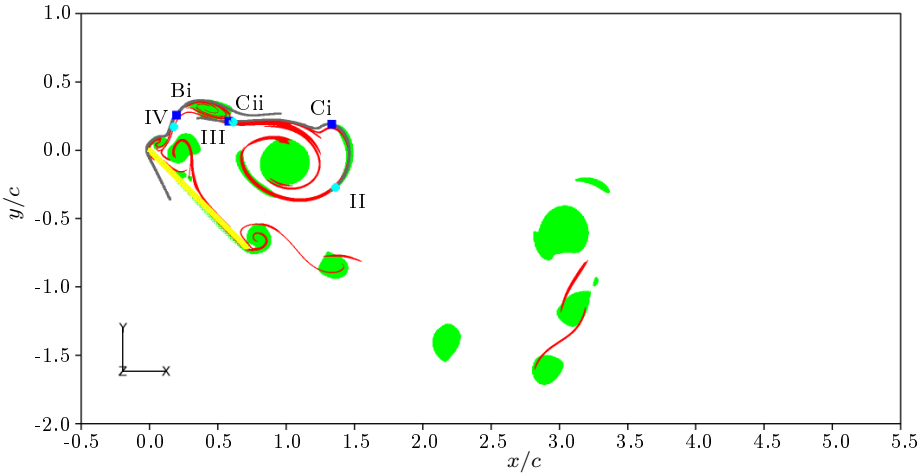

(e) $\hat{T} = 7.7$

Figure 3-16: Comparison of FTLE-saddles and λ-saddles on attracting LCSs B & C (gray curves) during LEV shedding process. Vortex core areas are visualized by green positive Q-criterion, and nFTLE are contoured as red ridges indicating the vortex area, with contour level of values more than 85% maximum. The λ-saddles and FTLE saddles are shown as blue and cyan spots. Flat plate is shown as a yellow line.

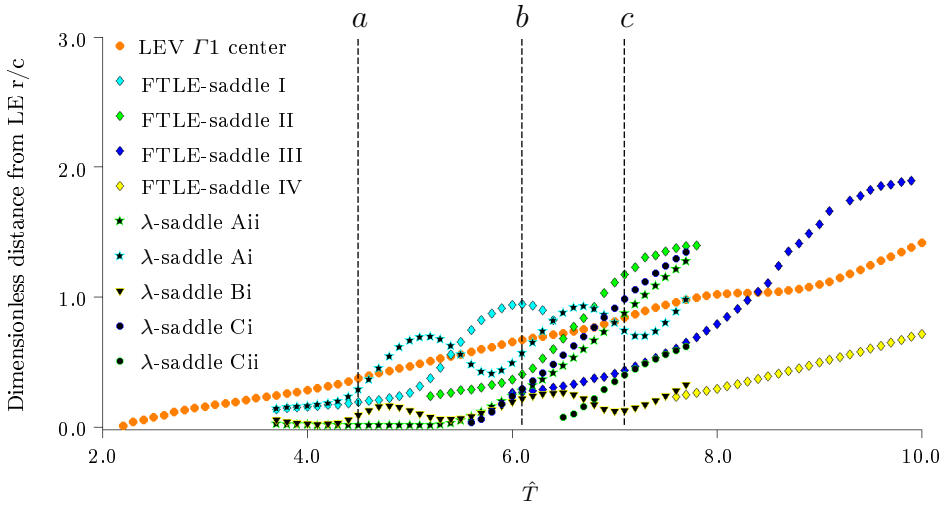

Figure 3-17: Comparison of FTLE-saddle and λ-saddle traces in formation time.

Figure 3-17 shows the location of each of these Lagrangian saddles and the LEV center identified from the Γ_1 function, measured as distance from the leading edge, scaled by the plate chord, and shown as a function of the formation time. The λ-saddle Ci have parallel trace with FTLE-saddle II after the latter sheds at $\hat{T} = 6.1$. The λ-saddle Ai trace overlaps with FTLE-saddle I during $\hat{T} = 3.7$ and $\hat{T} = 4.2$, then sheds and entrains into the LEV, as shown by its spiraling shape around the LEV center trace. The λ-saddle Aii trace overlaps with FTLE-saddle I during $\hat{T} = 6.0$ and $\hat{T} = 6.1$, then changes slope earlier and becomes parallel to the trace of the latter after the latter's shedding time $\hat{T} = 7.1$. The λ-saddle Bi and Cii traces show a deceleration trend and start overlapping with FTLE-saddle IV and III traces, respectively.

We can see the λ-saddles are showing similar dynamics with FTLE-saddles but with some discrepancy at shedding time. We argue that applying the flow map on discrete data as in the algorithm of the λ-saddle extraction can possibly be introducing numerical errors, as the saddles can shoot out earlier along the attracting LCS, if there is an initial discrepancy between the physical saddle and the numerical saddle.

Similarly, there an initial discrepancy between the physical saddle and the FTLE-saddle. While the standard method used to extract the FTLE-saddle constrains the discrepancy between the FTLE-saddle and the physical saddle to the FTLE calculation grid size for every instant (shown in figure 3-18).

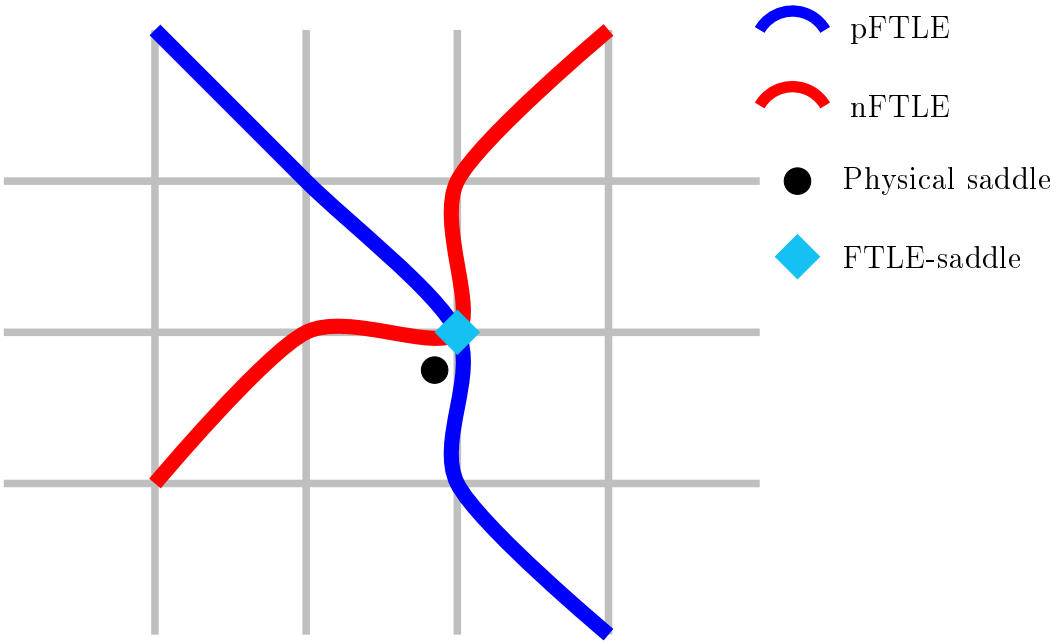

Figure 3-18: Discrepancy between physical saddle and FTLE-saddle.

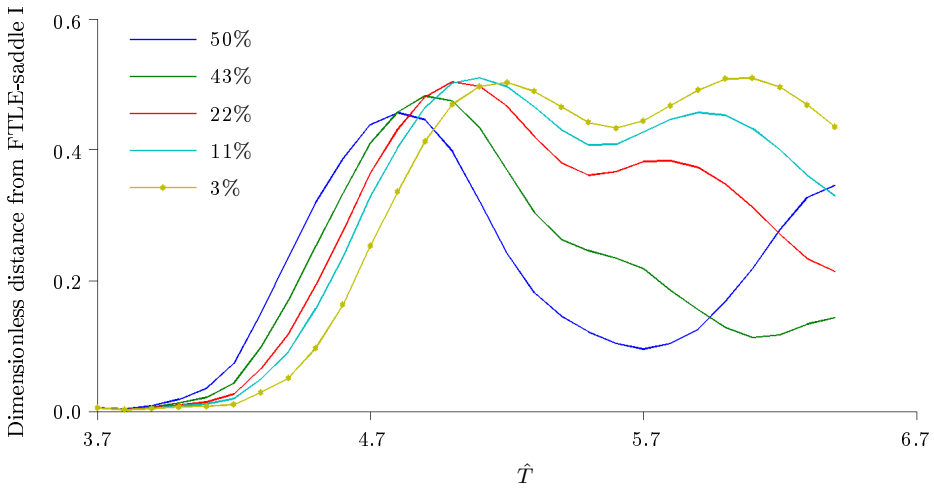

Figure 3-19: Distance between FTLE-saddle I and λ-saddles along attracting LCS A with different initial resolutions. The mustard yellow line with hexagram markers represents the distance between the λ-saddle Ai and the FTLE-saddleI.

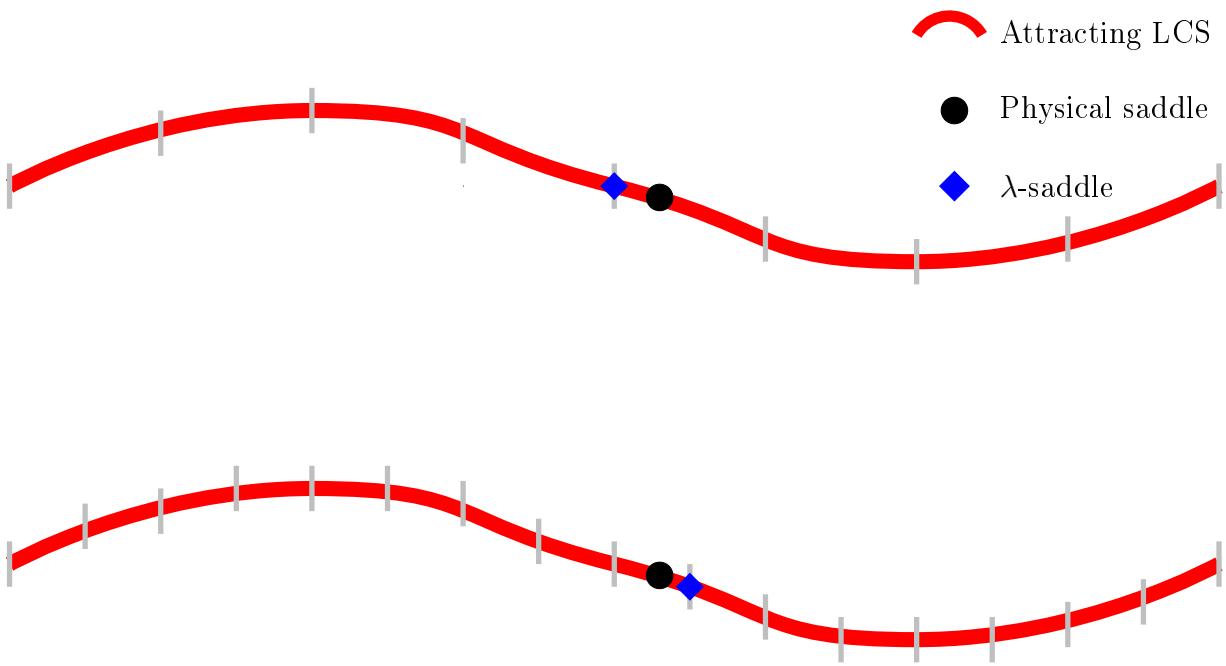

Figure 3-20: Schematic of flow maps.

On the other hand, besides the initial discrepancy in the extraction of the attracting LCS (up to the LCS grid size), there is another source of numerical error coming from the λ-saddle convection by the flow map in the λ-saddle extraction algorithm.

To illustrate this point, we picked five different initial grid sizes ($3\%, 11\%, 22\%, 43\%$ and 50% of the FTLE calculation grid size) for the attracting LCS A and extracted the λ-saddle in the vicinity of FTLE-saddle I. The distance between the five λ-saddles and FTLE-saddle I are plotted in figure 3-19 as a function of formation time. As we can see in figure 3-19, all the λ-saddles are extracted and convecting in the close vicinity of the FTLE-saddle I from $\hat{T} = 3.7$ to $\hat{T} = 3.9$, then the distance between them and the FTLE-saddle I increases with the formation time increasing. As shown in figure 3-20, if we ignore the numerical error of the LCS grid size and assume the physical saddle is located on the LCS, the finer initial grid size of LCS can identify the λ-saddle closer to the physical saddle. It is also shown that the fine initial grid size along the attracting LCS A will delay the shooting out of the λ-saddle, that the 3% grid size resolution makes λ-saddle Ai (mustard-colored hexagrams) convect in the vicinity of FTLE-saddle I for

the longest time. This shows the fact that the initial discrepancy between the λ-saddle and the physical saddle is amplified, when the λ-saddle is convected forward by the flow map $\boldsymbol{\phi}(\boldsymbol{x}_0, t_0, \tau)$ (blue arrow in figure 2-7) to get its trajectory integral of the tangential rate of Lagrangian strain $S_{||}$ value (green dotted arrow in figure 2-7) and the discrepancy is stretched along the attracting LCS.

3.3.2 Materially coherent vortex via LAVD

Detection of the LEV by LAVD provides us a different Lagrangian coherent perspective of the LEV formation and separation. The LAVD-identified region of fluid belonging to the LEV is tracked backward from shedding to formation and shown at several instants (in a forward-time sequence) in figure 3-21. The LAVD region is colored by vorticity, which shows when and how the fluid acquires vorticity, and if it has entrained into the LEV or is still in the shear layer.

The phenomena we observed in figures 3-13 and 3-14 could be seen also in the contained fluid behavior, as similar shape changes to the negative vorticity over the formation time. The LAVD vortex center of the LEV and the TEV are shown in figure 3-21 and tracked in figure 3-14, which are observed at the same location as the Γ_1 function center, and give similar traces.

The LAVD region with high vorticity magnitude has a similar size comparable to the compact LEV core identified by the positive Q-criterion contours in figure 3-13. The intermittent feeding of the shear layer due to Kelvin Helmholtz-type instability of the shear layer is also demonstrated in figure 3-21(c)−figure 3-21(f) by the filamentary LAVD fluid containing vorticity between the LEV core LAVD fluid and the LAVD fluid over the plate. We note here that the blue regions identified by LAVD are materially tracked through the sequence of figure 3-21, while the green Q-criterion regions of figure 3-13 are computed in a Eulerian sense every time step.

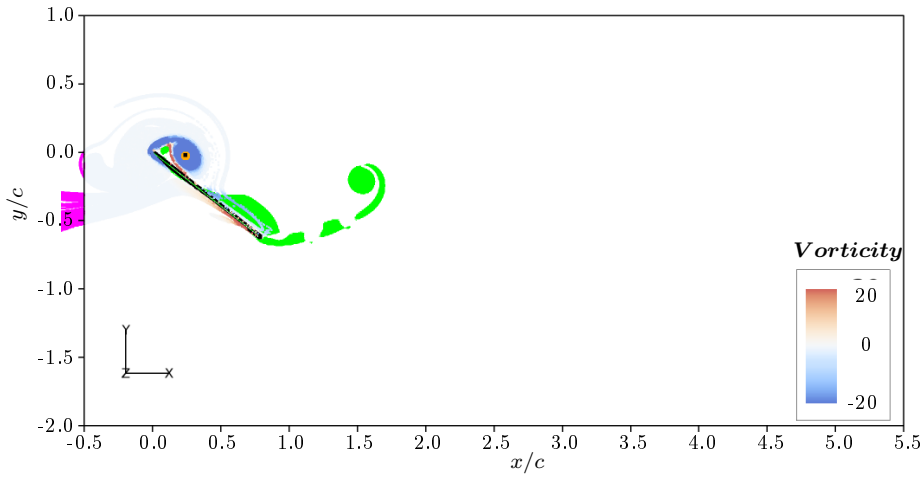

(a) $\hat{T} = 3.7$

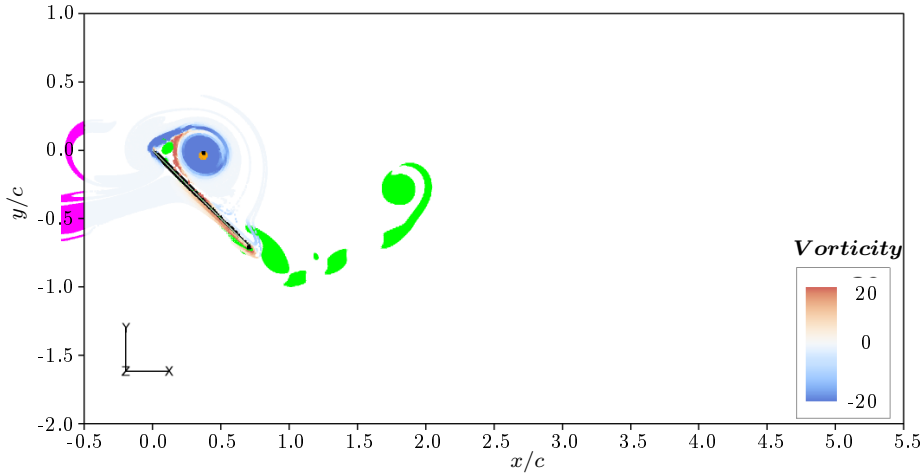

(b) $\hat{T} = 4.5$

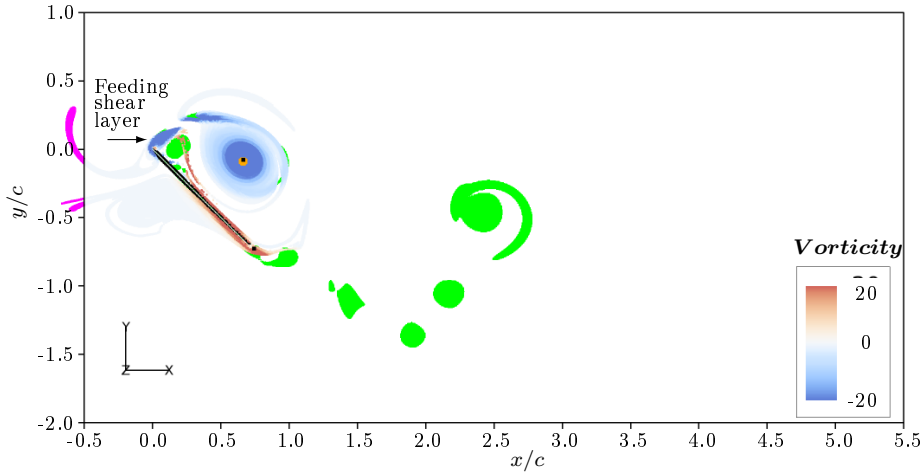

(c) $\hat{T} = 6.1$

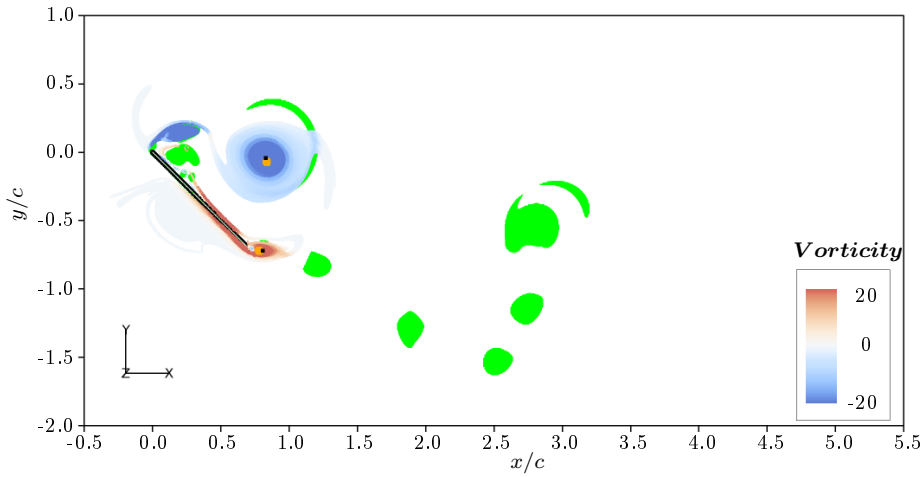

(d) $\hat{T} = 7.1$

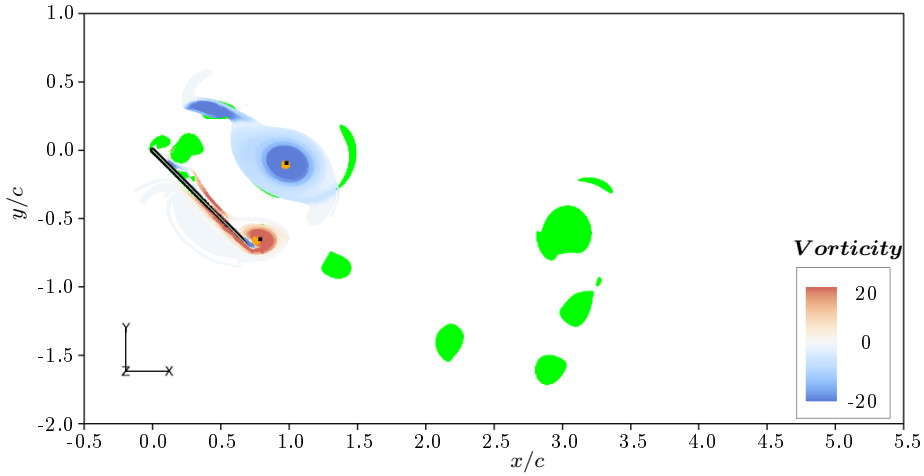

(e) $\hat{T} = 7.7$

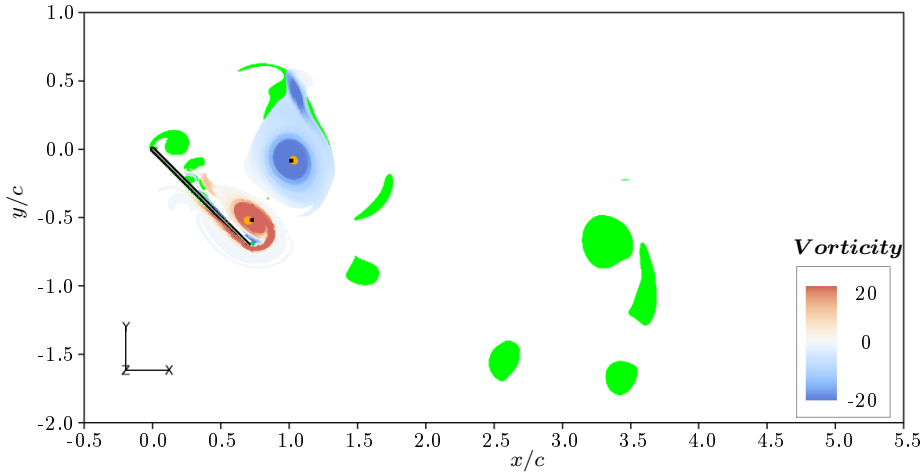

(f) $\hat{T} = 8.5$

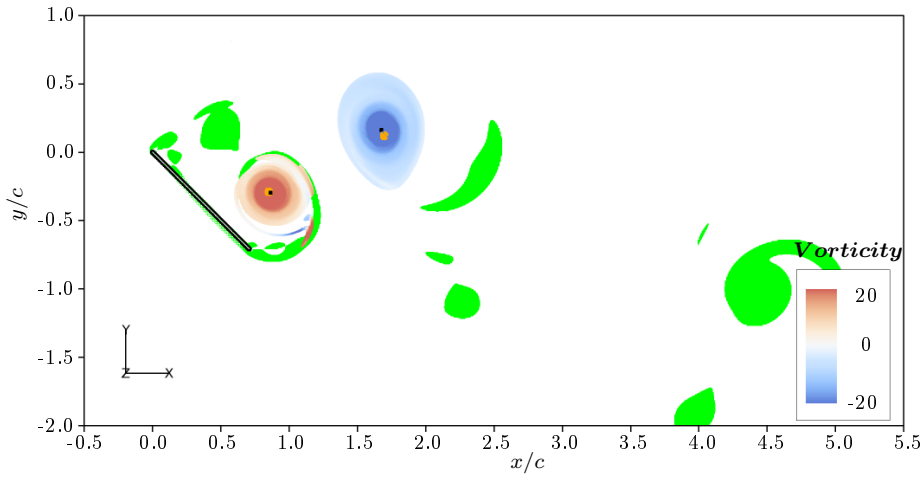

(g) $\hat{T} = 11.0$

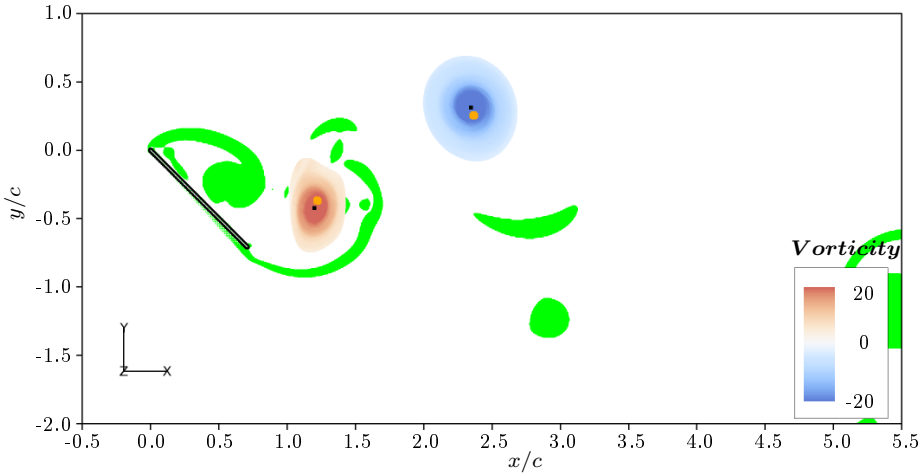

(h) $\hat{T} = 13.0$

Figure 3-21: Instantaneous flow field visualized by LAVD fluid particles. LAVD fluid is shown by contour plot of vorticity magnitude. $Q > 0$ region is shown as the green regions. Γ_1 function and LAVD vortex centers are presented by orange and black spots. Flat plate is shown as black line. LAVD fluid particles outside flow field are colored pink due to lacking information.

The feeding process of the shear layer to the LEV could be observed during its formation and shedding as shown between figure 3-21(a) and figure 3-21(d). Figure 3-21(e) – figure 3-21(h) show the LEV after all the fluid that will be entrained into the materially coherent LEV has lost contact with the plate surface. During these later times, it has coalesced into a circular shape and convected downstream.

The TEV formation process is also shown clearly by LAVD-identified fluid. After FTLE-saddle III sheds, the flow reversal from the trailing edge occurs such that a TEV develops and convects upstream. The LAVD-identified fluid from the pressure side of the plate generates counter-clockwise vorticity around the trailing edge and connects with the shear layer on the suction side, as shown between figure 3-21(d) and figure 3-21(f). Later as exhibited in figure 3-21(g) − 3-21(h), the TEV moves towards the leading edge until the topology changes then it starts convection downstream.

3.3.3 Vortex Shedding Mechanism

The Vortex Shedding Mechanism (VSM, introduced in section 2.2.2) and the its designated shedding location are shown in figure 3-22, compared with the FTLE-saddles. In this case, as stated by VSM, vortex shedding happens at locations with the zero-momentum, identified as intersections of $u = 0$ and $v = 0$ contour lines, as well as positive streamwise pressure divergence. A location with positive streamwise pressure divergence is exhibited as the white region with the blue negative pressure gradient on the right and red positive pressure gradient on the left, as shown in figure 3-22.

As we can see in figure 3-22(a), a shedding location, indicated by zero momentum point within positive streamwise pressure divergence, distinguishes the LEV from the pitching plate, and FTLE-saddle I appears at the same position. The VSM shedding location propagates with FTLE-saddle I between figure 3-22(a) and 3-22(b) till the FTLE-saddle sheds at $\hat{T} = 4.5$. A similar phenomena is observed in figure 3-22(c) − 3-22(h), the VSM shedding location appears near and propagates with FTLE-saddles II, III and IV till the saddle shedding times of $\hat{T} = 6.1$, 7.1 and 11.3, respectively.

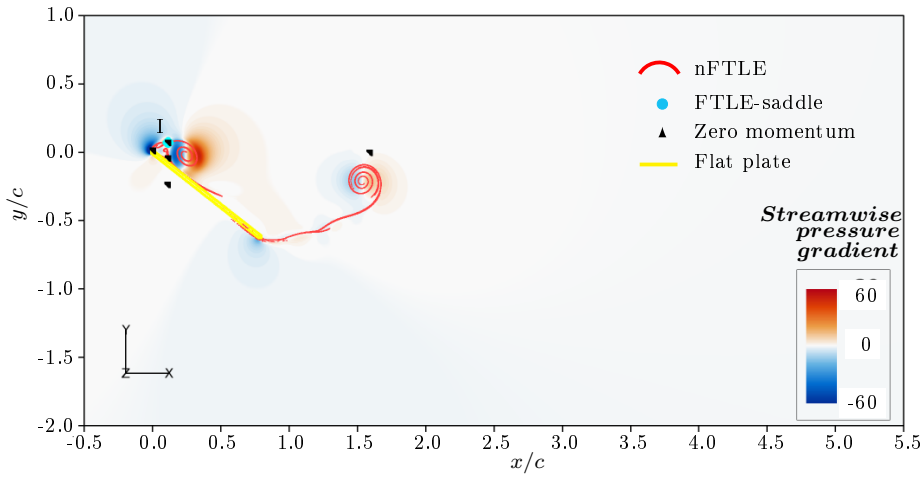

(a) $\hat{T} = 3.7$

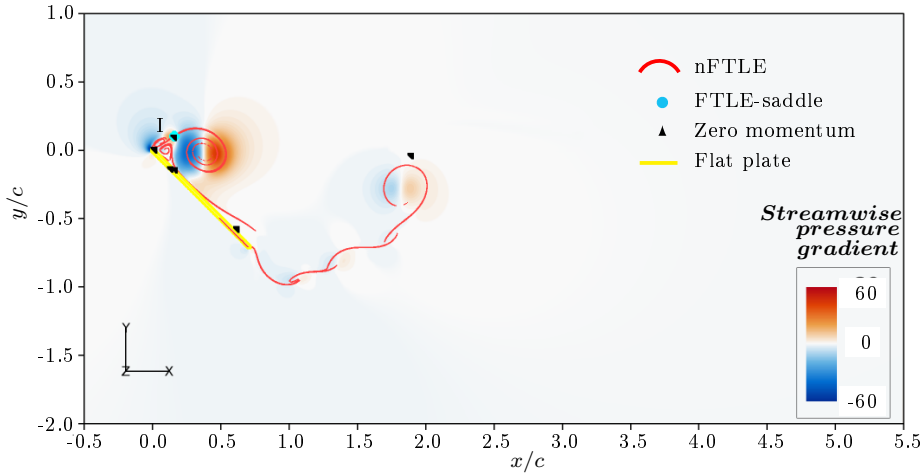

(b) $\hat{T} = 4.5$

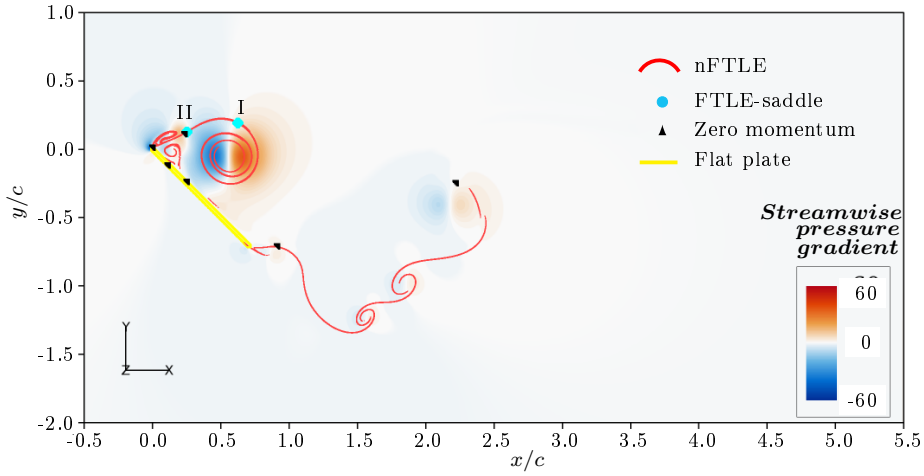

(c) $\hat{T} = 5.5$

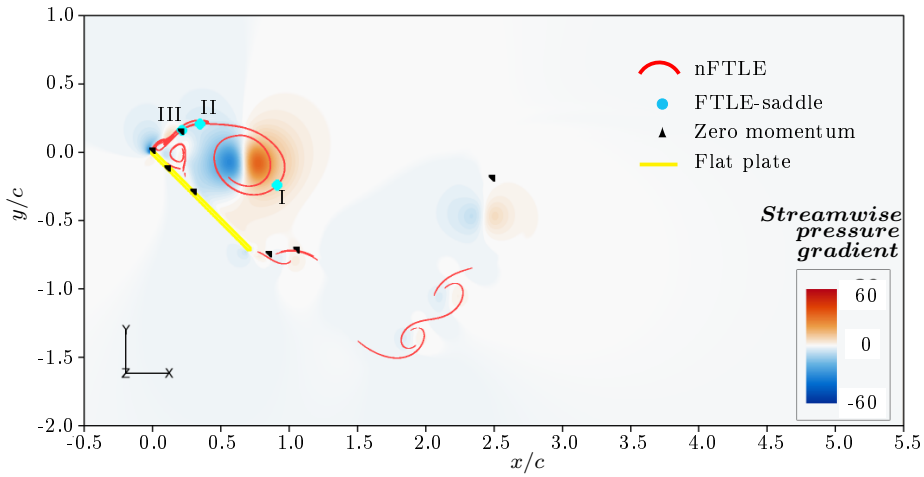

(d) $\hat{T} = 6.1$

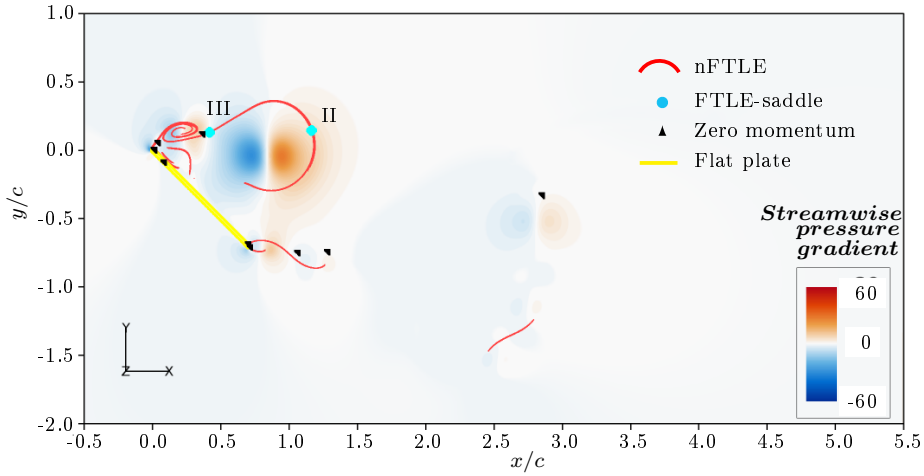

(e) $\hat{T} = 7.1$

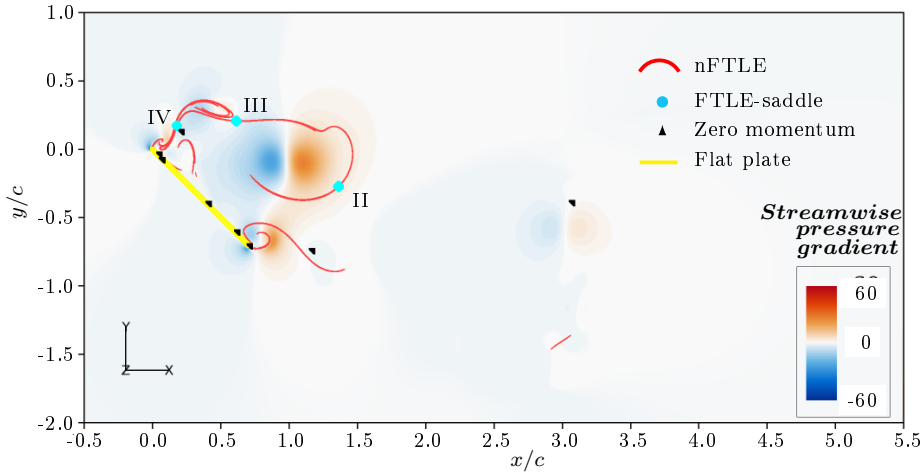

(f) $\hat{T} = 7.7$

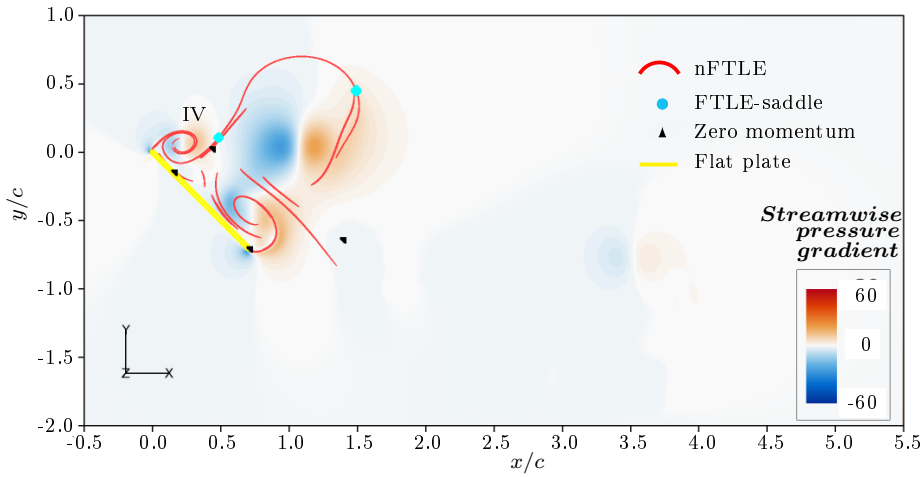

(g) $\hat{T} = 9.0$

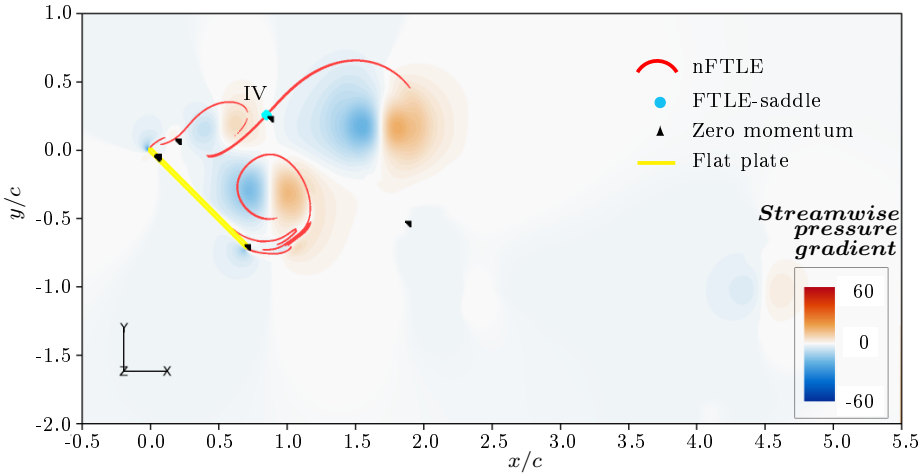

(h) $\hat{T} = 11.0$

Figure 3-22: Instantaneous vortex shedding position detected by VSM as zero momentum locations, marked by black triangle, in the white area of the instantaneous streamwise pressure gradient contour plot. nFTLE ridges are shown as red curves indicating the vortex boundary. FTLE-saddles are shown as cyan spots. Flat plate is shown as a yellow line.

Thus the role of FTLE-saddles in detecting vortex shedding can be elucidated similarly to VSM. The feeding shear layer near the FTLE-saddles at the upstream end of the LEV will become depleted of vorticity. The positive pressure gradient at the upstream of the saddle eliminates the propagation of the shear layer with the LEV, while the negative pressure gradient at the downstream of the saddle aids the convection of

the LEV downstream, which thus separates the LEV from the shear layer. The initiation and subsequent persistence of the VSM shedding location, or FTLE-saddles in our case, is responsible for the separation of the vortex from the source shear layer. There is no indication of time scale for VSM persistence in the work by Boghosian and Cassel (2016), but we suggest the it is necessary for the vortex shedding process.

It is worth noting that vortex shedding detection by the VSM does not apply to flow with moving reference frame, because the zero-momentum point, one of the necessary and sufficient condition of VSM, may not exist in this flow. Therefore the VSM is not Galilean invariant, while the vortex shedding detection by Lagrangian approaches, i.e. FTLE-saddles and λ-saddles, are frame and material invariant.

3.3.4 Shedding, circulation and force

The total circulation and the LEV circulation are studied using the methods introduced in section 3.2.2, the development of which are shown respectively in figure 3-23. The LEV circulation within a carefully chosen window is marked by magenta diamonds, and compared to the total circulation of plate shear layer marked by blue diamonds. The LEV circulation shows an increasing trend during its formation, and reaches a plateau after it has completely shed from the shear layer. The formation number N defined by Gharib et al. (1998) as the time when the total circulation equals the peak LEV circulation is in this case $N = 4.5$. The LEV formation number in this case lies in the reported range of $\hat{T} = 3.5 - 4.5$, and matches the FTLE-saddle I shedding time.

Circulation development by Q-criterion and FTLE ridges of the primary LEV is shown by green markers in figure 3-23. The circulation stops increasing rapidly after $\hat{T} = 4.0$ when plate stops pitching, then has a big jump during $\hat{T} = 8.3 - 8.4$, which could be explained by observation of figures 3-21(d) $-$ 3-21(f): after FTLE-saddle III sheds at $\hat{T} = 7.7$, additional vorticity stretches into thin layers along the boundary until collected into the LEV core. This vorticity is not in the interior of the LEV area as defined by the Q-criterion until it compresses into the area almost all at once.

As we observed in figure 3-23, the LEV feeding process is complicated, causing discon-

tinuous jumps of circulation calculated this way, for reasons including the intermittent feeding process of shear layer. It is a challenge to identify a vortex area boundary by $Q = 0$ contour level despite the use of the FTLE ridges and saddles as described in sections 3.2.2. The vortex area defined this way cannot collect all the eventual vorticity-containing fluid along the vortex boundary during the LEV formation. A closed, well defined vortex area provided by LAVD offers a more straightforward circulation calculation avoiding an ambiguous area definition.

The LEV circulation development by LAVD (as red markers shown in figure 3-23), on the other hand, is clear and continuous. The result by LAVD clearly identifies the regions of the shear layer that will end up in the shed coherent LEV while it is still forming, and it facilitates a more straightforward circulation calculation. The circulation of the LEV reaches to two peaks at $\hat{T} = 6.1$ and $\hat{T} = 7.1$ when FTLE-saddle II and III shed separately. The circulation peak time indicates that the LEV fluid has reached its saturation strength at this instant as the materially coherent LEV has ended contact with the plate surface, which coincides with when the LEV by LAVD region has shed from shear layer as shown in figure 3-13(e). The same phenomena of the LEV shedding process was observed in the research of vortex ring pinch-off by Fernando and Rival (2016), who argued that when the vortex ring pinches-off from the plate, it may not physically separate from the shear layer, which may occur later or not at all.

Before the peak time, the circulation increases with vortex formation, and maintains a relatively constant value after the second peak, showing the vortex stays materially coherent and maintains its circulation during convection despite some diffusion after $\hat{T} = 10.0$. It is worth noting that the plateau of circulation in the box window matches with the peak LAVD circulation. The time $\hat{T} = 4.0$ (when the plate stops pitching) is marked by red dotted line 'e' in figure 3-23, after which the slope of all circulation (calculated all ways) drops drastically. The circulation of the TEV by LAVD-identified fluid is shown as a trace of cyan markers in figure 3-23, with one peak around $\hat{T} = 9.0$. The circulation increases with TEV formation, then stays relatively constant after the peak.

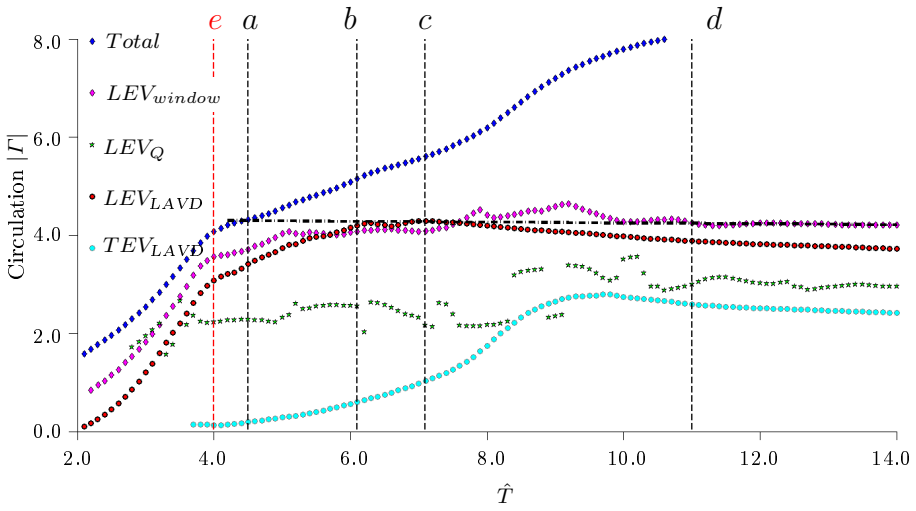

Figure 3-23: The LEV circulation development by multiple methods in formation time. Black dash lines indicate FTLE-saddle shedding times. Red dash line indicates the time at which the plate pitch-up motion stops.

The 2D lift coefficient ($C_L = L/(\rho U_\infty^2 c)$) on the 45^o pitch-up plate is shown against formation time in figure 3-24 (Wang and Eldredge, 2013). There is an initial drop in the amount of lift on the plate that occurs at $\hat{T} = 4.0$, which is associated with the end of the transient motion of the plate. After $\hat{T} = 4.0$, the fluctuations in force are associated with the unsteady fluid dynamic effects, and not the motion of the plate itself.

By comparing the FTLE-saddle shedding times and lift coefficient with respect to formation time after $\hat{T} = 4.0$, we observe that the lift drops most precipitously at $\hat{T} = 4.5$, corresponding to the formation number $N = 4.5$. The added-mass force is not considered in the case due to the fact that the plate is not moving during the period of interest(Hartloper et al., 2013; Jain et al., 2015). The observation that the timing of the lift coefficient peak matches with the LEV formation number agrees with the optimal vortex formation concept (Dabiri, 2009), and indicates the end of the LEV attachment to the plate and the beginning of the LEV shedding process from the shear layer.

As more shear layer is entrained into the LEV as shown by the increasing and second peak of circulation by the LEV LAVD-identified fluid in figure 3-23, the lift keeps decreasing with even an steeper trend until the last drop at $\hat{T} = 7.1$, when FTLE-saddle III sheds in figure 3-14.

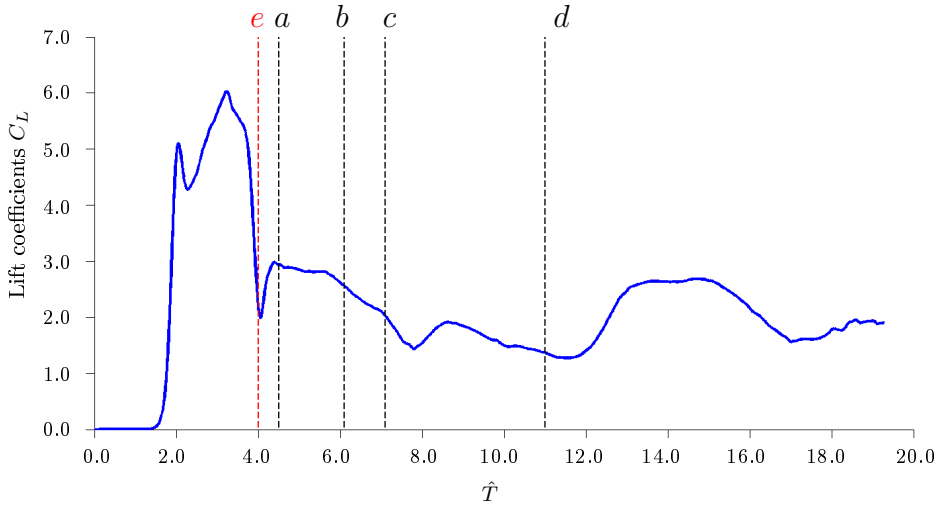

Figure 3-24: Force coefficients in formation time (Eldredge, 2007). Black dash lines indicate FTLE-saddle shedding times. Red dash line indicates the time at which the plate pitch-up motion stops.

The recovery of lift after $\hat{T} = 8.0$ is associated with the TEV formation. The lift drops close to the time $\hat{T} = 9.0$, when the circulation of TEV LAVD-identified fluid peaks. The TEV later sheds at $\hat{T} = 11.3$ along FTLE-saddle IV shedding. The continuing oscillation of the lift history between $\hat{T} = 11.3$ to $\hat{T} = 20$ continues to be related to the alternating formation and shedding of structures from the leading and trailing edges.

3.4 Discussion

In this chapter, we demonstrate the LEV separation process from a variety of different perspectives and diagnostics. Multiple vortex separation criteria are reviewed and compared, along with their connection to the shedding detection by multiple vortex visualization and tracking approaches, and pitching plate lift history. The current work shows the timing of the LEV separation and the circulation development generally fits the trend of lift history. With the vortex detection methods introduced in the chapter, we utilized multiple separation criterion, and demonstrated the vortex dynamics and time-varying vortex strength during the vortex separation process.

The behavior of both FTLE-saddles and λ-saddles correlate with the vortex shedding, which is also consistent with forces acting in two opposite directions identified from

VSM. A formation number reported in the literature is also shown to agree in this study, matching with the LEV circulation plateau. The use of LAVD to identify the region in which to calculate circulation provides a different perspective as it collects all the Lagrangian particles that comprise the final LEV during its formation. The peak in circulation found this way is considerably later than the formation time ($\hat{T} = 4.5$), but incorporates an additional region of vorticity that sheds and is entrained into the LEV after the initial LEV separation and shedding.

The application of VSM and formation number in this case provide the explanations of LEV shedding process and its influence on the plate lift coefficient fluctuation from different perspectives. The LAVD as an objective vortex criterion provides a straightforward and versatile method to study vortex strength and evolution, as well as reveals new information of vortex circulation peak and its connection to the lift coefficient fluctuation, which cannot be captured by the above Eulerian approaches.

The fact that FTLE-saddle locations match with the VSM shedding location, as well as that FTLE-saddle shedding times coincide with formation number and LAVD-identified fluid circulation peaks, shows that the FTLE-saddle is a valid approach including the most information in the vortex shedding detection. In the comparison of FTLE-saddle and λ-saddle applied for the vortex shedding detection in the massively-separated flow, i.e. the flow around a pitch-up plate, we show the utility and practicality of the 'standard method' (section 2.1.3) and the FTLE-saddle over the λ-saddle. The FTLE-saddle by the standard method constrain the discrepancy of physical saddle and numerical saddle into the size of the data grid, and avoid the error being magnified by the flow map as in the λ-saddle approach. Among all the approaches compared in this chapter for vortex shedding detection, FTLE-saddles, as a material invariant approach, provide the most consistent and detailed information during the whole LEV evolution, including vortex formation, growth and shedding.

Chapter 4

Other applications

In this chapter, we applied the combination of multiple vortex detection methods, including Γ_2 function, Q-criterion, FTLE, FTLE saddles and LAVD, into three cases of either experimental periodic or three-dimensional aperiodic flow to explore and expand their application in providing insight of flow physics.

Vortices are a key component of the unsteady flows that include propulsive wakes, flow separation, and shear layers with instability, etc. These flows often involve aerodynamic surfaces at high angles of attack or turbulent flows. When the vortices interact with aerodynamic bodies, they influence the oscillating force as introduced in chapter 3, and also play an important role in fluid mixing and instability, kinetic energy production and dissipation, mass transport and diffusion. The visualization and tracking of vortices by various detecting methods help to explain the basic physics of unsteady flows, as well as to improve vortex dominated flow modeling, prediction, and the design and implementation of control systems.

The first case studied in this chapter is a set of experimental two-component PIV data in the wake of a purely pitching trapezoidal panel, generated in the study of Green et al. (2011). Even though the flow in the wake is 3D, recent results from Kumar et al. (2016) showed the two-component assumption at midspan of the wake is a good one.

We also expand the physical observations we can make using these vortex detection techniques in the second case, a 3D fully turbulent channel flow simulation, previously used by Green et al. (2007) and originally from Kim et al. (1987). The average vortex

convection speed is computed as a function of wall-normal distance, and is compared to previously published work for validation. The third case is a single hairpin vortex (Green et al., 2007) exacted from the turbulent channel boundary layer by the method introduced by Zhou et al. (1999).

4.1 Vortex wake breakdown: 2D continually pitching trapezoidal panel

Study of the role of vortex formation, shedding and breaking-down in the wake of pitching flat plates has been previously carried out both computationally and experimentally (Buchholz and Smits, 2006, 2008; Green and Smits, 2008; Shyy et al., 2010; Zhang et al., 2010). This classic case is a first, fundamental step toward understanding the more complicated unsteady flow in the propulsive wakes (Ringuette et al., 2007).

The dataset in the current section is reconstructed from phase-averaged 2D PIV data downstream of a rigid trapezoidal panel pitching around its leading edge ($x/c = -1.0$), and an example 3D representation of the flow field is shown in figure 4-1. Experimental details about the acquisition of this data can be found in Green et al. (2011). In this figure, the x direction is aligned with the freestream flow from left to right, and the z direction is aligned with the span of the panel trailing edge. The data plane for the current work is taken at the midspan ($z/S = 0$), where S is the span of the trailing edge, and is parallel to the freestream flow. The current flow field is presented for $Re = 4200$ (based on panel chord length) and a Strouhal number of $St = 0.28$, where $St = fA/U_\infty$, with $f = 0.5Hz$ as the frequency of oscillation, $A = 20mm$ as the width of the wake, and $U_\infty = 0.036m/s$ as the freestream velocity. The peak-to-peak amplitude of the trailing edge is commonly used as an approximation for A. FTLE ridges and FTLE-saddles are determined, with an integration time of four pitching periods in the positive-time FTLE calculation, and two pitching periods for the negative-time FTLE calculation. A shaper nFTLE ridge is obtained with the same integration time compared to pFTLE, so a longer integration time is used for pFTLE to get a equally sharper ridge.

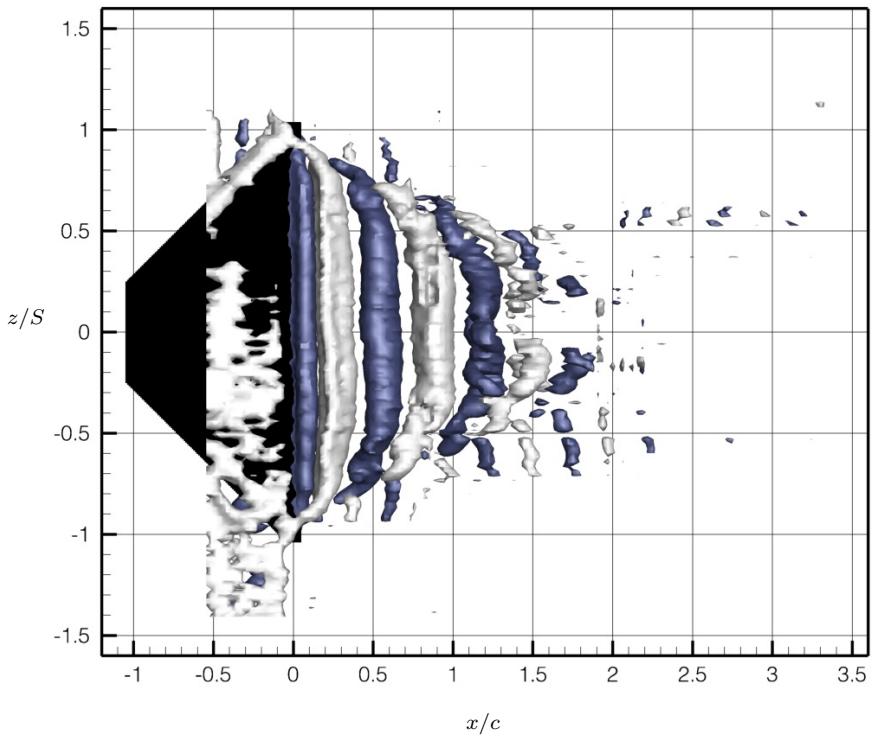

Figure 4-1: Spanwise vorticity (ω_z) isosurfaces in the flow around a continually oscillating trapezoidal panel. Panel is shown in black, positive vorticity in white isosurfaces, negative vorticity in blue isosurfaces. Vorticity isosurface level is 14% maximum and minimum ω_z. Recreated from the data set of Green et al. (2011).

The main result of the previous work was the observation of a loss of coherence in the reverse von Kármán street wake at a certain distance downstream of the pitching panel trailing edge. A von Kármán street is the flow pattern that emerges downstream of periodic shedding of alternately-signed vortices from the surface of a bluff body (Kármán, 1938; Wille, 1960). This loss of coherence in vorticity isosurfaces is evident in figure 4-1 near $x/c = 1.5$, and was shown to coincide, both in space and time, with the merging of two FTLE-saddles that belonged to the boundaries of two distinct vortex structures. The merging of the saddles indicated the interaction of the two vortex structures, and the loss of coherence of each. In the current work, we use the tracking technique from the shedding study to not only observe the merging, but to quantitatively identify the location at which it occurs.

The vortex centers are identified by the Γ_2 function, with vortex area determined by

positive Q-criterion regions, while the vortex boundaries are located by nFTLE ridges, pFTLE ridges and FTLE-saddles, as introduced in section 3.2.1. The function Γ_2 is used here instead of Γ_1 because of the large velocity of the whole vortex core, relative to the LEV velocity in the study case of chapter 3. In the first case, the LEV drifted from a relatively stable location. Here, the cores are already shed and continually moving downstream as part of the wake. As Γ_1 is not Galilean invariant, its identification of the vortex center will be affected by the vortex core motion, whereas Γ_2 will not be.

In order to use these Eulerian quantities to determine a location of breakdown, it is necessary to identify the downstream location at which both the $Q > 0$ regions or the Γ_2 centers disappear, indicating the lack of coherent rotation around them. That process, however, would be highly sensitive to a user-defined threshold on the value of Q-criterion or Γ_2 function at the center location, and it is also sensitive to data noise because Q-criterion calculation uses velocity gradient. Instead, the FTLE-saddles merging are used to indicate vortex breakdown to avoid threshold dependence.

4.1.1 Results

Figure 4-2 displays instantaneous snapshots of the wake from dimensionless time $t^* = 0.0$ to $t^* = 1.2$, where $t^* = t/T$, and T is the period of panel pitching motion. The panel is continuously pitching, and $t^* = 0.0$ is taken at the phase of motion where the panel is aligned with the flow, with the trailing edge moving in the positive y direction. From the trailing edge ($x/c = 0$) to approximately $x/c = 1.5$ downstream, the wake consists of a 2S vortex street, as two single vortices are being shed each period.

The locations of the vortex cores as identified by Γ_2 center are shown as yellow dots, and the regions of positive Q-criterion are the black round areas that give an indication of the vortex core regions. The contour setting for Q-criterion is $5\%Q_{max}$, chosen to avoid small scale noise associated with the experimental data. Further than approximately one chord length downstream, both the Q regions and the Γ_2 centers seem to disappear, indicating the destruction of the coherent vortex structures. The location of where these Eulerian metrics disappear is consistent with the previously calculated isosurfaces of vorticity, shown in figure 4-1.

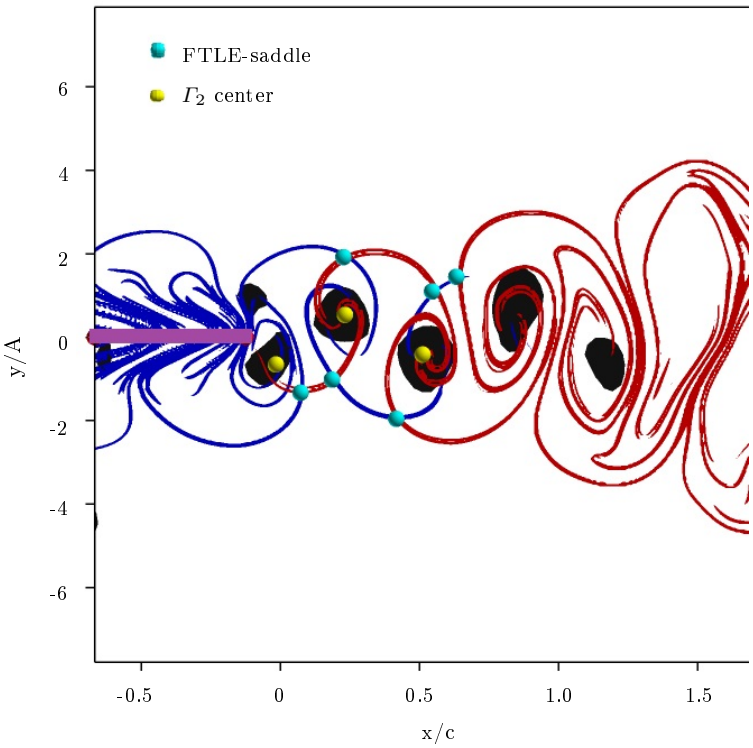

(a) $t^* = 0.0$

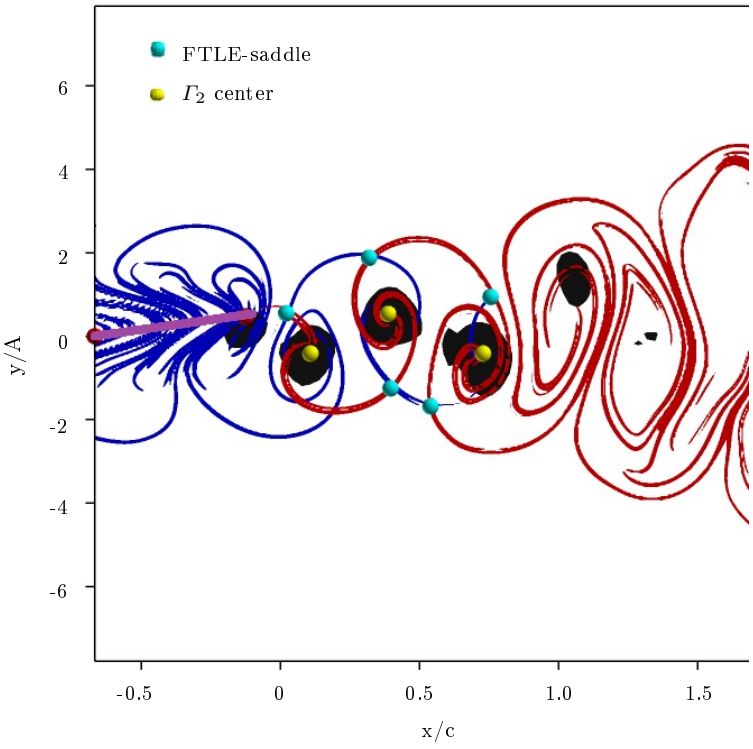

(b) $t^* = 0.3$

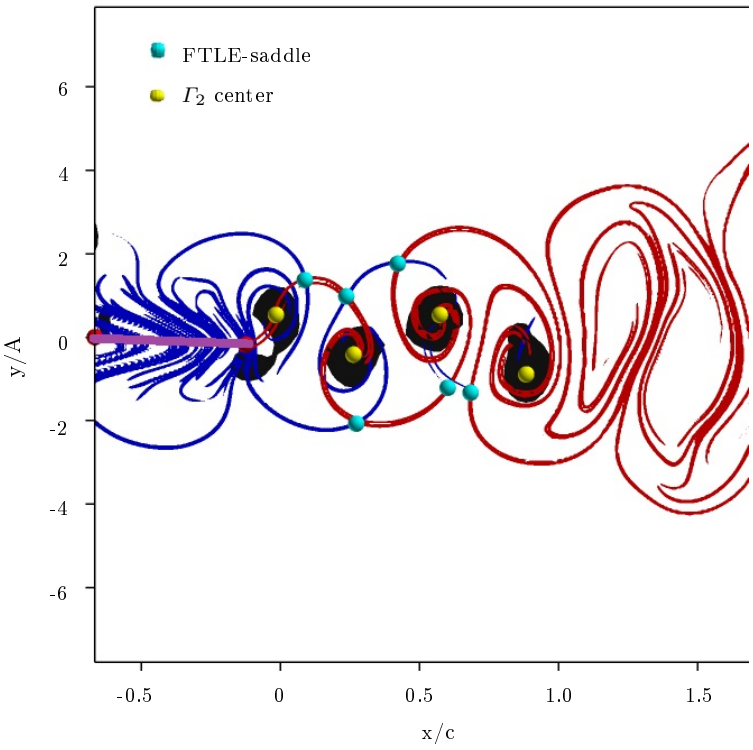

(c) $t^* = 0.6$

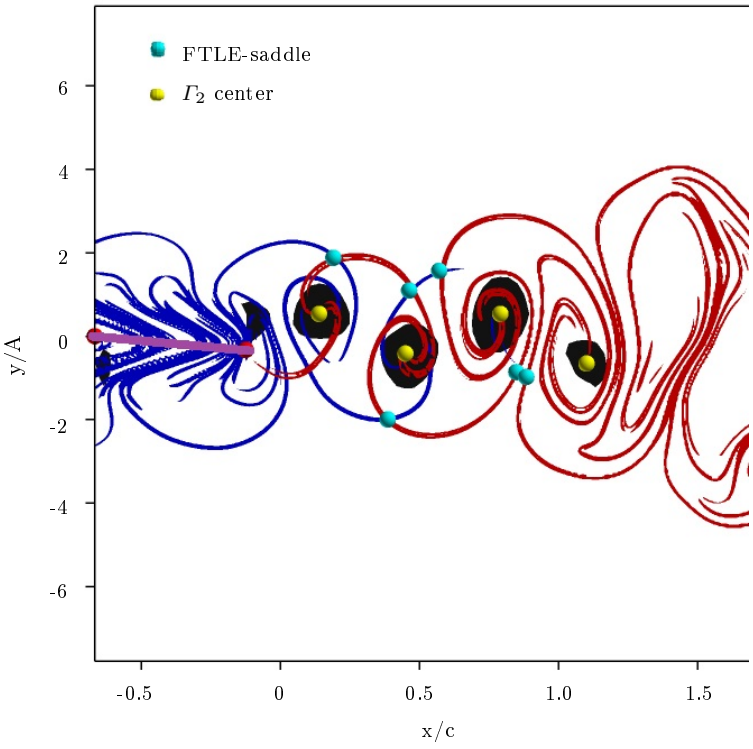

(d) $t^* = 0.9$

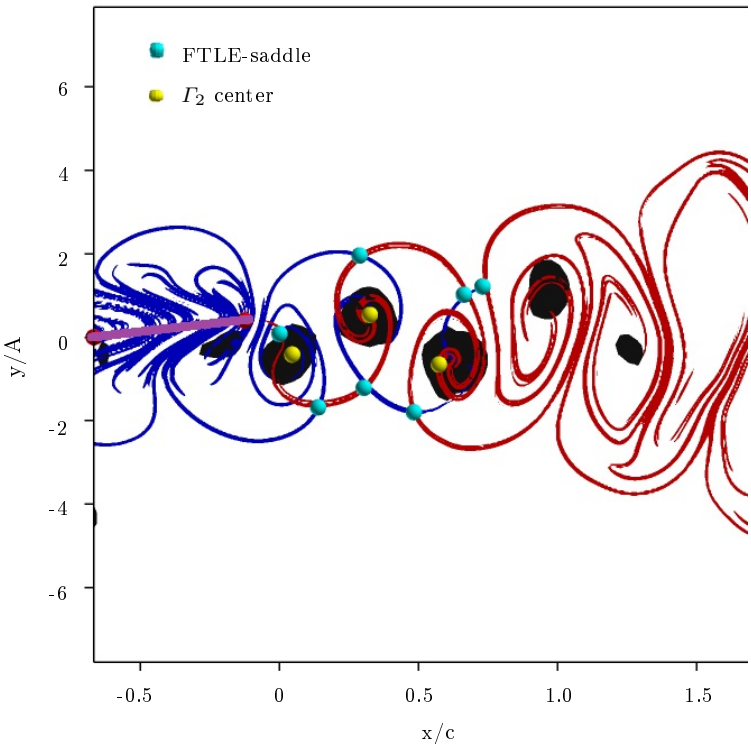

(e) $t^* = 1.2$

Figure 4-2: Instantaneous snapshots of the continuously pitching trapezoidal panel wake at $St = 0.28$. Negative- and positive-time FTLE ridges are contoured as red and blue ridges respectively, with contour level of values more than 67% maximum. Positive Q-criterion is contoured as black region with contour level at 5% of the maximum value. Panel is plotted as purple line.

In figure 4-2, it is clear that nFTLE (red curves), pFTLE (blue curves), and FTLE-saddles (cyan spots) provide a transverse boundary of the wake, and an alternating scroll pattern around the vortex cores. As each FTLE-saddle moves downstream, it approaches another FTLE-saddle associated with a vortex shed in either the previous or subsequent half-period. By approximately $x/c = 1.0$ downstream, the saddle pairs have nearly merged together entirely.

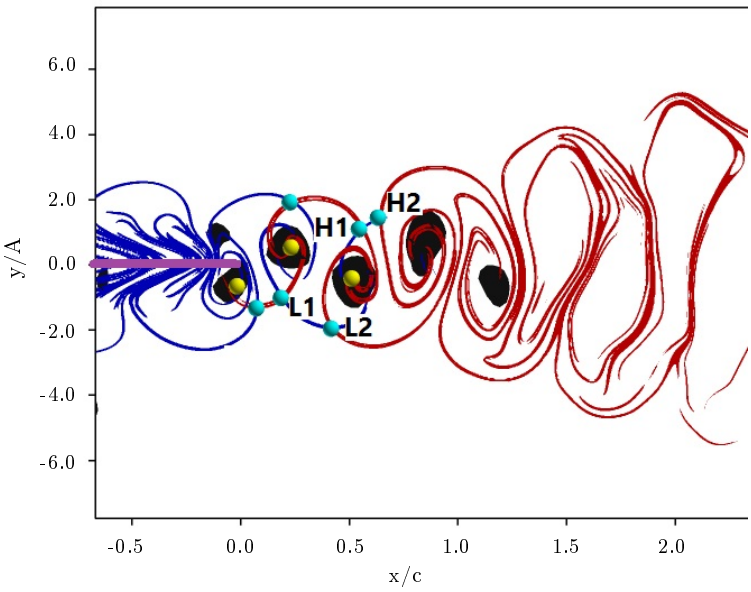

Figure 4-3: Instantaneous snapshot of marked FTLE-saddles. Negative- and positive-time FTLE are contoured as red and blue ridges respectively, with contour level of values more than 67% maximum. Positive Q-criterion is contoured as black region with contour level at 5% of the maximum value. Panel is plotted as a purple line.

Figure 4-3 shows one snapshot of this wake, with the FTLE-saddles labeled as they are referenced in figure 4-4. There are four markers labeled, two each that belong to boundaries of two subsequent structures along the centerline of the wake. They are labeled with either an 'H' to represent that they are on the higher half of the figure as presented, or 'L' to represent that they are on the lower half of the figure as presented. Each of the distinct vortex cores has one H saddle and one L saddle, and as seen in figure 4-2, we expect the lower saddles to merge together, and the higher saddles to merge together. In particular, L1 and L2 are shown to approach merger in figure 4-2(d) at $y/A \approx -1$ and $x/c \approx 1$. H1 and H2 are shown to approach merger in figure 4-2(e) at $y/A \approx 1$ and $x/c \approx 0.8$.

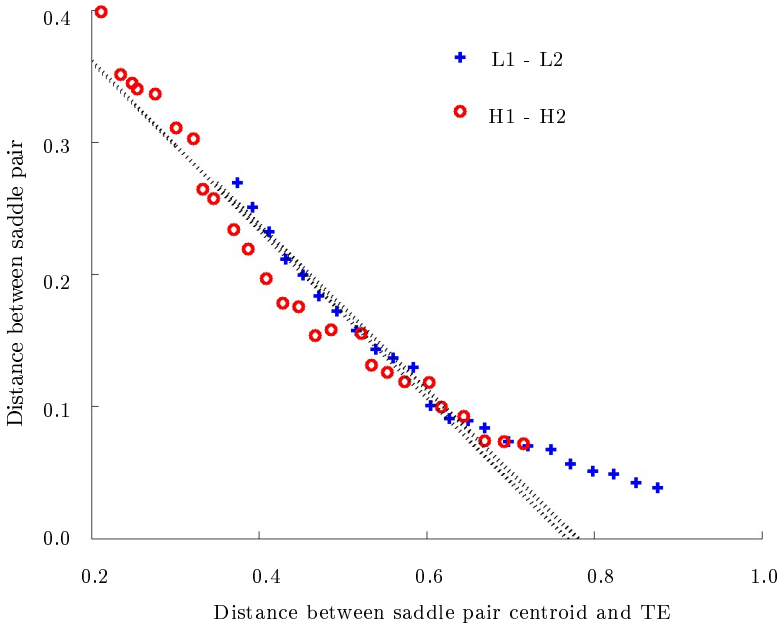

Figure 4-4: Decreasing distance between pairs of FTLE-saddles compared to downstream distance of the pair's centroid. Two dotted lines indicate linear curve fits to the decreasing pair distances from upstream. Linear fit was performed for FTLE-saddle distance upstream of $x/c = 0.6$.

In figure 4-4, the distance between the labeled H saddles and the distance between the labeled L saddles is presented as a function of the downstream distance of each pair's centroid. Both trace out a similar path as they move downstream, with an apparent deceleration of the merging occuring downstream of approximately 0.6 chord lengths. This is observed as a shallowing of the slope of the two curves. As seen in figure 4-2(d), the lower half saddles approach each other at $x/c \approx 0.8$, and the two red nFTLE ridges that are associated with each of the two saddles become parallel to each other, but can never intersect. Therefore the distance between the saddles will never go identically to zero. For this reason, we take the slope of these curves from trailing edge to $x/c = 0.6$, and find that both the upper half saddles and the lower half saddles have a projected merge location of $x/c = 0.8$ chord lengths downstream at $St = 0.28$.

In the previous work, the location of the vortex wake breakdown that accompanies the FTLE-saddle mergers was shown to move upstream with increasing Strouhal number.

By using the Lagrangian analysis, a more direct and consistent analysis of the breakdown location is possible, and as in the current results, can identify and track these structures with relatively less user interaction.

4.2 Vortex convection: 3D fully-developed turbulent channel flow

Fully developed 3D channel flow has been studied extensively to increase the understanding of the basic physics of wall-bounded turbulent flows. Vortex identification and tracking in the channel flow is important for the quantitative and qualitative investigations of complex turbulence interactions near a wall. It also helps the design and testing of turbulence closure models, independent of whether the flow is treated as a stochastic flow field, a network of vortices, or a superposition of waves (Robinson, 1991).

The vortex convection velocity is of fundamental interest as vortical structures play a dominant role in transport phenomena in turbulent flows. As indicated in the literature (Robinson, 1991), individual vortex structures are not expected to propagate at the speed of the mean flow. The velocity of structures varies among vortices, and for one given vortex, its convection velocity will change with time and location in a turbulent channel flow. Kim et al. (1987) and Kim and Hussain (1993) previously showed the variation of average structure convection velocity with wall-normal distance in turbulent channel flow using Eulerian space-time correlations of velocity and pressure fluctuations. Their study found that structure convection velocity is slightly less than the local mean velocity for most of the channel, except in the near-wall region. The Eulerian space-time correlation method has been fundamental to statistical theories of turbulence and its modeling since the 1940s, but it does not retain sufficient information, i.e., the energy transfer among small scales which are convected by large scales (Squires and Eaton, 1991), or the ability to disperse contaminants suspended in the turbulent flow (Kraichnan, 1965). The current study also calculates the streamwise structure convection velocity, but using cross-correlations of FTLE-saddle locations which reveals the transport phenomena in

the turbulent flow from the perspective of the Lagrangian coherent structure.

Here, the temporally and spatially averaged convection velocity is measured on 2D planes parallel to the wall. This is accomplished by tracking FTLE-saddles in each plane to determine their average streamwise velocities. The statistical average of the convection velocity has practical application, such as in aeroacoustic studies where structure velocity can indicate the time and velocity scales of the most dominant features that produce aerodynamic forces and sound (Kim and Hussain, 1993).

The 3D, fully turbulent channel simulation for this study was run at $Re_\tau = 180$, with $Re_\tau = u_\tau h/\nu$, where u_τ is the friction velocity, h is the channel half-height, and ν is the kinematic viscosity. In these quantities, $u_\tau = (\tau_w/\rho)^{1/2}$, where τ_w is the shear stress at the wall and ρ is the density. The computational domain is $x/h \in [0, 2\pi]$ in the streamwise direction, $z/h \in [0, 2\pi]$ in the spanwise direction, and $y/h \in [-1, 1]$ in the wall-normal direction. It is bounded by walls at y/h = -1 and $y/h = 1$, and has periodic boundary conditions in the streamwise and spanwise directions. Distance from the wall can also be represented in terms of $y^+ = u_\tau y/\nu$.

This simulation was used by Green et al. (2007), and was based on that of Kim et al. (1987). For the case shown here, a non-dimensional integration time of $\tau^+ = 27$ was used for the flow map computation with integration time steps of $\Delta t^+ = 0.09$. Both integration time and time step were non-dimensionalized by $\tau^+ = tu_\tau^2/\nu$. The integration time was chosen based on previous results, and yields well-defined FTLE fields. As can be seen in figure 4-5, shorter integration times can result in less sharp FTLE ridges, but by $\tau^+ = 27$, the FTLE ridges are converged. Longer integration of the flow map to $\tau^+ = 36$ or $\tau^+ = 45$ does not change the ridge locations, only sharpens them. The values of FTLE along the ridges decrease, which can be expected because the denominator of equation 2.8 is increasing, but the particle trajectories that were initialized near the ridges may have left the vicinity of structures and may not be continuing to separate.

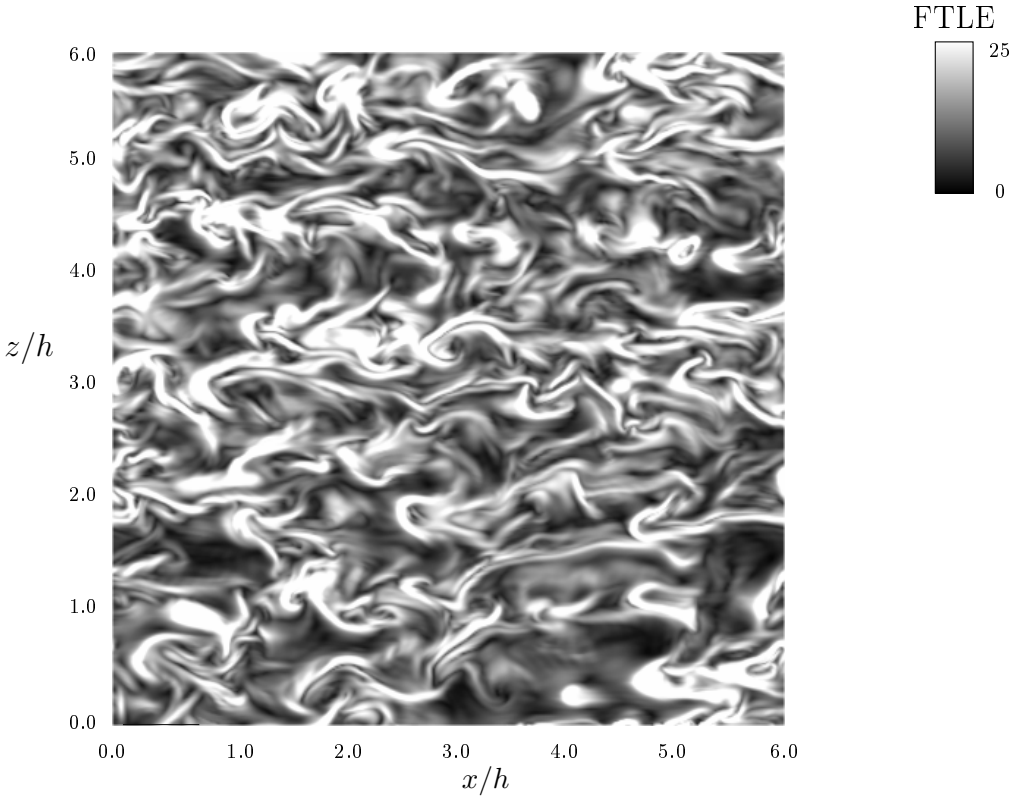

(a) $\tau^+ = 9$

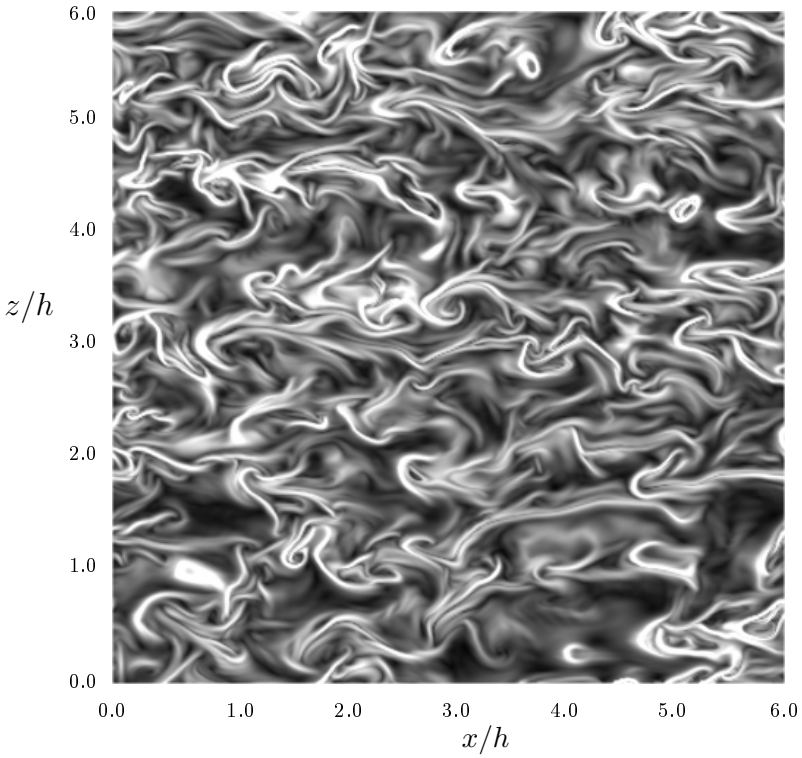

(b) $\tau^+ = 18$

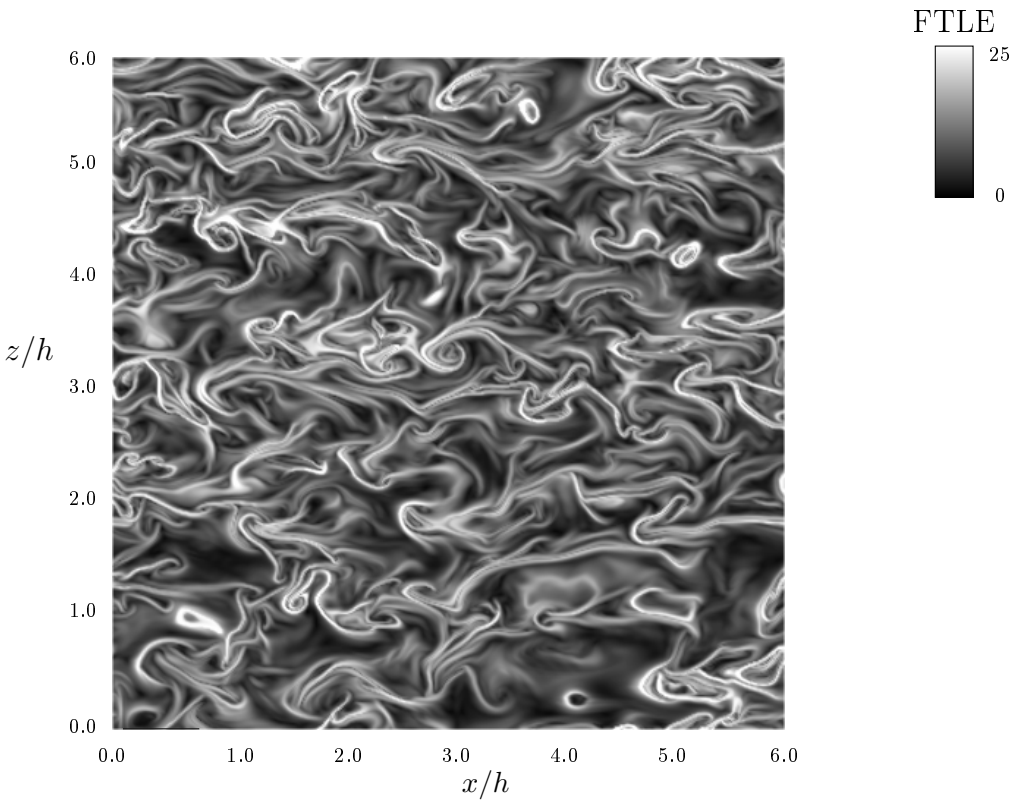

(c) $\tau^+ = 27$

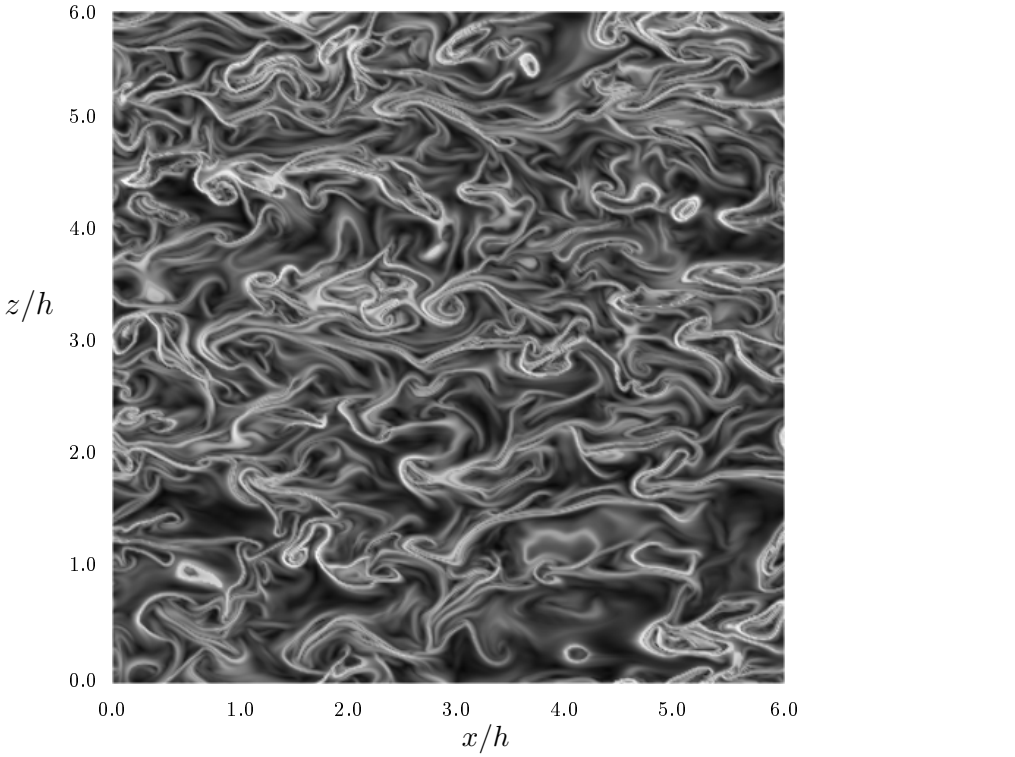

(d) $\tau^+ = 36$

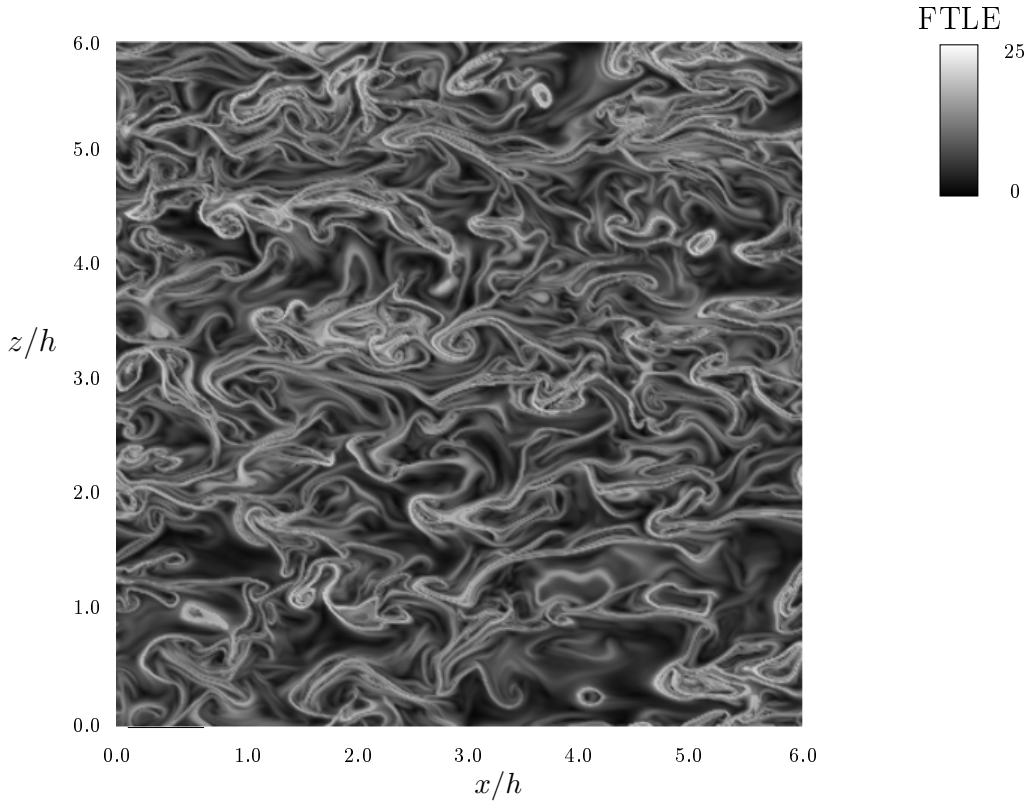

(e) $\tau^+ = 45$

Figure 4-5: Negative-time FTLE fields in a plane located at $y^+ = 49.6$ for five different integration times, as indicated. All five figures use the same color axis as shown.

4.2.1 Results

In this study, the averaged structure convection velocity at each wall-normal location was found by tracking the FTLE-saddles in wall-parallel planes of the channel flow. Fields of nFTLE in this data were originally presented by Green et al. (2007), but the current study manages to detect and track FTLE-saddles automatically from processed nFTLE and pFTLE data sets. Figure 4-6 shows FTLE ridges on 2D planes at $y^+ = 10.5$ and $y^+ = 49.6$ in the turbulent channel at one representative time. Positive- and negative-time FTLE ridges are shown as blue and red curves, respectively, and cyan dots locate the FTLE-saddles at the intersections of the pFTLE and nFTLE ridges. While 2D cuts of the FTLE surfaces are shown here as FTLE ridges, the full 3D domain is used for the FTLE calculation.

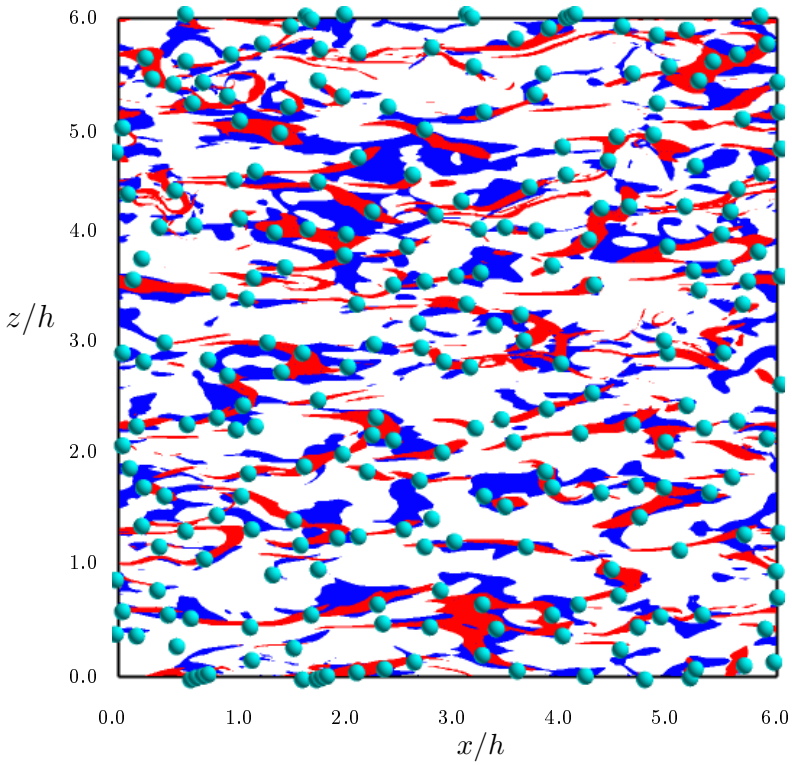

(a) $y^+ = 10.5$

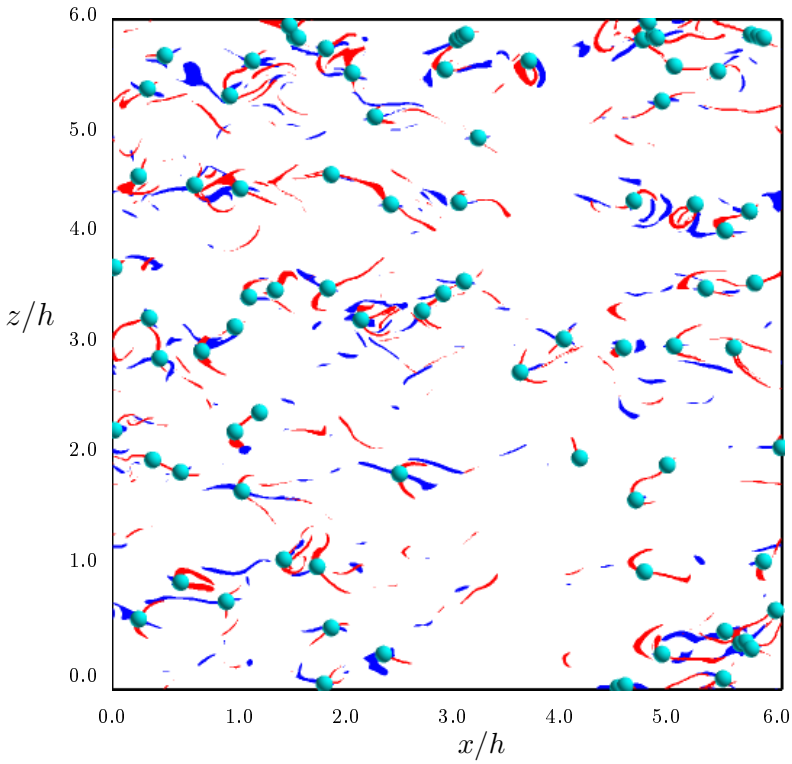

(b) $y^+ = 49.6$

Figure 4-6: Instantaneous snapshots of pFTLE ridges (blue) and nFTLE ridges (red) (values above $0.65FTLE_{max}$) at (a) $y^+ = 10.5$ and (b) $y^+ = 49.6$ in the turbulent channel simulation. FTLE-saddles are highlighted by cyan dots.

The ridges of the FTLE field are codimension-one structures, meaning that in 2D flows, they are one-dimensional curves. In the case of the turbulent channel, which is 3D, the FTLE ridges will be 2D curved surfaces in space. In figure 4-6, although the flow maps were only initialized in a series of single planes, they were advected in the full 3D data domain. For this reason, the ridges in figure 4-6 can be considered the intersection of the 2D FTLE maximizing surfaces with these particular planes. The saddles, which are the intersections of the FTLE ridges, are codimension-two, meaning that they are points in 2D flows, and one-dimensional line segments in 3D flows. The saddle points of figure 4-6 are then intersections of the saddle curves with the shown 2D planes. It is expected that the saddle line segments can also be moving in the wall-normal direction, and therefore the streamwise velocity could also be including line segment growth, bending, or rotation. The results obtained from the numerical hotwires used by Kim and Hussain (1993), however, would be subject to the same errors.

FTLE ridges and FTLE-saddle locations were identified for a series of twelve time-resolved snapshots at each of the 129 planes across the channel height. Using an adaptive cross-correlation algorithm by Dantec DynamicStudio for every two sequential snapshots of cyan saddles, one average streamwise velocity of the saddles at each plane was then calculated for each image pair. The algorithm is an iterative and adaptive cross-correlation based displacement estimator combined with window shifting, window deformation, and sub-pixel analysis. In particle image velocimetry analysis, it iteratively adjusts the size and the shape of the individual interrogation areas during processing in order to adapt to local particle densities and flow gradients. For the current study, streamwise convection velocity of saddles in each pair of snapshots was estimated from saddle displacements inside interrogation areas that were chosen as the whole 2D plane. This resulted in one average saddle velocity per instant in time per plane, which were then averaged together for the data points shown in figure 4-7. The structure convection velocity is non-dimensionalized using the friction velocity: $u_c = u/u_\tau$. As shown in figure 4-7, one standard deviation of the resulting convection velocity is less than 10% of the mean velocity for most sections of the channel, with the exception of planes close to the channel center, due to the existence of fewer saddles in this region, and very close to the wall,

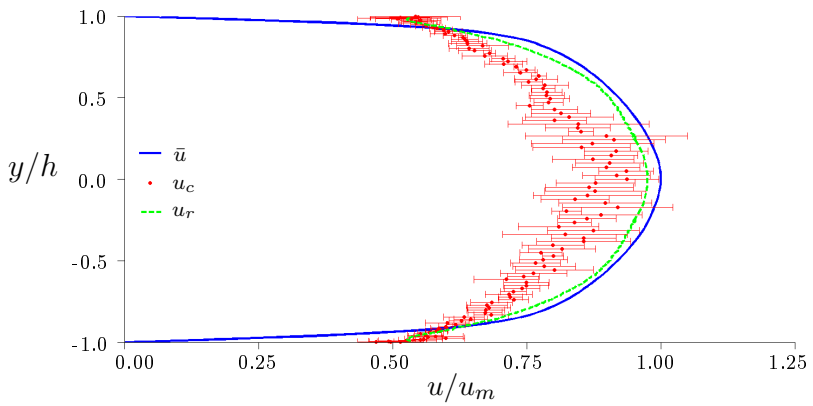

Figure 4-7: Dimensionless plane-averaged velocity of FTLE-saddles u_c/u_m (u_m is the mean velocity at the centerline of the channel) in the turbulent channel simulation is shown against wall-normal distance (red). This data is compared with the dimensionless simulation mean streamwise velocity $\bar{u}/u_m$ profile (blue), and the dimensionless streamwise propagation velocity of the velocity fluctuation u_r/u_m from the space-time correlations by Kim and Hussain (1993) (green). The error-bars in the figure are one standard deviation of the measured FTLE-saddle convection velocity in the plane.

where the saddles are hard to extract, due to lack of sharpness of the pFTLE ridges and nFTLE ridges caused by the shorter time scales. The plane-averaged transverse convection velocities of FTLE-saddles for all the planes have near-zero mean values ($v_c \cong 0.03$), and have an average standard deviation of 3% of the mean convecting velocity, with a maximum of 11% of planes close to the channel center, which is also due to the existence of fewer saddles in this region.

For comparison, the channel mean streamwise velocity $\bar{u}$ is included as a solid blue curve in figure 4-7, and the streamwise propagation velocity of the velocity fluctuation u_r/u_m from the space-time correlations by Kim and Hussain (1993) is also shown on the same axes. Here, we refer to the vortex convection velocity from Kim and Hussain (1993) as the velocity fluctuation propagation velocity. All the velocities are scaled by the mean velocity at the turbulent channel centerline for comparison. The structure convection velocity from the FTLE-saddles, u_c, is approximately 10% - 15% less than the mean profile velocity $\bar{u}$ for a large segment of the channel width: $-0.92 < y/h < 0.92$ ($y^+ > 14$). Close to the wall ($y^+ \leq 14$), the velocity of the vortices is larger than the channel mean profile velocity. While this is consistent with the physical interpretation

that vortices will travel faster than the viscous-dominated mean velocity close to the wall, the average velocity data in that region may not be statistically converged. Even though the channel mean velocity reaches zero close to the wall, the vortex structure convection velocity could be significant in the region due to perturbations caused by vortices advecting away from the wall. As shown in figure 4-7, Kim and Hussain (1993) and Kim et al. (1987) observed that the velocity fluctuation propagation velocities are slightly smaller than the local mean velocity for portions of the channel away from the wall ($y^+ > 15$), but that they are higher near the wall ($y^+ < 15$). The velocity profile of the current study agrees with the previous research, while the magnitude of the velocity fluctuation propagation velocity is higher than the convection velocities of FTLE-saddles for portions of the channel away from the wall ($y^+ > 15$). The previous research found that in sections near the wall ($y^+ < 15$) the structure convection velocity stays constant at 55% of the centerline velocity while the local mean velocity decreases until it is zero at the wall, indicating that the movement of vortices in this region is dominated by convection not viscosity.

The current study, which used automatic tracking of FTLE-saddles, was consistent with previous results that used correlations of velocity and pressure. This shows the validity of using FTLE-saddles to track vortices directly, avoiding the fluctuating velocity or pressure components that can be sensitive to small errors typically found in experimental data. FTLE ridges, and therefore FTLE-saddle points found from them, are robust to small magnitude or short duration velocity field errors (Haller, 2002).

4.3 Vortex evolution: 3D hairpin vortex

In section 4.2, some statistical quantities of vortex dynamics in the complex 3D turbulent flow, even in the boundary layer region, are revealed by vortex identification methods. The Lagrangian coherent structures show promising performance in tracking and identifying relatively larger scale vortices in the freestream compared to the small structures with short time scale. In the current section, we intend to extend this part of work by study of the hairpin (HP) vortex behavior with the application of quantitative analysis

techniques and criteria for more details and explanation.

HP vortex is a typical vortical structure in a turbulent boundary layer, and consists of an Ω-shaped head with a pair of counter-rotating quasi-streamwise legs usually not at equal strength. Spanwise asymmetric one-sided HP vortices ('canes') near the wall have also been observed (Theodorsen, 1954; Robinson, 1991; Guezennec, 1989). Its properties (size, vorticity, energy) and dynamic phenomena (origin, growth, breakdown) have been shown to correlate to the complex, multi-scaled turbulent motions observed in both experiments and simulations.

Passage of a rapidly lifting HP head and the strong pumping of fluid between the HP legs create a 'burst' event, which is a sequence of 'ejection' events: events in the second quadrant corresponding to negative streamwise fluctuations being lifted away from the wall by positive wall-normal fluctuations ($u' < 0, v' > 0$) using quadrant analysis (Adrian, 2007). The pumped fluid encounters the high-speed free-stream fluid resulting near-wall shear layers, which correlates to increase of the wall shear stress and boundary layer momentum (Brown and Thomas, 1977; Adrian et al., 2000; Ganapathisubramani et al., 2003; Tomkins and Adrian, 2003; Hutchins et al., 2005; Smits et al., 2011). The near-wall spanwise spacing of low-speed streaks is associated with the spanwise width of the HP legs, and the characteristic 30° to 50° angle seen in the structure of wall turbulence is also associated with the angle at which HP vortices incline with respect to the wall (Kim and Adrian, 1999; Tomkins and Adrian, 2005; Guala et al., 2006; Balakumar and Adrian, 2007; Monty et al., 2007). Experimental and numerical research (Bakewell Jr and Lumley, 1967; Head and Bandyopadhyay, 1981; Perry and Chong, 1982; Perry et al., 1986; Zhou et al., 1999; Adrian et al., 2000; Adrian, 2007; Wu and Moin, 2009) in wall-bounded turbulence revealed that the HP vortices are scattered randomly in streamwise and spanwise directions within an organized packet (shown in figure 4-8).

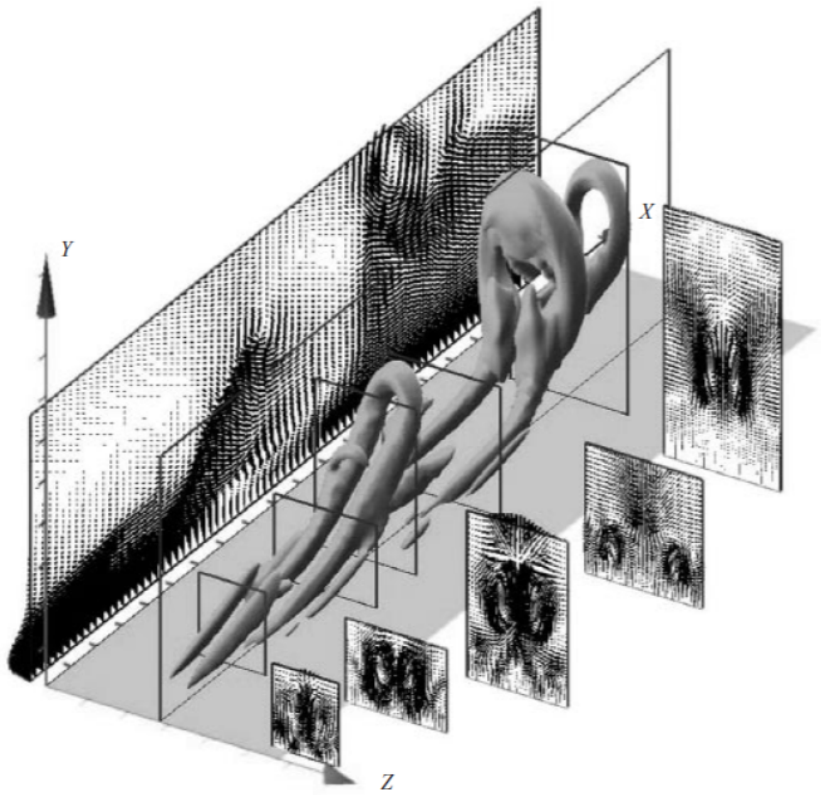

Figure 4-8: Hairpin vortices packet generated by DNS, visualized by iso-surfaces of λ_{ci}^2 (image courtesy of Zhou et al. (1999))

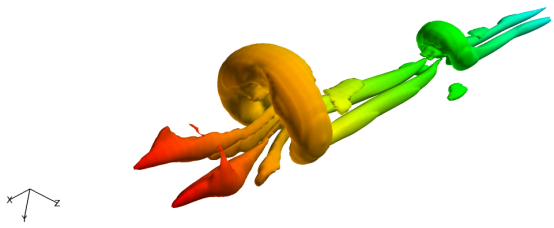

Figure 4-9: Hairpin vortex packet visualized by Q-criterion with isosurface level of 2% maximum, colored by streamwise location to aid visualization.

The physical process of the new HP vortex auto-generation on the wall and its evolution to large-scale motions (LSMs) farther from the wall was initially provided by Smith et al. (1991) with a model supported by unsteady surface-layer separation theory and

'kernel' experiments. This research also provided an explanation for the kinematic behavior of boundary-layer and channel flow based on HP vortex dynamics. Zhou et al. (1999) extended the study to address in detail the mechanisms responsible for the auto-generation of HP vortices, as well as discussion of the characteristic shape of the resulting HP packet. Adrian et al. (2000) used PIV to study the high-resolution velocity field measurements within the turbulent boundary layer, and revealed that HP vortices align one behind other within the packet, usually as an existing HP vortex (e.g., primary hairpin (PHP)) followed by a sequence of younger HP vortices (e.g., secondary hairpin (SHP)) on its upstream end that arise from a process of auto-generation, all of which results in a series of long near-wall low-speed streaks.

Adrian (2007) discussed HP vortex packet formation and organization, and its growth into larger-scale structures than the boundary layer thickness by LSMs. Vortex identification methods, i.e. FTLE and λ_{ci}^2, were applied by Green et al. (2007) to reveal the evolution of the single HP vortex into a packet of similar structures, and to show that the birth of a SHP vortex corresponds to a loss of hyperbolicity along the LCS. Jodai and Elsinga (2016) used time-resolved tomographic PIV to study the evolution of HP vortex, and argued that the SHP is initiated by an approaching 'sweep' event with associated fourth quadrant velocity fluctuations ($u' > 0$, $v' < 0$), perturbing the shear layer that contains an existing HP packet.

A previously generated simulation of an isolated HP vortex by Green et al. (2007), with the method introduced by Zhou et al. (1999), is used to study the auto-generation of a SHP vortex structure (shown in figure 4-9). The single HP vortex was generated by DNS from the simulation of turbulent channel flow in section 4.2, with an initial condition extracted by the linear stochastic estimation. The initial condition is identified as the statistically most probable flow field from the turbulent channel flow, that has a prescribed ejection event (a signature of HP vortex) at a prescribed point. More details of the data set can be found in Green et al. (2007). Eulerian methods, i.e., the Q-criterion and Γ_2 function, as well as Lagrangian methods, i.e., FTLE and LAVD, are used to visualize the 3D HP vortices and the auto-generation process. The circulation development and wall-normal location of both PHP and SHP heads are studied to determine if there

is a correlation between the strength and height of the primary HP vortex with the SHP vortex auto-generation.

Both the PHP and SHP heads are identified at the mid-span cross-section of the channel due to the approximate symmetry of the flow field through the HP heads (shown in figure 4-10). The vortex center of the HP head is identified by local maxima of Γ_2 function at the mid-span cross-section of the channel, and the vortex area boundary of the HP head is picked by $Q = 2\%Q_{max}$ level set surrounding Γ_2 function center. Both negative- and positive-time FTLE ridges will be plotted at the mid-span cross-section to indicate the HP vortex auto-generation process as elucidated in Green et al. (2007). The FTLE fields are calculated using the full 3D data set despite the fact that a 2D plane is shown in figure 4-10(c). A non-dimensional integration time of $\tau^+ = 27$ was used for the FTLE computation with integration time steps of $\Delta t^+ = 0.09$ in this case. Both integration time and time step were non-dimensionalized by $\tau^+ = tu_\tau^2/\nu$. 2D HP head circulation is calculated in the identified vortex area as a measurement of HP head strength (Zhou et al., 1999). As introduced in section 2.1.7, the circulation of the 2D HP head vortex is calculated by equation 2.16 using the vorticity of the mid-span cross-section plane (ω_z) within the vortex area. The development of the HP head circulation is studied during the HP auto-generation process.

3D LAVD is applied to reveal some details of HP auto-generation. Similar to the method introduced in section 3.2.3, the 3D LAVD is calculated from dimensionless time $\tau^+ = 189.0$ (after SHP vortex is formed), and through a backwards integration to $\tau^+ = 184.5$. A relatively short LAVD calculation period is chosen to avoid a scenario in which a too long integration time involves too many fluid particles entraining into or detraining from the SHP head, which makes it hard to separate LAVD-fluid of SHP from the shear layer close to the wall. To identify HP vortex with 3D LAVD, the LAVD boundary is identified at the mid-span cross-section of the channel, by an LAVD iso-contour level set that satisfies a chosen arc-length and convexity deficiency (shown in figure 4-11).

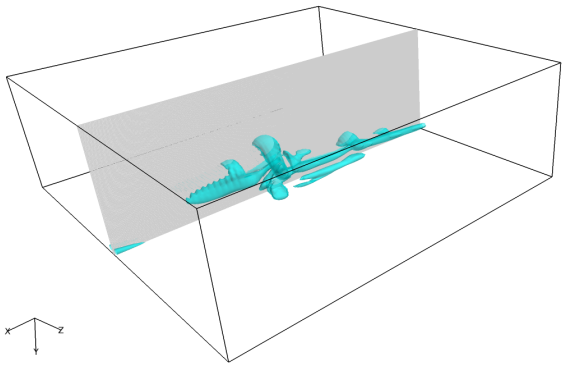

(a)

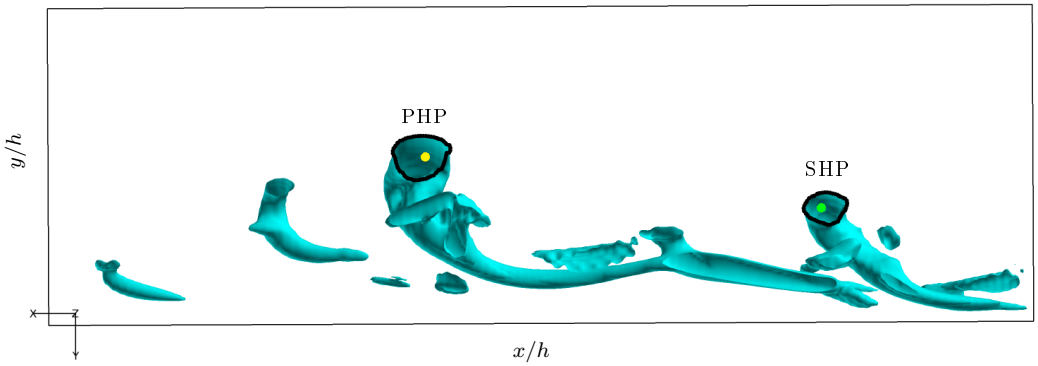

(b)

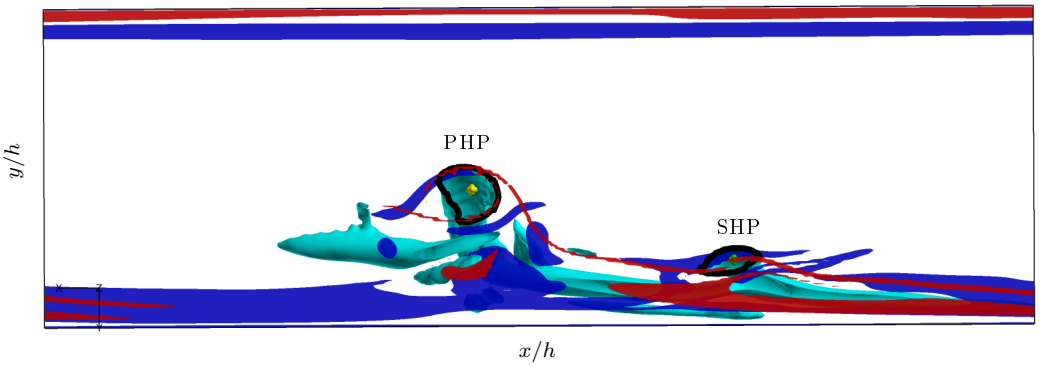

(c)

Figure 4-10: HP head visualized by an isosurface of $Q = 2\%Q_{max}$ (cyan) at the mid-span cross-section. (a) Demonstration of mid-span cross section of the channel. (b) HP heads visualized by Eulerian vortex identification methods. Yellow and green spots are PHP and SHP Γ_2 centers respectively. Black circle identifies the vortex boundary by the Q-criterion level set. (c) HP head visualized by Eulerian vortex identification methods and FTLE ridges. Yellow and green spots are PHP and SHP Γ_2 centers respectively. Black circle identifies the vortex boundary by Q-criterion level set. Negative-time and positive-FTLE ridges are plotted as red and blue curves.

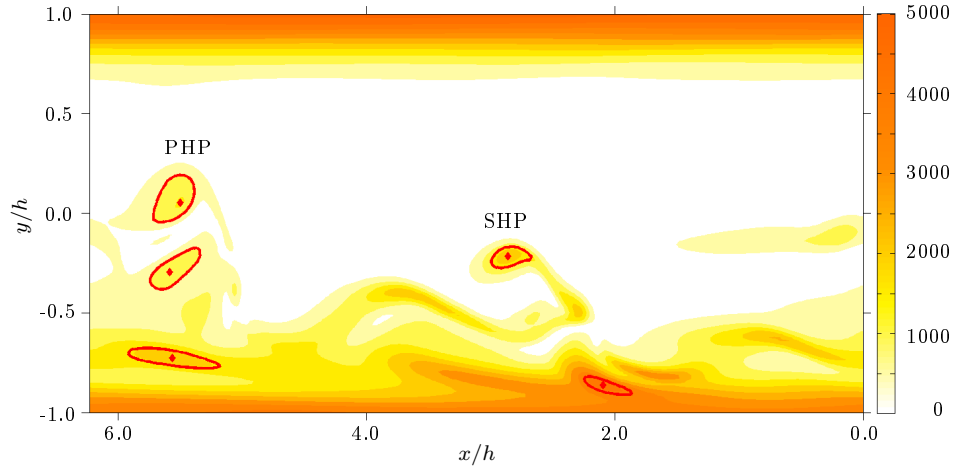

(a) HP LAVD 2D contour plot

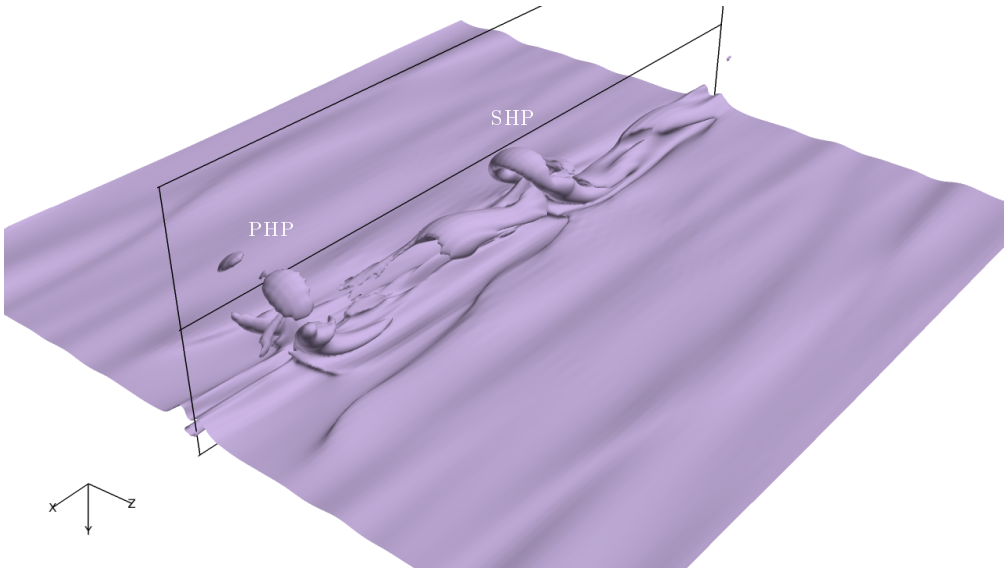

(b) HP LAVD 3D isosurface plot

Figure 4-11: HP head visualized by LAVD. (a) Identification of HP heads by LAVD 2D contour plot at the mid-span cross section of the channel. Red curves are HP head vortex boundaries by LAVD. (b) SHP head visualized by 3D LAVD iso-surface. The location of mid-span cross section plane is shown by black frame.

The SHP vortex is shown by a 3D LAVD isosurface identified from a level set of the 2D LAVD boundary around the SHP as shown in figure 4-11(b). As can be seen in the figure, the 3D LAVD isosurface of the SHP, consists of not only the SHP but also the shear layer close to the wall and partial PHP. After the formation of either PHP

or SHP vortex, the fluid particles are still entrained into or detrained from the vortex, and mix into the shear layer close to the wall. This dynamic process makes it difficult for Lagrangian methods, i.e. LAVD and FTLE, to differentiate the HP vortex from the shear layer close to the wall.

All the fluid particles within the 3D LAVD isosurface of the SHP are tracked backwards to study related problems: 1) the conditions for HP vortex auto-generation, i.e. PHP circulation, 2) origins of the SHP, 3) regions of the boundary layer directly affected by HP auto-generation.

4.3.1 Results

HP heads at the mid-span cross section of the channel are visualized by both negative- and positive-time FTLE ridges at four instants in figure 4-12. The HP vortices are moving from right to left in figure 4-12. The PHP head is identified by vortex boundary and center at $\tau^+ = 31.5$, at which instant it appears with wrapping FTLE boundaries and FTLE-saddles at intersection of both FTLE ridges, and is identified after the pFTLE separates it from the shear layer. The SHP is identified at $\tau^+ = 89.1$ by the Eulerian boundary and center, when the nFTLE boundary shows a kink (shown in figure 4-12(b)). Green et al. (2007) showed the loss of hyperbolicity along the nFTLE ridge indicating the beginning of the SHP formation, which coincides with the result of the current study.

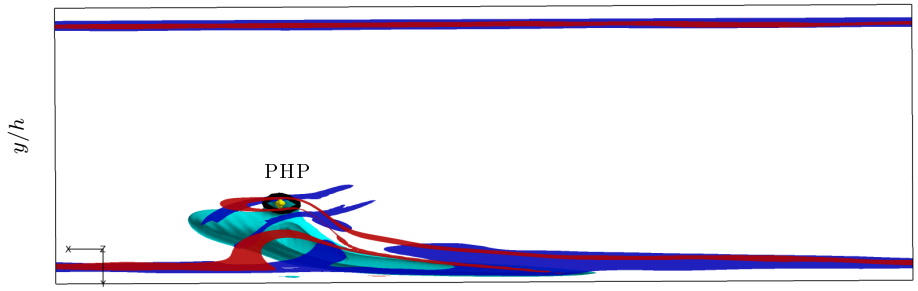

(a) $\tau^+ = 31.5$

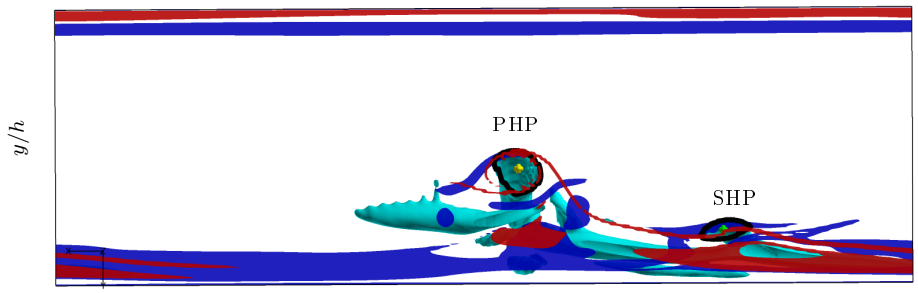

(b) $\tau^+ = 89.1$

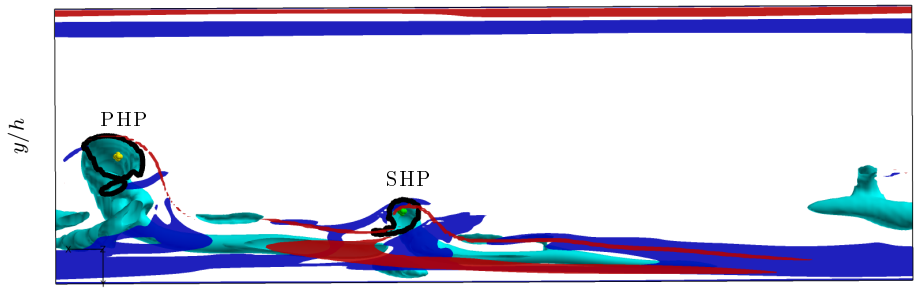

(c) $\tau^+ = 123.3$

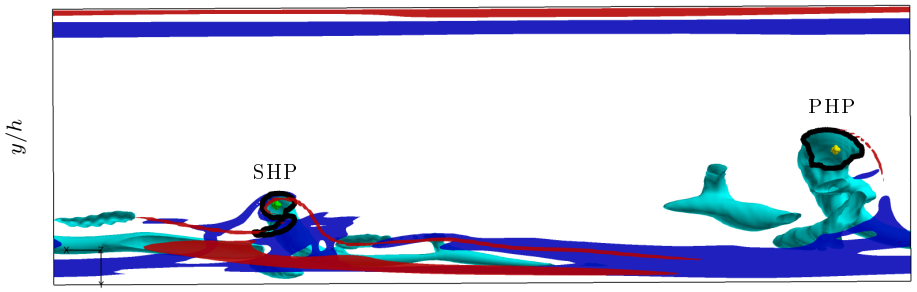

(d) $\tau^+ = 135.0$

Figure 4-12: HP head visualized by Eulerian vortex identification methods and FTLE ridges at two instants. Yellow and green spots are PHP and SHP Γ_2 centers respectively. Black circle identifies the vortex boundary by Q-criterion level set. Negative-time and positive- FTLE ridges are plotted as red and blue curves.

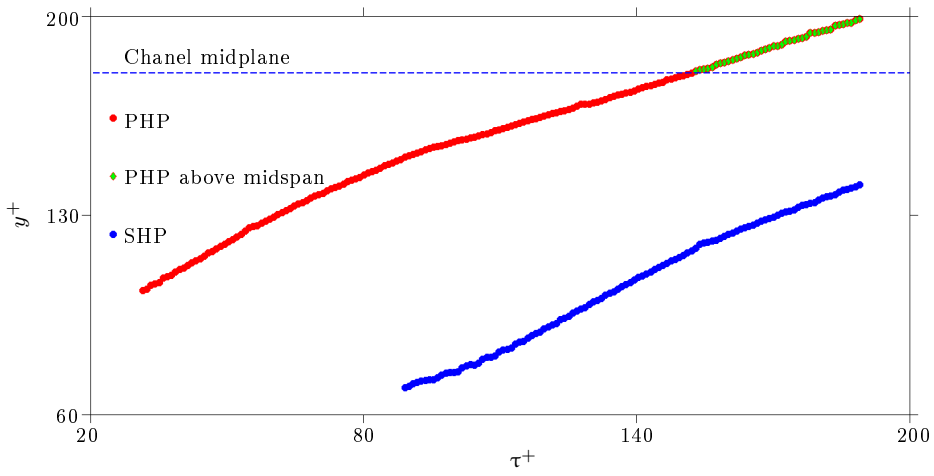

Figure 4-13: Traces of HP heads location identified by Γ_2 function centers.

In figure 4-13, both PHP and SHP heads are tracked by y^+ of their Γ_2 function center along the wall-normal direction against τ^+. In the figure, we can see that both HP heads move towards the channel midplane at a steady rate when convecting downstream. The PHP head crosses the channel midplane at $\tau^+ = 152.1$.

In figure 4-14, the dimensionless vortex area defined by Eulerian methods are tracked against τ^+. As we can see in the figure, the PHP head area increases between $\tau^+ = 31.5 - 152.1$ before it crosses the channel midplane. A more rapidly increasing trend of PHP head area can be observed close to the channel midplane. After its formation at $\tau^+ = 89.1$, the SHP head area exhibits a relatively small area compared to PHP head. The PHP and SHP head areas drop when their shapes change at $\tau^+ = 123.3$ and $\tau^+ = 135.0$ respectively (shown by black head boundary changing in figure 4-12(c) and figure 4-12(d)).

The development of both HP head circulations at mid-span are tracked against τ^+ in figure 4-15. The circulation development between $\tau^+ = 31.5 - 89.1$ shows that the PHP head circulation has a steady increasing rate. PHP head circulation reaches a plateau after SHP head formation at $\tau^+ = 89.1$, and starts decreasing while SHP head circulation increases. It can be observed that SHP heads circulation drops at $\tau^+ = 135.0$ when the head area decreases.

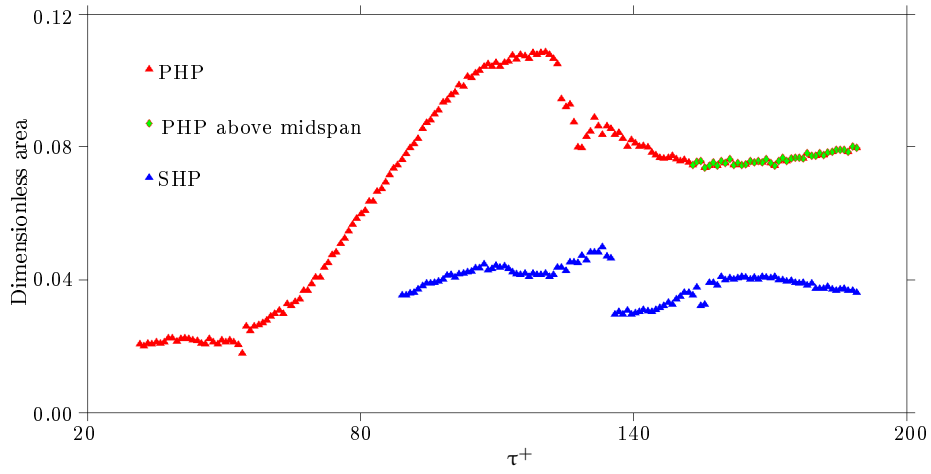

(a) HP heads area

Figure 4-14: Development of HP heads area.

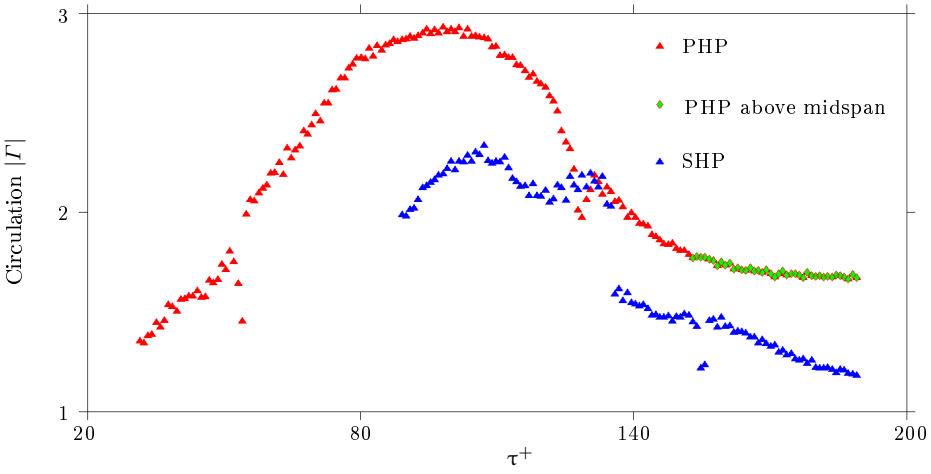

(a) HP heads circulation

Figure 4-15: Development of HP heads circulation.

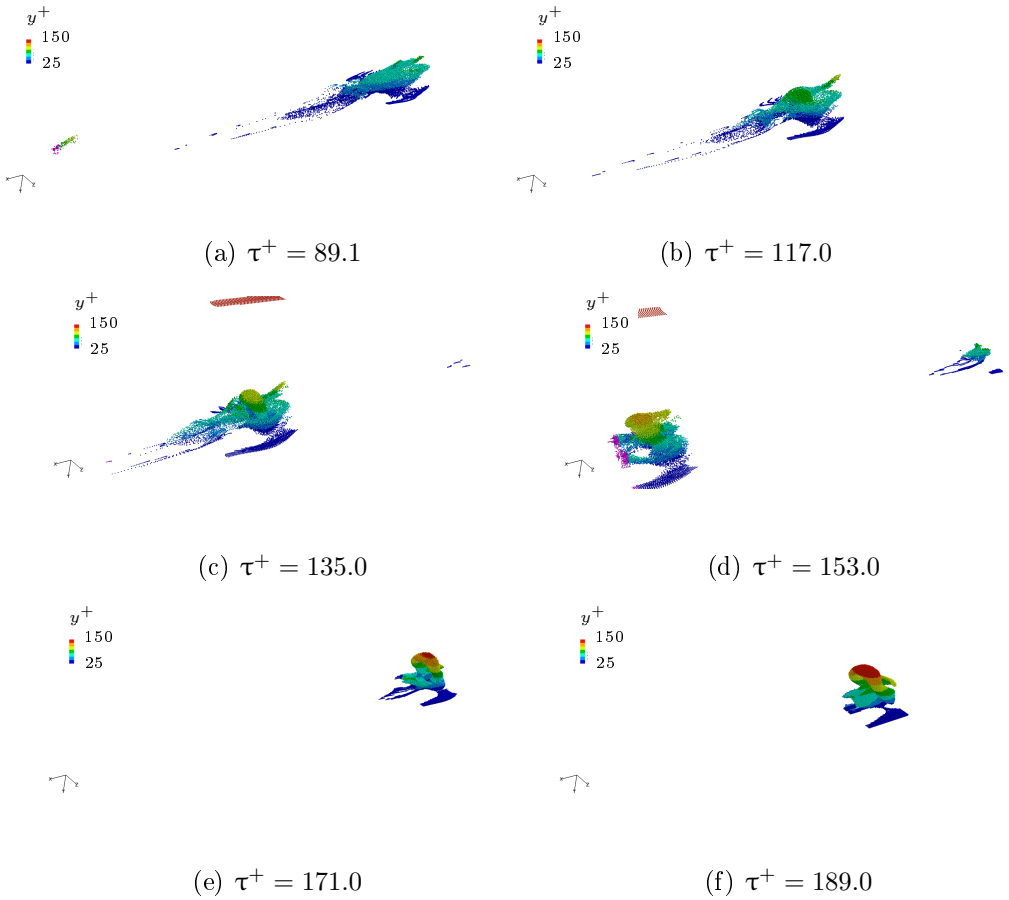

(a) $\tau^+ = 89.1$ (b) $\tau^+ = 117.0$

(c) $\tau^+ = 135.0$ (d) $\tau^+ = 153.0$

(e) $\tau^+ = 171.0$ (f) $\tau^+ = 189.0$

Figure 4-16: Material of SHP vortex identified by LAVD fluid particles colored by y^+ to aid visualization.

Figure 4-16 shows the motion of all the material belonging to the SHP identified by LAVD fluid particles. The LAVD fluid material of SHP is picked by a cut out ($2.0 < x/h < 3.0, -0.75 < y/h < 0.75$) of 3D LAVD iso-surface at $\tau^+ = 189.0$ (shown in figure 4-11) around the SHP vortex head by visual judgment. Due to the reason discussed above, it is difficult to separate the SHP vortex from the shear layer and part of the PHP vortex in the visualization of LAVD iso-surfaces, and the arbitrary cut is used here to help visualize only the SHP auto-generation process. The SHP LAVD fluid are convected backward from $\tau^+ = 189.0$ to $\tau^+ = 89.1$, and shown in figure 4-16 at six instants during the SHP auto-generation process in the forward time sequence. As can be seen in the figure, all the LAVD fluid particles in the SHP start close to the wall. The LAVD fluid belonging to the SHP head starts from $y^+ = 70$, then moves up towards the midplane to

$y^+ = 150$ in the end. It is consistent with ejection event, which is often associated with HP vortex generation. This also indicates that HP vortex formation will have effects at the wall, i.e., pressure, shear stress, etc.

The circulation, area, and wall-normal location of the PHP and SHP heads has been compared during the evolution process. A correlation between these characteristics of two HP heads is given. It is observed that the increasing strength of PHP head stops at SHP formation. A decrease in the PHP head strength while the SHP strength increases is also observed. By LAVD fluid, the origin of the SHP vortex is shown to come from the vicinity of the channel wall. Thus a strong connection between flow characteristics, i.e., pressure and shear stress and SHP is expected preceding or during the HP ejection event.

In this chapter, we applied the combination of multiple vortex detection methods into three cases of either experimental periodic or three-dimensional aperiodic flow. We found that with sufficient temporal and dimensional resolution of 3D experimental velocity data, the Lagrangian analysis by FTLE and FTLE-saddles can provide a more direct and consistent analysis with relatively less user interaction than Eulerian approaches in the research of propulsive wakes. In the 3D wall-bounded turbulent flow, the application of FTLE and FTLE-saddles provide a quantitative and qualitative investigation consistent with the traditional methods of velocity and pressure correlation, while being more robust from the small velocity field errors. In the case of 3D isolated hairpin vortex, the Lagrangian analysis of both FTLE and LAVD provide new perspectives of the SHP auto-generation process compared to the analysis only by Eulerian approaches. But we also observed that in places close to the boundary layer where the time scales can be much shorter than those in the main flow, as well as in the HP vortex where it experiences strong entrainment and detrainment, the Lagrangian approaches perform poorly, as it is difficult to separate the HP vortex and shear layer for in depth research.

Chapter 5

Conclusion and outlook

This thesis advances the state of the art regarding vortex identification and tracking in the vortex forming and shedding flows of flapping flight by a detailed study of a canonical case, the leading edge vortex (LEV) shedding from a flat plate with 45° pitch-up maneuver. The canonical case study revealed the advantages of the combination of multiple Eulerian and Lagrangian vortex detection approaches, i.e. FTLE, Geodesic LCS, LAVD, and Q-criterion, etc., in the vortex dynamics analysis. By identifying and quantifying the LEV dynamics during its evolution, and by analyzing its shedding phenomenon and the influence on the plate lift fluctuation, this study helps to provide future refinement of aerodynamic models incorporating vortex shedding. The vortex dominated flow in the study is in many ways analogous to the flight of natural flyers, and is relevant to the aerodynamics of bio-inspired MAVs incorporating unsteady flapping flight. The knowledge produced by this study thus has the potential to impact the future design of such MAVs.

5.1 Conclusions

The vortex detection methods used in this thesis allow us to simultaneously consider multiple vortices present in a given data set, and they reveal complex vortex dynamics. This allows us to track and evaluate the vortex dynamics in both time and space, such as formation, attachment, growth, shedding, and convection, etc. Combined with the

optimal vortex formation concept and vortex shedding mechanism, the vortex detection methods enable us to investigate the vortex shedding mechanism and its correlation with the fluctuation of lift on the plate.

During the pitch-up motion of the flat plate, there is formation and shedding of a large scale LEV and a trailing edge vortex (TEV, induced upon LEV shedding). FTLE-saddles and λ-saddles on the boundary of the LEV are tracked to study the LEV shedding from the plate and the intermittent feeding of the LEV by the shear layer. The shedding time of FTLE-saddle I at $\hat{T} = 4.5$ indicates the detachment of the LEV, matches with the formation number $N = 4.5$, and correlates with the first peak of lift after the plate motion stopped. The shedding time of FTLE-saddle III at $\hat{T} = 7.1$ correlates with the LAVD-defined fluid circulation peaks and the last marked decreases in the plate lift (associated with the LEV). The FTLE-saddles around the LEV match with the shedding location identified by VSM, which attributes the vortex shedding to influence of stream-wise pressure gradient. As discussed in chapter 3, λ-saddle is a more recent approach, but there is a numerical error in its resulting saddle location induced by the flow map in its algorithm compared to FTLE-saddle. In contrast, the FTLE-saddle by the standard method provides a solution with the minimum error, preventing the discrepancy between the physical saddle and numerical saddle to be amplified in the calculation.

The exploration of vortex detection methods is extended to three other cases: a 2D experimental data set of a pitching plate, a fully developed turbulent channel flow and an isolated hairpin vortex through its evolution process. We found that the trajectory and phenomenological evolution of vortices could be determined by tracking FTLE-saddles and visualizing LAVD-defined fluid in these cases. Using the vortex detection approaches to track the vortices yielded an objective point in space tied to their location, which enabled the implementation of automatic tracking algorithms. Automatic tracking of vortices in moderate Re flows dominated by large scale structures allows for the robust application of quantitative analysis techniques and criteria to determine the behavior of structures. This will be particularly useful in studying the unsteady aerodynamic applications of birds and large insects, which primarily fly at $Re = 10^2 - 10^4$ (Shyy et al., 2008; Ol et al., 2009). It is worth noting that in turbulent flows or other flows with an

interacting range of length and time scales, users need to carefully consider the interplay between the spectrum of time scales of the data set and the integration time, and carefully choose an integration time of the vortex criteria based on the relevant time scale. As shown in Chapter 4, there is still a good deal of information and flow description available using these methods in the more complex flows, but implementation of the method and interpretation of the results must be more careful.

5.2 Recommendations for Future Work

With the current body of work detecting and analyzing the LEV shedding with its correlation to the plate lift fluctuation in a 2D canonical case, the next step in the current research would be to extend the study into more complicated flapping flight with either the pitching, heaving or surging motions, or a combination of them. Flow features that emerge in the pitch-up motion have been described in detail, and investigating the effect of the continuous motions on the vortex shedding and the aerodynamic forces would be an interesting problem to explore.

Use of the Lagrangian FTLE with experimental data requires both temporal and dimensional support in the data. While it is not uncommon to use a trajectory integration timestep during particle trajectory calculation that is smaller than the time between subsequent velocity data sets, the temporal resolution of the data must be sufficient so that interpolation techniques adequately recreate intermediate velocity fields when it is necessary. For inherently three-dimensional flows, a single plane of data, even if it contains all three velocity components, is not sufficient to generate an accurate Cauchy-Green deformation tensor and FTLE field. The wake structure of a 2D flow and a 3D flow is essentially different, and a 2D plane flow would not represent the real 3D wake structure as 3D instabilities develop. In particular, vortex structures that are parallel to the data plane, such that the vortex-induced velocity will be in and out of the plane, will not be captured. In those cases where it is known ahead of time that the structures of interest are mainly perpendicular to the plane in which data is acquired, the FTLE calculation will capture the majority of the structures in the plane. The further application of the vortex

detection approaches in 3D data is necessary to broad and validate their application to more general cases.

Based on the statistical result in the turbulent channel flow and the study on the hairpin vortex evolution in this thesis, the next step can be a 3D implementation of the vortex identification methods in turbulent boundary layers. When applying the Lagrangian methods FTLE and LAVD for vortex identification and tracking in turbulent boundary layer, the high shear stress close to the boundary, and intense entrainment and detrainment of fluid material into or away from the the Lagrangian coherent structure make it difficult to differentiate Lagrangian coherent structures from the shear layer close to the boundary. More correlations between the hairpin vortex dynamics and the complex, random, multi-scaled turbulent motion, as well as the shear stress and drag on the boundary will be the next step in the current research. A united picture of the turbulent flow could be significantly advanced.

Appendices

Appendix A

Code Used

MATLAB and Fortran 90 were used extensively for all the analysis techniques, Lagrangian coherent structure analysis, such as FTLE, FTLE-saddle, Geodesic LCS, λ-saddle, LAVD. Fieldview was used to generate wake visualization images. All codes used are available on http://greenfluids.syr.edu/, and a list of the files and a short description for each is included below.

A.1 Fortran 90 codes

1. intprog.f90: Top-level code to integrate trajectories and λ, and calculate Cauchy-Green strain tensor eigenvector and eigenvalue, FTLE, LAVD.

2. grid.f90: Read in input parameters and set up the calculation grid.

3. inout.f90: All input and output subroutines.

4. ftlecalc.f90: Particle, λ integration, Cauchy-Green strain tensor eigenvector and eigenvalue, FTLE, LAVD calculation, and velocity field interpolation.

5. Makefile: File used to compile all modules at once.

6. input.inp: Input parameters, usually located in a subfolder.

A.2 MATLAB codes

1. ftle_saddle.m: Calculates FTLE-saddle locations for all cases.

2. lambda_saddle.m: Calculates λ-saddle locations for all cases.

A.3 Fieldview code

1. Image_General.fvx Generate images with the same formatting for a number of data files.

Bibliography

Abel-John Lothar Lamond Buchner. Dynamic stall: stability and evolution at transitional Reynolds numbers. PhD thesis, Monash University. Faculty of Engineering. Department on Mechanical and Aerospace Engineering, 2016.

Nipun Arora, Amit Gupta, Sanjeev Sanghi, Hikaru Aono, and Wei Shyy. Lift-drag and flow structures associated with the "clap and fling" motion. Physics of Fluids (1994-present), 26(7):071906, 2014.

Morteza Gharib, Edmond Rambod, and Karim Shariff. A universal time scale for vortex ring formation. Journal of Fluid Mechanics, 360:121–140, 1998.

ME Boghosian and KW Cassel. On the origins of vortex shedding in two-dimensional incompressible flows. Theoretical and Computational Fluid Dynamics, pages 1–17, 2016.

Karen Mulleners and Markus Raffel. The onset of dynamic stall revisited. Experiments in fluids, 52(3):779–793, 2012.

Jeff D Eldredge. Numerical simulation of the fluid dynamics of 2d rigid body motion with the vortex particle method. J. Comput. Phys., 221:626–648, 2007.

Melissa A. Green, Clarence W. Rowley, and Alexander J. Smits. The unsteady three-dimensional wake produced by a trapezoidal pitching panel. Journal of Fluid Mechanics, 685:117–145, 2011.

John Kim and Fazle Hussain. Propagation velocity of perturbations in turbulent channel flow. Physics of Fluids A, 5(3):695–706, 1993.

Jigen Zhou, Ronald J Adrian, S Balachandar, and TM Kendall. Mechanisms for generating coherent packets of hairpin vortices in channel flow. Journal of Fluid Mechanics, 387:353–396, 1999.

Rafał Zbikowski. Flapping wing technology. In European Military Rotorcraft Symposium, Shrivenham, UK, March, pages 1–7, 2000.

Rafal Żbikowski. On aerodynamic modelling of an insect–like flapping wing in hover for micro air vehicles. Philosophical Transactions of the Royal Society of London A: Mathematical, Physical and Engineering Sciences, 360(1791):273–290, 2002a.

Charles Pitt Ford and Holger Babinsky. Lift and the leading-edge vortex. Journal of Fluid Mechanics, 720:280–313, 2013. ISSN 1469-7645. doi: 10.1017/jfm.2013.28.

Michael H Dickinson and Karl G Gotz. Unsteady aerodynamic performance of model wings at low reynolds numbers. The Journal of Experimental Biology, 174(1):45–64, 1993.

Charles P Ellington, Coen Van Den Berg, Alexander P Willmott, and Adrian LR Thomas. Leading-edge vortices in insect flight. Nature, 384(6610):626, 1996.

Z Jane Wang. Dissecting insect flight. Annu. Rev. Fluid Mech., 37:183–210, 2005.

Jeff D Eldredge, Chengjie Wang, and MV Ol. A computational study of a canonical pitch-up, pitch-down wing maneuver. AIAA paper, 3687:2009, 2009.

Thomas J Mueller. Fixed and flapping wing aerodynamics for micro air vehicle applications, volume 195. AIAA, 2001.

Darryll J Pines and Felipe Bohorquez. Challenges facing future micro-air-vehicle development. Journal of aircraft, 43(2):290–305, 2006.

Wei Shyy, Hikaru Aono, Satish Kumar Chimakurthi, Pat Trizila, C-K Kang, Carlos ES Cesnik, and Hao Liu. Recent progress in flapping wing aerodynamics and aeroelasticity. Progress in Aerospace Sciences, 46(7):284–327, 2010.

Wei Shyy, Y Lian, J Tang, H Liu, P Trizila, B Stanford, L Bernal, C Cesnik, P Friedmann, and P Ifju. Computational aerodynamics of low reynolds number plunging, pitching and flexible wings for mav applications. Acta Mechanica Sinica, 24(4):351–373, 2008.

Umberto Pesavento and Z Jane Wang. Flapping wing flight can save aerodynamic power compared to steady flight. Physical review letters, 103(11):118102, 2009.

Sutthiphong Srigrarom and Woei-Leong Chan. Ornithopter type flapping wings for autonomous micro air vehicles. Aerospace, 2(2):235–278, 2015.

James M Birch and Michael H Dickinson. Spanwise flow and the attachment of the leading-edge vortex on insect wings. Nature, 412(6848):729–733, 2001.

Sanjay P Sane. The aerodynamics of insect flight. The journal of experimental Biology, 206(23):4191–4208, 2003.

Rafal Żbikowski. On aerodynamic modelling of an insect–like flapping wing in hover for micro air vehicles. Philosophical Transactions of the Royal Society of London A: Mathematical, Physical and Engineering Sciences, 360(1791):273–290, 2002b.

J Videler, John, EJ Stamhuis, and GDE Povel. Leading-edge vortex lifts swifts. Science, 306(5703):1960–1962, 2004.

Delyle T. Polet, David E. Rival, and Gabriel D. Weymouth. Unsteady dynamics of rapid perching manoeuvres. Journal of Fluid Mechanics, 767:323–341, 2015.

D. T. Polet and D. E. Rival. Rapid area change in pitch-up manoeuvres of small perching birds. Bioinspiration & biomimetics, 10(6):066004, 2015.

William J McCroskey. Unsteady airfoils. Annual review of fluid mechanics, 14(1):285–311, 1982.

A Smith. Vortex models for the control of stall. PhD thesis, Boston University, 2005.

James M Akkala, Azar Eslam Panah, and James HJ Buchholz. Vortex dynamics and performance of flexible and rigid plunging airfoils. Journal of Fluids and Structures, 54:103–121, 2015.

Michael V Ol, Luis Bernal, Chang-Kwon Kang, and Wei Shyy. Shallow and deep dynamic stall for flapping low reynolds number airfoils. Experiments in Fluids, 46(5):883–901, 2009.

Theodore Theodorsen and WH Mutchler. General theory of aerodynamic instability and the mechanism of flutter. Technical report, NASA Document, 1935.

Herbert Wagner. Über die entstehung des dynamischen auftriebes von tragflügeln. ZAMM-Journal of Applied Mathematics and Mechanics/Zeitschrift für Angewandte Mathematik und Mechanik, 5(1):17–35, 1925.

Herbert G Küssner. Zusammenfassender bericht über den instationären auftrieb von flügeln. Luftfahrtforschung, 13(12):410–424, 1936.

TH Von Kármán. Airfoil theory for non-uniform motion. Journal of the Aeronautical Sciences, 5(10):379–390, 1938.

MFM Osborne. Aerodynamics of flapping flight with application to insects. Journal of Experimental Biology, 28(2):221–245, 1951.

JWS Pringle. Locomotion: flight. The physiology of insecta, 2:283–329, 1965.

Torkel Weis-Fogh. Energetics of hovering flight in hummingbirds and in drosophila. Journal of Experimental Biology, 56(1):79–104, 1972.

Torkel Weis-Fogh. Quick estimates of flight fitness in hovering animals, including novel mechanisms for lift production. Journal of Experimental Biology, 59(1):169–230, 1973.

MJ Lighthill. On the weis-fogh mechanism of lift generation. Journal of Fluid Mechanics, 60(01):1–17, 1973.

Tony Maxworthy. Experiments on the weis-fogh mechanism of lift generation by insects in hovering flight. part 1. dynamics of the âĂŸflingâĂŹ. Journal of Fluid Mechanics, 93(01):47–63, 1979.

CP Ellington. The aerodynamics of hovering insect flight. i. the quasi-steady analysis. Philosophical Transactions of the Royal Society of London B: Biological Sciences, 305 (1122):1–15, 1984a.

CP Ellington. The aerodynamics of hovering insect flight. iii. kinematics. Philosophical Transactions of the Royal Society of London B: Biological Sciences, 305(1122):41–78, 1984b.

CP Ellington. The aerodynamics of hovering insect flight. iv. aeorodynamic mechanisms. Philosophical Transactions of the Royal Society B: Biological Sciences, 305(1122):79–113, 1984c.

CP Ellington. The aerodynamics of hovering insect flight. vi. lift and power requirements. Philosophical Transactions of the Royal Society of London B: Biological Sciences, 305 (1122):145–181, 1984d.

Linda J Martin and Peter W Carpenter. Flow-visualization experiments on butterflies in simulated gliding flight. Fortschritte der Zoologie, 24(2-3):308–316, 1977.

William J McCroskey. The phenomenon of dynamic stall. Technical report, DTIC Document, 1981.

Peter Freymuth. Thrust generation by an airfoil in hover modes. Experiments in Fluids, 9(1):17–24, 1990.

William C Reynolds and LW Carr. Review of unsteady, driven, separated flows. publisher not identified, 1985.

Kazuo Ohmi, Madeleine Coutanceau, Ta Phuoc Loc, and Annie Dulieu. Vortex formation around an oscillating and translating airfoil at large incidences. Journal of Fluid Mechanics, 211:37–60, 1990.

Kazuo Ohmi, Madeleine Coutanceau, Olivier Daube, and Ta Phuoc Loc. Further experiments on vortex formation around an oscillating and translating airfoil at large incidences. Journal of Fluid Mechanics, 225:607–630, 1991.

MS Triantafyllou, GS Triantafyllou, and R Gopalkrishnan. Wake mechanics for thrust generation in oscillating foils. Physics of Fluids A: Fluid Dynamics, 3(12):2835–2837, 1991.

George S Triantafyllou, MS Triantafyllou, and MA Grosenbaugh. Optimal thrust development in oscillating foils with application to fish propulsion. Journal of Fluids and Structures, 7(2):205–224, 1993.

AK Brodsky. Vortex formation in the tethered flight of the peacock butterfly inachis io l.(lepidoptera, nymphalidae) and some aspects of insect flight evolution. Journal of Experimental Biology, 161(1):77–95, 1991.

Dmitry L Grodnitsky and Pahvel P Morozov. Flow visualization experiments on tethered flying green lacewings chrysopa dasyptera. Journal of experimental biology, 169(1): 143–163, 1992.

Dmitry L Grodnitsky and Pahvel P Morozov. Vortex formation during tethered flight of functionally and morphologically two-winged insects, including evolutionary considerations on insect flight. Journal of Experimental Biology, 182(1):11–40, 1993.

KD Jones, CM Dohring, and MF Platzer. Wake structures behind plunging airfoils: a comparison of numerical and experimental results. AIAA paper, 78:1996, 1996.

K Jones, M Platzer, K Jones, and M Platzer. Numerical computation of flapping-wing propulsion and power extraction. In 35th Aerospace Sciences Meeting and Exhibit, page 826, 1997.

K Jones and M Platzer. An experimental and numerical investigation of flapping-wing propulsion. In 37th Aerospace Sciences Meeting and Exhibit, page 995, 1999.

K Jones, S Duggan, and M Platzer. Flapping-wing propulsion for a micro air vehicle. In 39th Aerospace Sciences Meeting and Exhibit, page 126, 2000.

AR Jones and H Babinsky. Reynolds number effects on leading edge vortex development on a waving wing. Experiments in fluids, 51(1):197–210, 2011.

Alexander P Willmott, Charles P Ellington, and Adrian LR Thomas. Flow visualization and unsteady aerodynamics in the flight of the hawkmoth, manduca sexta. Philosophical Transactions of the Royal Society of London B: Biological Sciences, 352 (1351):303–316, 1997.

Coen Van Den Berg and Charles P Ellington. The three–dimensional leading–edge vortex of a âĂŸhoveringâĂŹmodel hawkmoth. Philosophical Transactions of the Royal Society of London B: Biological Sciences, 352(1351):329–340, 1997a.

Coen Van Den Berg and Charles P Ellington. The vortex wake of a âĂŸhoveringâĂŹ-model hawkmoth. Philosophical Transactions of the Royal Society of London B: Biological Sciences, 352(1351):317–328, 1997b.

Hao Liu, Charles P Ellington, Keiji Kawachi, Coen Van Den Berg, and Alexander P Willmott. A computational fluid dynamic study of hawkmoth hovering. The journal of experimental biology, 201(4):461–477, 1998.

JM Anderson, K Streitlien, DS Barrett, and MS Triantafyllou. Oscillating foils of high propulsive efficiency. Journal of Fluid Mechanics, 360:41–72, 1998.

Michael H Dickinson, Fritz-Olaf Lehmann, and Sanjay P Sane. Wing rotation and the aerodynamic basis of insect flight. Science, 284(5422):1954–1960, 1999.

Adrian LR Thomas, Graham K Taylor, Robert B Srygley, Robert L Nudds, and Richard J Bomphrey. Dragonfly flight: free-flight and tethered flow visualizations reveal a diverse array of unsteady lift-generating mechanisms, controlled primarily via angle of attack. Journal of Experimental Biology, 207(24):4299–4323, 2004.

Richard J Bomphrey, Nicholas J Lawson, Nicholas J Harding, Graham K Taylor, and Adrian LR Thomas. The aerodynamics of manduca sexta: digital particle image velocimetry analysis of the leading-edge vortex. Journal of Experimental Biology, 208 (6):1079–1094, 2005.

Richard J Bomphrey, Nicholas J Lawson, Graham K Taylor, and Adrian LR Thomas. Application of digital particle image velocimetry to insect aerodynamics: measurement of the leading-edge vortex and near wake of a hawkmoth. Experiments in Fluids, 40 (4):546, 2006.

C Poelma, WB Dickson, and MH Dickinson. Time-resolved reconstruction of the full velocity field around a dynamically-scaled flapping wing. Experiments in Fluids, 41 (2):213–225, 2006.

Yeon Sik Baik, Luis Bernal, Wei Shyy, and Michael Ol. Unsteady force generation and vortex dynamics of pitching and plunging flat plates at low Reynolds number. PhD thesis, University of Michigan, 2011.

Z Jane Wang. Two dimensional mechanism for insect hovering. Physical review letters, 85(10):2216, 2000a.

Z Jane Wang. Using drag to hover. arXiv preprint physics/0304069, 2003.

DI Pullin and Z Jane Wang. Unsteady forces on an accelerating plate and application to hovering insect flight. Journal of Fluid Mechanics, 509:1–21, 2004.

Marvin A Jones. The separated flow of an inviscid fluid around a moving flat plate. Journal of Fluid Mechanics, 496:405, 2003.

Patrick Zdunich. A Discrete Vortex Model of Unsteady Separated Flow About a Thin Airfoil For Application to Hovering Flapping-Wing Flight. PhD thesis, University of Toronto, 2003.

SA Ansari, R Żbikowski, and K Knowles. Non-linear unsteady aerodynamic model for insect-like flapping wings in the hover. part 1: methodology and analysis. Proceedings of the Institution of Mechanical Engineers, Part G: Journal of Aerospace Engineering, 220(2):61–83, 2006.

Hikaru Aono, Wei Shyy, and Hao Liu. Near wake vortex dynamics of a hovering hawkmoth. Acta Mechanica Sinica, 25(1):23–36, 2009.

T Jardin and L David. Coriolis effects enhance lift on revolving wings. Physical review. E, Statistical, nonlinear, and soft matter physics, 91(3):031001, 2015. ISSN 1539-3755. doi: 10.1103/PhysRevE.91.031001.

AR Jones and H Babinsky. Unsteady lift generation on rotating wings at low reynolds numbers. stroke, 8:9, 2010.

Z Wang. Vortex shedding and frequency selection in flapping flight. Journal of Fluid Mechanics, 410:323–341, 2000b.

Z. R. Carr, C. Chen, and M. J. Ringuette. Finite-span rotating wings: three-dimensional vortex formation and variations with aspect ratio. Experiments in fluids, 54(2):1–26, 2013.

Alexander Widmann and Cameron Tropea. Reynolds number influence on the formation of vortical structures on a pitching flat plate. Interface Focus, 7(1):20160079, 2017.

James HJ Buchholz, Melissa A Green, and Alexander J Smits. Scaling the circulation shed by a pitching panel. Journal of Fluid Mechanics, 688:591–601, 2011.

Chengjie Wang and Jeff D Eldredge. Low-order phenomenological modeling of leading-edge vortex formation. Theoretical and Computational Fluid Dynamics, pages 1–22, 2013.

Craig J Wojcik and James HJ Buchholz. Parameter variation and the leading-edge vortex of a rotating flat plate. AIAA journal, 52(2):348–357, 2014.

Moshe Rosenfeld, Edmond Rambod, and Morteza Gharib. Circulation and formation number of laminar vortex rings. Journal of Fluid Mechanics, 376:297–318, 1998.

U Dallmann, ThGebing Herberg, W Su, and H Zhang. Flow field diagnostics-topological flow changes and spatio-temporal flow structure. In 33rd Aerospace Sciences Meeting and Exhibit, page 791, 1995.

Vassilios Theofilis, Stefan Hein, and Uwe Dallmann. On the origins of unsteadiness and three-dimensionality in a laminar separation bubble. Philosophical Transactions of the Royal Society of London A: Mathematical, Physical and Engineering Sciences, 358 (1777):3229–3246, 2000.

Matthieu Marquillie and UWE Ehrenstein. On the onset of nonlinear oscillations in a separating boundary-layer flow. Journal of Fluid Mechanics, 490:169–188, 2003.

AV Obabko and KW Cassel. Navier–stokes solutions of unsteady separation induced by a vortex. Journal of Fluid Mechanics, 465:99–130, 2002.

Daehyun Wee, Tongxun Yi, Anuradha Annaswamy, and Ahmed F Ghoniem. Self-sustained oscillations and vortex shedding in backward-facing step flows: Simulation and linear instability analysis. Physics of Fluids, 16(9):3361–3373, 2004.

William Thomson Baron Kelvin. Vortex statics. publisher not identified, 1880.

T Brooke Benjamin. The alliance of practical and analytical insights into the nonlinear problems of fluid mechanics. In Applications of methods of functional analysis to problems in mechanics, pages 8–29. Springer, 1976.

TS Pottebaum and M Gharib. The pinch-off process in a starting buoyant plume. Experiments in fluids, 37(1):87–94, 2004.

Paul S Krueger and Morteza Gharib. The significance of vortex ring formation to the impulse and thrust of a starting jet. Physics of Fluids, 15(5):1271–1281, 2003.

David Jeon and Morteza Gharib. On the relationship between the vortex formation process and cylinder wake vortex patterns. Journal of Fluid Mechanics, 519:161–181, 2004.

John O Dabiri and Morteza Gharib. Starting flow through nozzles with temporally variable exit diameter. Journal of Fluid Mechanics, 538:111–136, 2005.

Michele Milano and Morteza Gharib. Uncovering the physics of flapping flat plates with artificial evolution. Journal of Fluid Mechanics, 534:403–409, 2005.

Michele Milano and Petros Koumoutsakos. A clustering genetic algorithm for cylinder drag optimization. Journal of Computational Physics, 175(1):79–107, 2002.

Matthew J Ringuette, Michele Milano, and Morteza Gharib. Role of the tip vortex in the force generation of low-aspect-ratio normal flat plates. Journal of Fluid Mechanics, 581:453–468, 2007.

John O Dabiri. Optimal vortex formation as a unifying principle in biological propulsion. Annual review of fluid mechanics, 41:17–33, 2009.

David Rival, Tim Prangemeier, and Cameron Tropea. The influence of airfoil kinematics on the formation of leading-edge vortices in bio-inspired flight. Experiments in fluids, 46(5):823–833, 2009.

Kyohei Onoue and Kenneth S. Breuer. Vortex formation and shedding from a cyber-physical pitching plate. Journal of Fluid Mechanics, 793:229–247, 2016. ISSN 0022-1120, 1469-7645. doi: 10.1017/jfm.2016.134.

Wolfgang Cherdron, Franz Durst, and James H Whitelaw. Asymmetric flows and instabilities in symmetric ducts with sudden expansions. Journal of Fluid Mechanics, 84 (01):13–31, 1978.

Laura L Pauley, Parviz Moin, and William C Reynolds. The structure of two-dimensional separation. Journal of Fluid Mechanics, 220:397–411, 1990.

Yeng-Yung Tsui, Chia-Kang Wang, et al. Calculation of laminar separated flow in symmetric two-dimensional diffusers. Jounal of fluids engineering, 117:612–616, 1995.

Lambros Kaiktsis, George Em Karniadakis, and Steven A Orszag. Unsteadiness and convective instabilities in two-dimensional flow over a backward-facing step. Journal of Fluid Mechanics, 321:157–187, 1996.

R Mittal, SP Simmons, and F Najjar. Numerical study of pulsatile flow in a constricted channel. Journal of Fluid Mechanics, 485:337–378, 2003.

Michael Edward Boghosian. Flow in partially constricted planar channels-origins of vortex shedding and global stability of Navier–Stokes solutions. Illinois Institute of Technology, 2011.

ME Boghosian and KW Cassel. A pressure-gradient mechanism for vortex shedding in constricted channels. Physics of Fluids, 25(12):123603, 2013.

JM Lawson and JR Dawson. The formation of turbulent vortex rings by synthetic jets. Physics of Fluids, 25(10):105113, 2013.

Adam C. DeVoria and Matthew J. Ringuette. Vortex formation and saturation for low-aspect-ratio rotating flat-plate fins. Experiments in fluids, 52(2):441–462, 2012.

JG Leishman and TS Beddoes. A semi-empirical model for dynamic stall. Journal of the American Helicopter society, 34(3):3–17, 1989.

Peter G Wilby. The development of rotor airfoil testing in the uk. Journal of the American Helicopter Society, 46(3):210–220, 2001.

W Sheng, RA McD Galbraith, and FN Coton. A new stall-onset criterion for low speed dynamic-stall. Journal of Solar Energy Engineering, 128(4):461–471, 2006.

Steven Brunton and Clarence Rowley. Modeling the unsteady aerodynamic forces on small-scale wings. AIAA Paper, 1127:2009, 2009a.

Yangzi Huang and Melissa A Green. Comparing leading and trailing edge vortex circulation history with vortex identification and tracking methods. In 54th AIAA Aerospace Sciences Meeting, page 2082, 2016.

Jinhee Jeong and Fazle Hussain. On the identification of a vortex. Journal of fluid mechanics, 285:69–94, 1995.

Pinaki Chakraborty, S Balachandar, and Ronald J Adrian. On the relationships between local vortex identification schemes. Journal of Fluid Mechanics, 535:189–214, 2005.

Frits H Post, Benjamin Vrolijk, Helwig Hauser, Robert S Laramee, and Helmut Doleisch. The state of the art in flow visualisation: Feature extraction and tracking. In Computer Graphics Forum, volume 22, pages 775–792. Wiley Online Library, 2003.

Tobias Salzbrunn, Christoph Garth, Gerik Scheuermann, and Joerg Meyer. Pathline predicates and unsteady flow structures. The Visual Computer, 24(12):1039–1051, 2008.

Armin Pobitzer, Ronald Peikert, Raphael Fuchs, Benjamin Schindler, Alexander Kuhn, Holger Theisel, Krešimir Matkovic, and Helwig Hauser. On the way towards topology-based visualization of unsteady flow-the state of the art. H. und E. Reinhard (Hrsg.), Eurographics, 2010.

Armin Pobitzer, Ronald Peikert, Raphael Fuchs, Benjamin Schindler, Alexander Kuhn, Holger Theisel, Krešimir Matković, and Helwig Hauser. The state of the art in topology-based visualization of unsteady flow. In Computer Graphics Forum, volume 30, pages 1789–1811. Wiley Online Library, 2011.

James C McWilliams. The emergence of isolated coherent vortices in turbulent flow. Journal of Fluid Mechanics, 146:21–43, 1984.

AKMF Hussain. Coherent structures and turbulence. Journal of Fluid Mechanics, 173 (303-356):125, 1986.

Tobias Günther, Maik Schulze, and Holger Theisel. Rotation invariant vortices for flow visualization. IEEE transactions on visualization and computer graphics, 22(1):817–826, 2016.

Julian CR Hunt, Alan A Wray, and Parviz Moin. Eddies, streams, and convergence zones in turbulent flows. Technical report, NASA Document, 1988.

MS Chong, A Eo Perry, and BJ Cantwell. A general classification of three-dimensional flow fields. Physics of Fluids A: Fluid Dynamics (1989-1993), 2(5):765–777, 1990.

Yves Dubief and Franck Delcayre. On coherent-vortex identification in turbulence. Journal of turbulence, 1(1):011–011, 2000.

R Cucitore, M Quadrio, and A Baron. On the effectiveness and limitations of local criteria for the identification of a vortex. European Journal of Mechanics-B/Fluids, 18 (2):261–282, 1999.

Laurent Graftieaux, Marc Michard, and Nathalie Grosjean. Combining piv, pod and vortex identification algorithms for the study of unsteady turbulent swirling flows. Measurement Science and Technology, 12(9):1422, 2001.

Akira Okubo. Horizontal dispersion of floatable particles in the vicinity of velocity singularities such as convergences. In Deep sea research and oceanographic abstracts, volume 17, pages 445–454. Elsevier, 1970.

John Weiss. The dynamics of enstrophy transfer in two-dimensional hydrodynamics. Physica D: Nonlinear Phenomena, 48(2-3):273–294, 1991.

George Haller. An objective definition of a vortex. Journal of Fluid Mechanics, 525:1–26, 2005.

Arganthaël Berson, Marc Michard, and Philippe Blanc-Benon. Vortex identification and tracking in unsteady flows. Comptes Rendus Mécanique, 337(2):61–67, 2009.

Turgut O Yilmaz and D Rockwell. Flow structure on finite-span wings due to pitch-up motion. Journal of Fluid Mechanics, 691:518–545, 2012.

Václav Kolář. Vortex identification: New requirements and limitations. International journal of heat and fluid flow, 28(4):638–652, 2007.

Morton E Gurtin. An introduction to continuum mechanics, volume 158. Academic press, 1982.

George Haller. Lagrangian coherent structures. Annual Review of Fluid Mechanics, 47: 137–162, 2015.

Thomas Peacock and John Dabiri. Introduction to focus issue: Lagrangian coherent structures, 2010.

T Peacock, G Froyland, and G Haller. Introduction to focus issue: Objective detection of coherent structures, 2015.

Shawn C Shadden. Lagrangian coherent structures. Transport and Mixing in Laminar Flows: From Microfluidics to Oceanic Currents, pages 59–89, 2011.

Michael R Allshouse and Thomas Peacock. Lagrangian based methods for coherent structure detection. Chaos: An Interdisciplinary Journal of Nonlinear Science, 25(9): 097617, 2015.

George Haller. Distinguished material surfaces and coherent structures in 3d fluid flows. Physica D, 149:248–277, 2001.

George Haller and Guocheng Yuan. Lagrangian coherent structures and mixing in two-dimensional turbulence. Physica D: Nonlinear Phenomena, 147(3):352–370, 2000.

George Haller. Lagrangian coherent structures from approximate velocity data. Physics of Fluids, 14(6):1851–1861, 2002.

Shawn C Shadden, Francois Lekien, and Jerrold E Marsden. Definition and properties of lagrangian coherent structures from finite-time lyapunov exponents in two-dimensional aperiodic flows. Physica D: Nonlinear Phenomena, 212(3):271–304, 2005.

Doug Lipinski and Kamran Mohseni. A ridge tracking algorithm and error estimate for efficient computation of Lagrangian coherent structures. Chaos: An Interdisciplinary Journal of Nonlinear Science, 20(1):017504, 2010. doi: http://dx.doi.org/10.1063/1.3270049.

Helga S Huntley, BL Lipphardt, Gregg Jacobs, and AD Kirwan. Clusters, deformation, and dilation: Diagnostics for material accumulation regions. Journal of Geophysical Research: Oceans, 120(10):6622–6636, 2015.

Sanjeeva Balasuriya. Dynamical systems techniques for enhancing microfluidic mixing. Journal of Micromechanics and Microengineering, 25(9):094005, 2015.

Guo-Sheng He, Chong Pan, Li-Hao Feng, Qi Gao, and Jin-Jun Wang. Evolution of lagrangian coherent structures in a cylinder-wake disturbed flat plate boundary layer. Journal of Fluid Mechanics, 792:274–306, 2016.

George Haller. A variational theory of hyperbolic lagrangian coherent structures. Physica D: Nonlinear Phenomena, 240(7):574–598, 2011.

Greg A. Voth, G. Haller, and J. P. Gollub. Experimental measurements of stretching fields in fluid mixing. Phys. Rev. Lett., 88:254501, Jun 2002.

Manikandan Mathur, George Haller, Thomas Peacock, Jori E. Ruppert-Felsot, and Harry L. Swinney. Uncovering the lagrangian skeleton of turbulence. Physical Review Letters, 98(14):144502, 2007.

Shawn C Shadden, John O Dabiri, and Jerrold E Marsden. Lagrangian analysis of fluid transport in empirical vortex ring flows. Physics of Fluids (1994-present), 18(4):047105, 2006.

Melissa A Green, Clarence W Rowley, and George Haller. Detection of lagrangian coherent structures in three-dimensional turbulence. Journal of Fluid Mechanics, 572: 111–120, 2007.

Jifeng Peng and John O Dabiri. The 'upstream wake' of swimming and flying animals and its correlation with propulsive efficiency. Journal of Experimental Biology, 211 (16):2669–2677, 2008.

Doug Lipinski, Blake Cardwell, and Kamran Mohseni. A lagrangian analysis of a two-dimensional airfoil with vortex shedding. Journal of Physics A: Mathematical and Theoretical, 41(34):344011, 2008.

Blake M Cardwell and Kamran Mohseni. Vortex shedding over a two-dimensional airfoil: Where the particles come from. AIAA journal, 46(3):545–547, 2008.

Doug Lipinski and Kamran Mohseni. Flow structures and fluid transport for the hydromedusae sarsia tubulosa and aequorea victoria. Journal of Experimental Biology, 212(15):2436–2447, 2009.

Megan M Wilson, Jifeng Peng, John O Dabiri, and Jeff D Eldredge. Lagrangian coherent structures in low reynolds number swimming. Journal of Physics: Condensed Matter, 21(20):204105, 2009.

Steven L Brunton and Clarence W Rowley. Modeling the unsteady aerodynamic forces on small-scale wings. AIAA Paper, 1127(2009):1–14, 2009b.

Melissa A Green, Clarence W Rowley, and Alexander J Smits. Using hyperbolic lagrangian coherent structures to investigate vortices in bioinspired fluid flows. Chaos: An Interdisciplinary Journal of Nonlinear Science, 20(1):017510, 2010.

Clara O'Farrell and John O Dabiri. Pinch-off of non-axisymmetric vortex rings. Journal of Fluid Mechanics, 740:61–96, 2014.

Mohammad Farazmand and George Haller. Computing lagrangian coherent structures from their variational theory. Chaos: An Interdisciplinary Journal of Nonlinear Science, 22(1):013128, 2012a.

George Haller and Francisco J Beron-Vera. Coherent lagrangian vortices: The black holes of turbulence. Journal of Fluid Mechanics, 731:R4, 2013.

G Haller and Francisco J Beron-Vera. Addendum to 'coherent lagrangian vortices: the black holes of turbulence'. Journal of Fluid Mechanics, 755:R3, 2014.

Mohammad Farazmand and George Haller. Erratum and addendum to 'a variational theory of hyperbolic lagrangian coherent structures' [physica d 240 (2011) 574–598]. Physica D: Nonlinear Phenomena, 241(4):439–441, 2012b.

Mohammad Farazmand and George Haller. Attracting and repelling lagrangian coherent structures from a single computation. Chaos: An Interdisciplinary Journal of Nonlinear Science, 23(2):023101, 2013.

Mohammad Farazmand, Daniel Blazevski, and George Haller. Shearless transport barriers in unsteady two-dimensional flows and maps. Physica D: Nonlinear Phenomena, 278:44–57, 2014.

George Haller and Francisco J Beron-Vera. Geodesic theory of transport barriers in two-dimensional flows. Physica D: Nonlinear Phenomena, 241(20):1680–1702, 2012.

Francisco J Beron-Vera, Yan Wang, María J Olascoaga, Gustavo J Goni, and George Haller. Objective detection of oceanic eddies and the agulhas leakage. Journal of Physical Oceanography, 43(7):1426–1438, 2013.

Mohammad Farazmand and George Haller. Polar rotation angle identifies elliptic islands in unsteady dynamical systems. Physica D: Nonlinear Phenomena, 315:1–12, 2016.

George Haller, Alireza Hadjighasem, Mohammad Farazmand, and Florian Huhn. Defining coherent vortices objectively from the vorticity. Journal of Fluid Mechanics, 795: 136–173, 2016.

Clifford Truesdell and Walter Noll. The non-linear field theories of mechanics. In The non-linear field theories of mechanics, pages 1–579. Springer, 2004.

Binson Joseph and Bernard Legras. Relation between kinematic boundaries, stirring, and barriers for the antarctic polar vortex. Journal of the Atmospheric Sciences, 59 (7):1198–1212, 2002.

Francesco d'Ovidio, Vicente Fernández, Emilio Hernández-García, and Cristóbal López. Mixing structures in the mediterranean sea from finite-size lyapunov exponents. Geophysical Research Letters, 31(17), 2004.

Joao H Bettencourt, Cristóbal López, and Emilio Hernández-García. Characterization of coherent structures in three-dimensional turbulent flows using the finite-size lyapunov exponent. Journal of Physics A: Mathematical and Theoretical, 46(25):254022, 2013.

Gary Froyland and Kathrin Padberg. Almost-invariant sets and invariant manifoldsâĂŤconnecting probabilistic and geometric descriptions of coherent structures in flows. Physica D: Nonlinear Phenomena, 238(16):1507–1523, 2009.

Michael Dellnitz and Oliver Junge. for dynamical systems. Handbook of dynamical systems, 2:221, 2002.

Gary Froyland, Simon Lloyd, and Naratip Santitissadeekorn. Coherent sets for nonautonomous dynamical systems. Physica D: Nonlinear Phenomena, 239(16):1527–1541, 2010.

Michael R Allshouse and Jean-Luc Thiffeault. Detecting coherent structures using braids. Physica D: Nonlinear Phenomena, 241(2):95–105, 2012.

Marko Budišić and Jean-Luc Thiffeault. Finite-time braiding exponents. Chaos: An Interdisciplinary Journal of Nonlinear Science, 25(8):087407, 2015.

Marko Budišić and Igor Mezić. Geometry of the ergodic quotient reveals coherent structures in flows. Physica D: Nonlinear Phenomena, 241(15):1255–1269, 2012.

Gary Froyland and Kathrin Padberg-Gehle. Finite-time entropy: A probabilistic approach for measuring nonlinear stretching. Physica D: Nonlinear Phenomena, 241(19): 1612–1628, 2012.

Igor Mezić. Analysis of fluid flows via spectral properties of the koopman operator. Annual Review of Fluid Mechanics, 45:357–378, 2013.

Tian Ma and Erik M Bollt. Differential geometry perspective of shape coherence and curvature evolution by finite-time nonhyperbolic splitting. SIAM Journal on Applied Dynamical Systems, 13(3):1106–1136, 2014.

Gary Froyland and Kathrin Padberg-Gehle. A rough-and-ready cluster-based approach for extracting finite-time coherent sets from sparse and incomplete trajectory data. Chaos: An Interdisciplinary Journal of Nonlinear Science, 25(8):087406, 2015.

Igor Mezić, S Loire, Vladimir A Fonoberov, and P Hogan. A new mixing diagnostic and gulf oil spill movement. Science, 330(6003):486–489, 2010.

Raphael Fuchs, Ronald Peikert, Filip Sadlo, Bilal Alsallakh, and Eduard Gröller. Delocalized unsteady vortex region detectors. In VMV, volume 8, pages 81–90, 2008.

Kuangyu Shi, Holger Theisel, Helwig Hauser, Tino Weinkauf, Kresimir Matkovic, Hans-Christian Hege, and Hans-Peter Seidel. Path line attributes-an information visualization approach to analyzing the dynamic behavior of 3d time-dependent flow fields. Topology-Based Methods in Visualization II, pages 75–88, 2009.

Tino Weinkauf and Holger Theisel. Streak lines as tangent curves of a derived vector field. IEEE Transactions on Visualization and Computer Graphics, 16(6):1225–1234, 2010.

Alexander Wiebel, Raymond Chan, Christina Wolf, Andrea Robitzki, Angela Stevens, and Gerik Scheuermann. Topological flow structures in a mathematical model for rotation-mediated cell aggregation. Topological Methods in Data Analysis and Visualization. Springer, pages 193–204, 2011.

Ana M Mancho, Stephen Wiggins, Jezabel Curbelo, and Carolina Mendoza. Lagrangian descriptors: A method for revealing phase space structures of general time dependent dynamical systems. Communications in Nonlinear Science and Numerical Simulation, 18(12):3530–3557, 2013.

Ming Jiang, Raghu Machiraju, and David Thompson. Detection and visualization of. The Visualization Handbook, 295, 2005.

Alireza Hadjighasem, Mohammad Farazmand, Daniel Blazevski, Gary Froyland, and George Haller. A critical comparison of lagrangian methods for coherent structure detection. Chaos: An Interdisciplinary Journal of Nonlinear Science, 27(5):053104, 2017.

Christoph Garth, Florian Gerhardt, Xavier Tricoche, and Hagen Hans. Efficient computation and visualization of coherent structures in fluid flow applications. IEEE Transactions on Visualization and Computer Graphics, 13(6):1464–1471, 2007.

K Onu, Florian Huhn, and George Haller. Lcs tool: A computational platform for lagrangian coherent structures. Journal of Computational Science, 7:26–36, 2015.

Yuan Lu and Gong Xin Shen. Three-dimensional flow structures and evolution of the leading-edge vortices on a flapping wing. Journal of Experimental Biology, 211(8): 1221–1230, 2008.

Matthew P. Rockwood. Lagrangian visualization and real-Time identification of the vortex shedding time in the wake of a circular cylinder. PhD thesis, Syracuse University, 2017.

Karim Shariff, Anthony Leonard, and Joel H Ferziger. Dynamics of a class of vortex rings. Technical report, NASA Document, 1989.

V Rom-Kedar, A Leonard, and S Wiggins. An analytical study of transport, mixing and chaos in an unsteady vortical flow. Journal of Fluid Mechanics, 214:347–394, 1990.

John Guckenheimer and Philip J Holmes. Nonlinear oscillations, dynamical systems, and bifurcations of vector fields, volume 42. Springer Science & Business Media, 2013.

Ali B. Olcay, Tait S. Pottebaum, and Paul S. Krueger. Sensitivity of Lagrangian coherent structure identification to flow field resolution and random errors. Chaos: An Interdisciplinary Journal of Nonlinear Science, 20(1):017506, 2010. doi: 10.1063/1.3276062.

Matthew P Rockwood, Kunihiko Taira, and Melissa A Green. Detecting vortex formation and shedding in cylinder wakes using lagrangian coherent structures. AIAA Journal, 2016.

María J Olascoaga and George Haller. Forecasting sudden changes in environmental pollution patterns. Proceedings of the National Academy of Sciences, 109(13):4738–4743, 2012.

Philippe Miron and Jérôme Vétel. Towards the detection of moving separation in unsteady flows. Journal of Fluid Mechanics, 779:819–841, 2015.

Sanjeeva Balasuriya. Explicit invariant manifolds and specialised trajectories in a class of unsteady flows. Physics of Fluids, 24(12):127101, 2012.

Sanjeeva Balasuriya and Kathrin Padberg-Gehle. Accurate control of hyperbolic trajectories in any dimension. Physical Review E, 90(3):032903, 2014.

Sanjeeva Balasuriya, Rahul Kalampattel, and Nicholas T Ouellette. Hyperbolic neighbourhoods as organizers of finite-time exponential stretching. Journal of Fluid Mechanics, 807:509–545, 2016.

Yangzi Huang and Melissa A. Green. Detection and tracking of vortex phenomena using Lagrangian coherent structures. Experiments in Fluids, 56(7):1–12, July 2015. ISSN 0723-4864, 1432-1114. doi: 10.1007/s00348-015-2001-z.

G Haller and R Iacono. Stretching, alignment, and shear in slowly varying velocity fields. Physical Review E, 68(5):056304, 2003.

George Haller. Exact theory of unsteady separation for two-dimensional flows. Journal of Fluid Mechanics, 512:257–311, 2004.

Francois Lekien and George Haller. Unsteady flow separation on slip boundaries. Physics of fluids, 20(9):097101, 2008.

Philippe Miron, Jérôme Vétel, and André Garon. On the flow separation in the wake of a fixed and a rotating cylinder. Chaos: An Interdisciplinary Journal of Nonlinear Science, 25(8):087402, 2015.

Sanjeeva Balasuriya. A tangential displacement theory for locating perturbed saddles and their manifolds. SIAM Journal on Applied Dynamical Systems, 10(3):1100–1126, 2011.

George Haller, Alireza Hadjighasem, Mohammad Farazmand, and Florian Huhn. Defining coherent vortices objectively from the vorticity. arXiv preprint arXiv:1506.04061, 2015.

George Haller. Dynamic rotation and stretch tensors from a dynamic polar decomposition. Journal of the Mechanics and Physics of Solids, 86:70–93, 2016.

Kamran Mohseni, Hongyu Ran, and Tim Colonius. Numerical experiments on vortex ring formation. Journal of Fluid Mechanics, 430:267–282, 2001.

Norbert Didden. On the formation of vortex rings: rolling-up and production of circulation. Zeitschrift für Angewandte Mathematik und Physik (ZAMP), 30(1):101–116, 1979.

Paul S Krueger, John O Dabiri, and Morteza Gharib. The formation number of vortex rings formed in uniform background co-flow. Journal of Fluid Mechanics, 556:147–166, 2006.

Pooria Sattari, David E Rival, Robert J Martinuzzi, and Cameron Tropea. Growth and separation of a start-up vortex from a two-dimensional shear layer. Physics of Fluids, 24(10):107102, 2012.

David E Rival, Jochen Kriegseis, Pascal Schaub, Alexander Widmann, and Cameron Tropea. Characteristic length scales for vortex detachment on plunging profiles with varying leading-edge geometry. Experiments in fluids, 55(1):1–8, 2014.

Filip Sadlo and Ronald Peikert. Visualizing lagrangian coherent structures and comparison to vector field topology. Topology-Based Methods in Visualization II, pages 15–29, 2009.

David Rival, Roland Manejev, and Cam Tropea. Measurement of parallel blade–vortex interaction at low reynolds numbers. Experiments in Fluids, 49(1):89–99, 2010.

Eric Gutierrez, Daniel B Quinn, Diana D Chin, and David Lentink. Lift calculations based on accepted wake models for animal flight are inconsistent and sensitive to vortex dynamics. Bioinspiration & biomimetics, 12(1):016004, 2016.

J Panda and Khairul BMQ Zaman. Experimental investigation of the flow field of an oscillating airfoil and estimation of lift from wake surveys. Journal of Fluid Mechanics, 265:65–95, 1994.

John N. Fernando and David E. Rival. On vortex evolution in the wake of axisymmetric and non-axisymmetric low-aspect-ratio accelerating plates. Physics of Fluids (1994-present), 28(1):017102, 2016. ISSN 1070-6631, 1089-7666. doi: 10.1063/1.4938744.

Colin Hartloper, Matthias Kinzel, and David E Rival. On the competition between leading-edge and tip-vortex growth for a pitching plate. Experiments in fluids, 54(1):1447, 2013.

Manuel V Jain, Jaime G Wong, and David E Rival. Investigation of vortex development on accelerating spanwise-flexible wings. Journal of Fluids and Structures, 54:466–478, 2015.

Rajeev Kumar, Justin T King, and Melissa A Green. Momentum distribution in the wake of a trapezoidal pitching panel. Marine Technology Society Journal, 50(5):9–23, 2016.

John Kim, Parviz Moin, and Robert Moser. Turbulence statistics in fully developed channel flow at low Reynolds number. J. Fluid Mech., 177:133–166, 1987.

James HJ Buchholz and Alexander J Smits. On the evolution of the wake structure produced by a low-aspect-ratio pitching panel. Journal of fluid mechanics, 546:433–443, 2006.

James HJ Buchholz and Alexander J Smits. The wake structure and thrust performance of a rigid low-aspect-ratio pitching panel. Journal of fluid mechanics, 603:331–365, 2008.

Melissa A Green and Alexander J Smits. Effects of three-dimensionality on thrust production by a pitching panel. Journal of fluid mechanics, 615:211–220, 2008.

Jie Zhang, Nan-Sheng Liu, and Xi-Yun Lu. Locomotion of a passively flapping flat plate. Journal of Fluid Mechanics, 659:43–68, 2010.

R Wille. Karman vortex streets. Advances in Applied Mechanics, 6:273–287, 1960.

Stephen K Robinson. Coherent motions in the turbulent boundary layer. Annual Review of Fluid Mechanics, 23(1):601–639, 1991.

Kyle D Squires and John K Eaton. Lagrangian and eulerian statistics obtained from direct numerical simulations of homogeneous turbulence. Physics of Fluids A: Fluid Dynamics, 3(1):130–143, 1991.

Robert H Kraichnan. Lagrangian-history closure approximation for turbulence. The Physics of Fluids, 8(4):575–598, 1965.

Theodore Theodorsen. The structure of turbulence. University of Maryland, The Institute for Fluid Dynamics and Applied Mathematics, 1954.

YG Guezennec. Stochastic estimation of coherent structures in turbulent boundary layers. Physics of Fluids A: Fluid Dynamics (1989-1993), 1(6):1054–1060, 1989.

Ronald J. Adrian. Hairpin vortex organization in wall turbulencea). Physics of Fluids (1994-present), 19(4):041301, 2007. ISSN 1070-6631, 1089-7666. doi: 10.1063/1.2717527.

Garry L Brown and Andrew SW Thomas. Large structure in a turbulent boundary layer. The Physics of fluids, 20(10):S243–S252, 1977.

RJ Adrian, CD Meinhart, and CD Tomkins. Vortex organization in the outer region of the turbulent boundary layer. Journal of Fluid Mechanics, 422:1–54, 2000.

Bharathram Ganapathisubramani, Ellen K Longmire, and Ivan Marusic. Characteristics of vortex packets in turbulent boundary layers. Journal of Fluid Mechanics, 478:35–46, 2003.

Christopher D Tomkins and Ronald J Adrian. Spanwise structure and scale growth in turbulent boundary layers. Journal of Fluid Mechanics, 490:37–74, 2003.

N Hutchins, WT Hambleton, and Ivan Marusic. Inclined cross-stream stereo particle image velocimetry measurements in turbulent boundary layers. Journal of Fluid Mechanics, 541:21–54, 2005.

Alexander J Smits, Beverley J McKeon, and Ivan Marusic. High–reynolds number wall turbulence. Annual Review of Fluid Mechanics, 43:353–375, 2011.

KC Kim and RJ Adrian. Very large-scale motion in the outer layer. Physics of Fluids, 11(2):417–422, 1999.

CD Tomkins and RJ Adrian. Energetic spanwise modes in the logarithmic layer of a turbulent boundary layer. Journal of Fluid Mechanics, 545:141–162, 2005.

M Guala, SE Hommema, and RJ Adrian. Large-scale and very-large-scale motions in turbulent pipe flow. Journal of Fluid Mechanics, 554:521–542, 2006.

BJ Balakumar and RJ Adrian. Large-and very-large-scale motions in channel and boundary-layer flows. Philosophical Transactions of the Royal Society of London A: Mathematical, Physical and Engineering Sciences, 365(1852):665–681, 2007.

JP Monty, JA Stewart, RC Williams, and MS Chong. Large-scale features in turbulent pipe and channel flows. Journal of Fluid Mechanics, 589:147–156, 2007.

Henry P Bakewell Jr and John L Lumley. Viscous sublayer and adjacent wall region in turbulent pipe flow. Physics of Fluids (1958-1988), 10(9):1880–1889, 1967.

MR Head and P Bandyopadhyay. New aspects of turbulent boundary-layer structure. Journal of Fluid Mechanics, 107:297–338, 1981.

AE Perry and MS Chong. On the mechanism of wall turbulence. Journal of Fluid Mechanics, 119:173–217, 1982.

AE Perry, S Henbest, and MS Chong. A theoretical and experimental study of wall turbulence. Journal of Fluid Mechanics, 165:163–199, 1986.

Xiaohua Wu and Parviz Moin. Direct numerical simulation of turbulence in a nominally zero-pressure-gradient flat-plate boundary layer. Journal of Fluid Mechanics, 630:5–41, 2009.

C. Rt Smith, J. D. A. Walker, A. H. Haidari, and U. Sobrun. On the dynamics of near-wall turbulence. Philosophical Transactions of the Royal Society of London A: Mathematical, Physical and Engineering Sciences, 336(1641):131–175, 1991.

Y Jodai and GE Elsinga. Experimental observation of hairpin auto-generation events in a turbulent boundary layer. Journal of Fluid Mechanics, 795:611–633, 2016.

Yangzi Huang

www.linkedin.com/in/yangzi-huang yhuang44@syr.edu
300 Ashland Pl. Brooklyn, NY 11217 585-754-1090

EDUCATION

SYRACUSE UNIVERSITY, Syracuse, NY

PhD Candidate in Mechanical and Aerospace Engineering Aug. 2013 – Dec. 2017
STEM certified program, providing 3 years work authorization
Advisor: Dr. Melissa A. Green; **Thesis:** "Vortex shedding study in massively separated flow"
Journal publication: Huang, Y. and Green, M.A. Detection and tracking of vortex phenomena using Lagrangian coherent structures. Experiments in Fluids. 56, 7, 1-12, 2015.
Teaching Assistant – Methods of Analysis in Mechanical Engineering

XI'AN JIAO TONG UNIVERSITY, Xi'an, Shaanxi, China

Master of Science in Power Machinery Engineering Sept. 2008 – June 2011
Awards: Innovation Scholarship Recipient; Outstanding Graduates of Xi'an Jiao Tong University (Top 2%)
Bachelor of Thermal Energy and Power Engineering Sept. 2004 – June 2008
Awards and Engagements: Siyuan Scholarship (Top 5%); Minister, Arts Department of Student Union and Chairman of University Cycling Club.
Graduate Student Mentor – Assisted graduate students with thesis writing.

EXPERIENCE

SYRACUSE UNIVERSITY, Syracuse, NY

Research Assistant, Mechanical & Aerospace Engineering Dept. Aug. 2013 – Dec. 2017
- Conducted analytical research with Matlab and Fortran on flow patterns and shedding mechanisms of Micro Aerial Vehicles.
- Builded data visualization and identification methodologies with Matlab and Python in hairpin-shape flow patterns evolution.
- Performed statistical analysis with Matlab, Python and Pearl on three-dimensional flow data sets in complex turbulent flow.

SHANGHAI ELECTRIC - POWER GENERATION GROUP, Shanghai, China

Multinational power generation and electrical equipment manufacturing company – the world's largest manufacturer of steam turbines
Fluid Mechanics Lead Engineer, Gas Turbine Research Institute Aug. 2011 – June 2013
- Led a team of two to support and monitor several prototype product research projects through all stages: initiation, execution, documentation and reporting.
- Developed new management system and internal processes for research projects, budgets and database using MS Visio by leveraging firm best practices.
- Identify Key Performance Indicators (KPI) for measuring the researcher performances.
- Facilitated communication between institute and internal departments including technology, manufacturing and finance.
- Designed programming modules contributing to power plant performance estimation utilizing GateCycle and IPSEpro.
- Improved performance of prototype turbine seal using ANSYS CFX with optimized parameters by 3% leakage decreasing.
- Updated empirical equation for seal product design with Matlab, and successfully achieved a 5% calculation error reduction.

XI'AN JIAO TONG UNIVERSITY, Xi'an, Shaanxi, China

Research Assistant, Mechanical & Aerospace Engineering Dept. Sept. 2008 – June 2011
- Builded a mode of the brush seal with ANSYS Fluent to enable numerical performance analysis for industrial seal design.
- Constructed optimal structure parameters for reliable and practical brush seal with ANSYS Fluent and Matlab

COMPETENCIES

- **Software:** Matlab, Fieldview, LaTex, Visio, Access, Maple, ANSYS (CFD), AutoCAD, Solidworks, GateCycle, IPSEpro.
- **Programming Languages:** Fortran, Python, SQL, R, Pearl, C++.

SKILLS & INTERESTS

Language skills: Fluent English, native Mandarin Chinese, and beginner level Swedish
Other: Presented research findings at numerous conferences, including American Institute of Aeronautics and Astronautics.